Dispersion Properties of Photonic Crystals and Silicon Nanostructures Investigated by Fourier-Space Imaging

PAR

Jana JÁGERSKÁ

ÉCOLE POLYTECHNIQUE
FÉDÉRALE DE LAUSANNE

Suisse
2011

Contents

Abstract

State-of-the-art nanophotonic devices based on semiconductor technology use total internal reflection or the photonic bandgap effect to reduce the waveguide core dimensions down to hundreds of nanometers, ensuring strong optical confinement within the scale of the wavelength. Within the framework of this thesis, we investigate the light propagation in such devices by direct experimental reconstruction of their dispersion relation $\omega(k)$, where ω is the optical frequency and k the wave vector of the supported modes. Knowledge of the dispersion relation provides us with comprehensive information about the guided field, including the number of supported modes, their phase and group velocity as well as the higher order dispersion.

As a principal characterization tool, an original experimental technique referred as Fourier-space imaging is used. It is based on far-field analysis of optical signal radiated out of the plane of the structure, which makes it possible to retrieve accurately, non-invasively and in one step the complex dispersion of both the leaky and the truly guided optical modes. The latter is feasible provided that the device is equipped with vanishingly weak grating probes that scatter a small part of the guided light into the light cone.

The Fourier-space imaging technique was applied to study the optical properties of a large number of nanophotonic devices, ranging from simple nanowire waveguides to complex photonic crystal structures. In the first part of the work, silicon-on-insulator slot waveguides, coupled ridge waveguides and nanowire waveguide arrays are addressed. Besides the phase and group index dispersion, we investigate the phenomenon of mode splitting in coupled systems, being able to probe the coupling lengths with an accuracy of ± 50 nm. In the case of waveguide arrays, beam steering using both thermo-optic effect and wavelength tuning was demonstrated.

Concerning the photonic crystal devices, we primarily focus on the phenomenon of slow light propagation in line-defect and coupled-cavity photonic crystal waveguides. The latter represent a special type of a waveguide, which allows for substantial optical signal retardation by evanescent coupling along a chain of photonic crystal cavities. The main motivation was to accurately measure the group index of the slow light modes and recognize the main factors limiting its maximum achievable value. Among others, experimental observation of dispersion curve renormalization, enhanced out-of-plane and back-scattering as well as light localization due to residual disorder were reported.

Finally, a detailed experimental study of hollow-core photonic crystal structures intended for optical sensing applications is presented.

Keywords:
Nanophotonics, Photonic crystals, Dispersion, Slow light, Fourier-space imaging

Résumé

L'état de l'art des dispositifs nanophotoniques basé sur la technologie semiconduteur se base sur la reflection totale interne ou l'effet de bande interdite photonique pour réduire les dimensions de coeur des guides d'onde à quelques centaines de nanomètres. Dans le cadre de cette thèse, nous étudions la propagation de la lumière dans de telles structures grâce à la reconstruction expérimentale de leur relation de dispersion $\omega(k)$, où ω correspond à la fréquence optique et k au vecteur d'onde des modes supportés. La connaissance de la relation de dispersion nous donne accès à une grande quantité d'informations concernant le champ guidé, dont le nombre de modes supportés, leur phase, leur vitesse de groupe ainsi que la dispersion d'ordre supérieur.

Pour caractériser cette relation, une méthode originale d'imagerie de Fourier a été utilisée. Elle est basée sur l'analyse du champ lointain du signal optique diffusé hors du plan de la structure. Elle permet de retrouver de manière directe, précise, et non-invasive la dispersion complexe des modes radiatifs comme des modes optiques guidés. Ce dernier aspect est rendu possible par l'ajout d'un réseau de sondes faible à la structure étudiée, et dont la fonction est de diffuser une infime partie de la lumière guidée dans le cône de lumière.

La technique d'imagerie de Fourier a été appliquée à l'étude des propriétés optiques d'un grand nombre de dispositifs nanophotoniques, allant de simple guides "nanofils" à des structures à cristaux photoniques complexes. La première partie de ce travail est consacrée aux guides d'ondes tranchés, aux guides en arêtes couplés et aux réseaux de nanofils. En plus des dispersions de phase et de groupe, nous étudions le phénomène de séparation de modes dans les systèmes couplés et la détermination de la longueur de couplage avec une précision de ± 50 nm. Dans le cas des réseaux de guides d'onde, la déflection de faisceau par effet thermo-optique et par accord de longueur d'onde a été démontrée.

Pour les dispositifs à cristaux photoniques, nous nous consacrons principalement à l'étude du phénomène de lumière lente dans les guides à défaut de ligne et les guides à cavités couplées. Ces derniers forment une famille de guides d'onde toute particulière qui permet d'induire un retard substantiel du signal optique par le couplage évanescent le long d'une chaine. Le but principal est la mesure précise de l'indice de groupe des modes lents et l'identification des facteurs qui en limitent le maximum. Les observations expérimentales de renormalisation de la courbe de dispersion, de renforcement de la diffusion hors-plan et de la rétrodiffusion ainsi que de localisation induite par le désordre sont reportées.

Pour finir, une étude expérimentale détaillée de structures à cristaux photoniques creuses imaginées pour des applications de détection optique est présentée.

Mots-clés:
Nanophotonique, Cristaux photoniques, Dispersion, Lumière lente, Imagerie de Fourier

Introduction

Photonics as a new research field was founded in the late 1960s, with the purpose of using light to perform functions that traditionally fall into the domain of electronics. The first successful inventions of photonics such as laser diode and optical fibers for long-haul data transmission gave rise to the telecommunication revolution in the end of the 20th century, which, in return, became a strong driving force for further photonic research.

With the exception of the past decade, photonics focused mainly at telecom applications. Combining or replacing the electronic circuits by integrated nanophotonic devices should lead to a dramatic increase in the capacity of transmitted data (ultra-high bandwidth with Wavelength Division Multiplexing) and considerable reduction of the power consumption (*e.g.* power dissipated in metallic interconnects due to their nonzero resistance). Since the past 25-30 years, there has been a lot of effort invested into the development of photonic devices that can not only transmit, but also control, route and process optical signal in a way similar to electronic circuits. Examples of such devices include interconnecting waveguides with sharp bends, filters, couplers and splitters, multiplexers, optical delay lines, optical memories and logical gates. The challenge is not only to implement all these functions with optics, but also to scale them down in order to achieve a similar integration density as that of the modern electronics (see Fig. 1).

The state-of-the-art photonics covers much broader area of applications than the telecommunication industry. The ability to control the light, its generation, propagation, and specific interaction with matter proved to be highly appealing for biological and chemical sensing applications, medical diagnostics, therapy, and optical imaging. Recently, considerable attention has been given to quantum photonics and its new, related domains such as quantum computing and quantum cryptography.

Today's commercial photonic components based on lithium niobate or glass integrated

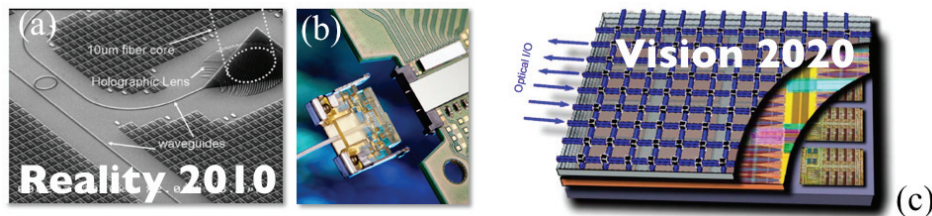**Figure 1:** Integrated photonic circuits available with the state-of-the-art technology and the vision for the future: (a) 10 Gb/s per channel single-chip optoelectronic transceiver based on SOI [1], (b) Intel's End-to-End Silicon Photonics Connection with Integrated Lasers [2], (c) IBM's 2020 vision for 22 nm CMOS on-chip optical interconnects that both connect electronic chips and route the data trafic [3].

optics are, however, too large to allow for much integration. Low index contrast between the core and the cladding regions results in low propagation loss (below 0.1 dB/cm), but also in a typical scale of several millimeters to centimeters. On the integrated level, they cannot be used to implement more complicated functions than simple on-board (chip to chip) interconnects. Increasing the refractive index contrast between the core and the cladding material makes it possible to better confine light, and hence, to significantly reduce the size of the optical components. The reduction in size is scaled with the refractive index contrast: the higher the contrast, the smaller the size in order to maintain single-mode operation. Typical dimensions of high index contrast structures reduce to hundreds of nanometers with the smallest features scaled down to several tens of nanometers. Therefore, they are often related as *nanophotonic* structures.

High index contrast devices are mostly based on semiconductor or semiconductor oxide material systems, the most common are: silicon oxide, silicon nitride, silicon (Si), silicon-on-insulator (SOI), indium phosphide (InP) and gallium arsenide (GaAs). A great advantage of silicon is the compatibility with the Compound Metal Oxide Semiconductor (CMOS) technology that is currently used for mass production of electronic circuits, which results in a wide availability of high quality substrates and low price production, as well as in an easy integration with nanoelectronics. However, silicon as an indirect bandgap semiconductor is not readily suitable for production of light sources as laser or light-emitting diodes, and is typically used to realize purely passive components. If active components are desired, group III-V semiconductors (GaAs or InP) are of primary choice, either standalone or integrated with silicon as hybrid silicon lasers [4]. Nevertheless, one should mention that lasing in silicon is possible by making use of Raman scattering: silicon Raman lasers with decent threshold (20 mW), slope efficiency (28%) and output power (50 mW) have already been reported [5].

There are two principal mechanisms of light confinement in dielectric nanophotonic structures, *i.e.* the total internal reflection and the photonic bandgap effect. The total internal reflection (TIR), or refractive index guiding, relies on existence of high refractive index core surrounded by low index cladding; light coupled into the core is totally reflected at the core/cladding interface and remains confined within the core region [6]. A typical examples of TIR-based structures are nanophotonic waveguides with rectangular cross-section often related as photonic wires [7, 8]. Their cross-sectional dimensions are around 300×400 nm, allowing for realization of compact elements like sharp bends (radius lesser than 10 μm), ultra-short couplers [9–11] or ring resonator devices [12]. One special type of photonic wires are slot waveguides [13, 14], which consist of two parallel wires separated by approx. 100 nm. The optical field is mainly concentrated in the slit, which is advantageous if strong optical interaction with the surrounding low-index medium is desired (optical sensing, nonlinear experiments). Last but not least, subwavelength grating waveguides [15] represent a novel solution that allows to freely engineer the waveguide refractive index and, hence, the optical field confinement. The subwavelength grating waveguide is formed by a linear array of periodic rectangular segments with structural period of approx. 300 nm. The refractive index of the core can be tuned lithographically by changing the volume fractions of the Si-segments and the cladding material. Such structures can also realize virtually lossless crossings as well as optical fiber/nanowire tapers of excellent performance [16, 17].

The second physical mechanism of light confinement, the photonic bandgap effect occurs in photonic crystals, *i.e.*, materials with periodic modulation of the dielectric constant. Multiple scattering from the periodic index perturbation leads to creation of so-called pho-

tonic bandgap (PBG), a frequency interval, where no light propagation is allowed. For optical frequencies inside the bandgap, photonic crystals act as a perfect mirror and can confine and guide optical signal along regions where the strict periodicity is broken. Thus, introducing point or line defects in otherwise unperturbed photonic crystal lattice, one can form optical cavities with high quality factors and low mode volumes, or theoretically lossless optical waveguides. Generally, photonic crystals can realize smaller and more complex structures than nanophotonic wires, yet, at the expense of slightly higher propagation losses (record low loss values of 5 dB/cm in photonic crystal line-defect waveguides were achieved [18], compared to 2 dB/cm loss figure of standard SOI nanowires [8].)

Besides the PBG effect, light confinement in photonic crystals can be realized by self-collimation [19] or by the slow light effect at the photonic band edge. The latter phenomenon results from the fact that in the proximity of the photonic bandgap the group velocity of supported optical modes drops to zero. Slow light has recently intrigued many researchers as slow modes represent an optical feedback mechanism for lasers [20] as well as they can create large pulse delays if the propagation is limited to one dimension as in optical waveguides. It has been shown experimentally that group velocity reduction by a factor of 100 or more is possible in specially tailored photonic crystal waveguides [21], which suggests a large spectrum of applications such as optical buffers and delay lines. In addition, the slow light effect brings along an enhancement of light-matter interaction, which may lead to further down-scaling of size of optical devices, especially those that rely on nonlinear phenomena or optical phase shift (*e.g.* photonic crystal couplers [10], optical (bio)sensors [22]).

For completeness, it should be mentioned that light can be extremely well confined in plasmonic nanostructures [23] comprising a metal/dielectric interface. The practical applicability of these structures in integrated nanophotonics is mostly hindered by losses that arise from inherent absorption of light in metals. There are, however, two specialized areas where plasmonic devices proved their excellence: the field of biosensing and biomedical imaging.

The aim of the present work is to investigate both theoretically and experimentally the optical properties of advanced photonic nanostructures intended for high-density integration. Particular attention is paid to complex photonic crystal devices like specially tailored slow light photonic crystal waveguides or high-Q cavities, the underlying physics of which is not yet fully understood.

The manuscript is divided into 8 chapters. The first chapter has an introductory character and explains the most important theoretical concepts of light propagation in high-index contrast dielectric waveguides and photonic crystals. It focuses in more detail on 2D photonic crystals in dielectric slabs, which are compatible with the current CMOS fabrication technology. An overview of the most common photonic crystal structures is given together with a brief discussion of their basic properties and applications.

The small geometrical features of nanophotonic structures bring along strict requirements on fabrication tolerances, as they need to be processed with precision of one to ten nanometers to achieve well-defined optical properties and minimal residual scattering loss. The second chapter reviews the fabrication techniques capable of meeting such tolerances, with emphasis given on Si and SOI material technology.

The third chapter presents different experimental measurement techniques used for characterization of nanophotonic structures. A large section is dedicated to the description

of Fourier-space imaging method, a non-invasive characterization technique developed at EPFL and refined within the framework of this thesis. The Fourier-space imaging technique allows us to directly probe the dispersion relation of nanophotonic waveguides, and hence, to obtain the information about the phase and group velocity of supported modes and their higher order dispersion. Understanding and molding the dispersion is of particular interest in photonic crystals, which exhibit complex dispersion characteristics similar to the energy band diagrams of solid-state materials.

Experimentally measured dispersion of different nanostructures is presented and discussed in the remaining part of this thesis. The fourth chapter reports on dispersion properties of rectangular and slot nanophotonic waveguides, wire couplers and coupled waveguide arrays. The fifth and sixth chapter focuse on photonic crystal devices such as self-collimating bulk photonic crystals or line defect waveguides specially tailored for slow light applications. Among others, coupling into slow light modes and their sensitivity to residual disorder are discussed. A special type of slow light waveguide consisting of coupled optical resonators, the coupled cavity waveguide, is investigated in the seventh chapter. Formation of the coupled cavity mode and its intrinsic limitations due to radiation loss, finite size and disorder are addressed. Finally, the last chapter reports on the development of a refractive index sensor based on a photonic crystal cavity. Such a sensor with a sensing volume of only 40 aliters represents a possible solution for integrated (bio)sensors oriented towards parallel detection.

Chapter 1

Light confinement in dielectric nanostructures

1.1 Electromagnetic waves in homogeneous environment

In traditional optical instruments and systems, the light transmission between two locations is often realized in free space. The propagation of light in a homogeneous dielectric medium without any electric charges or currents is fully described by four Maxwell's equations:

$$\nabla \times \mathbf{E} + \frac{\partial \mathbf{B}}{\partial t} = 0 \quad \nabla \cdot \mathbf{D} = 0 \tag{1.1}$$

$$\nabla \times \mathbf{H} - \frac{\partial \mathbf{D}}{\partial t} = 0 \quad \nabla \cdot \mathbf{B} = 0 \tag{1.2}$$

and two constitutive relations:

$$\mathbf{D} = \varepsilon \varepsilon_0 \mathbf{E} \quad \mathbf{B} = \mu_0 \mathbf{H} \tag{1.3}$$

with $\mathbf{E}$ the electric field, $\mathbf{H}$ the magnetic field, $\mathbf{D}$ the electric displacement and $\mathbf{B}$ the magnetic induction. The fields and inductions depend on the time and position, while the electric permittivity ε is a constant. Assuming harmonic time dependence of the solution in the form $\mathbf{E}(\mathbf{r}, t) = \mathbf{E}(\mathbf{r})e^{-i\omega t}$, the Maxwell's equations can be simplified to the Helmholz's equation:

$$\nabla^2 \mathbf{E} = \varepsilon \left(\frac{\omega}{c} \right)^2 \mathbf{E} \tag{1.4}$$

The most simple solution of Maxwel's equations is a plane wave $\mathbf{E}(\mathbf{r}, t) = E_0 e^{i(kz - \omega t)}$. It propagates in one given direction z, and its wavefronts, *i.e.* surfaces of constant phase, are infinite planes of constant amplitude oriented perpendicular to the direction of propagation. In a very coarse approximation, such wave can describe the propagation of a coherent, collimated beam originating from an extremely large optical source (such as laser beams used in lunar ranging experiments [24]). Plane waves of different directions create an ortogonal basis, and any optical wave that solves Maxwell's equation can be represented as their linear superposition.

Propagation of a plane wave is fully described by two quantities: the optical frequency ω and the wave vector $\mathbf{k}$. The direction of $\mathbf{k}$ determines the direction of propagation of the
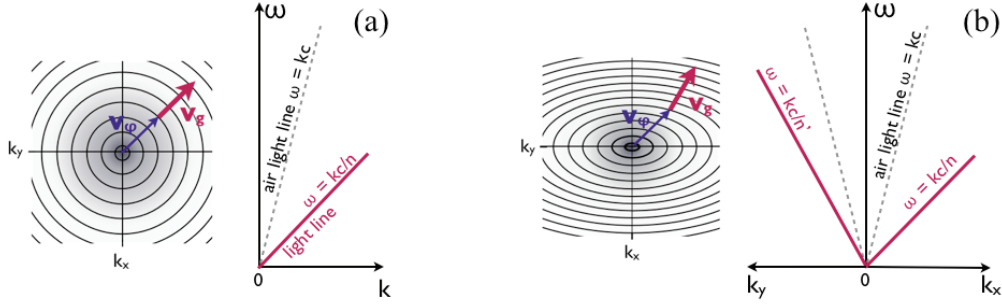
Figure 1.1: Two-dimensional dispersion map and projected dispersion diagram of (a) homogeneous isotropic and (b) anisotropic dielectric.

plane wave and the optical frequency divided by the norm of $\mathbf{k}$ defines its phase velocity:

$$\mathbf{v}_\varphi = \frac{\mathbf{k}}{k}\frac{\omega}{k} \tag{1.5}$$

The quantities k and ω are not independent, they are linked together by the *dispersion relation* standardly written in the form:

$$\omega = kv_\varphi = k\frac{c}{n} \tag{1.6}$$

where c the speed of light and $n = \sqrt{\varepsilon}$ the refractive index of the dielectric medium.

In an isotropic medium (*e.g.* in free space), the dispersion doesn't depend on the direction of propagation. Hence, the dispersion relation can be well represented by a one-dimensional plot $\omega = f(k)$ as is graphically illustrated in Fig. 1.1(a). For each frequency ω, there is just one k, and, hence, one phase velocity equal to $v_\varphi = c/n$. The corresponding linear dispersion relation $\omega = kc/n$ is often called the *light line*.

On the contrary, in an anisotropic medium the phase velocity depends on the propagation direction. The dispersion can be visuallized as a 2D dispersion map shown in Fig. 1.1(b), where the iso-frequency contours $\omega(\mathbf{k}) = const.$ form concentric ellipsoids. If projected into one-dimensional dispersion diagram $\omega = f(k)$, dispersion along all principal optical axes must be shown.

Besides the phase velocity, one defines the group velocity as a gradient of the optical frequency in respect to $\mathbf{k}$:

$$\mathbf{v}_g = \frac{\mathrm{d}\omega}{\mathrm{d}\mathbf{k}} = \nabla_k(\omega) \tag{1.7}$$

In a medium without losses, group velocity gives the direction and the velocity of the energy transport, or equally, the direction and velocity of propagation of optical information carried by a wave packet. Its value is given by the slope of the dispersion curve and its direction is always perpendicular to iso-frequency contours $\omega(\mathbf{k}) = const.$ as depicted in Fig. 1.1. In the vacuum or non-dispersiove homogeneous dielectric the group and phase velocity coincide. In a general dielectric, weak deviation from the strict dispersion relation is possible due to material dispersion $n = n(\omega)$ and the norm of the group velocity can become slightly larger or smaller than the v_φ. However, as long as the dielectric is isotropic, the directions of the two velocities are the same regardless of the material dispersion.

Anisotropy leads to distinction in the direction of v_g and v_φ as shown in Fig. 1.1(b).

1.1.1 Light confinement in a homogeneous medium

The plane waves $\mathbf{E}(\mathbf{r}, t) = E_0 \mathrm{e}^{i(kz - \omega t)}$ propagate in one unique direction, and, hence, they exhibit no angular spread. However, its energy is spatially delocalized over all of the space. On the contrary, a spherical wave $\mathbf{E}(\mathbf{r}, t) = \mathbf{E}(r, t)\mathrm{e}^{i(kr - \omega t)}$, which also solves the Maxwell's equations, is perfectly spatially confined at its origin (point source), but it diverges in all angular directions as it propagates. A compromise between spatially localized and nondiverging waves is the Gaussian beam. Unlike the plane wave, the latter has spatially localized envelope while keeping one principal direction of propagation. However, the envelope broadens and the peak intensity of the beam decreases as a function of the axial distance z, the beam diverges. The divergence angle is inversely proportional to the beam waist diameter: the more the beam is spatially localized at its waist, the more it diverges angularly.

Simultaneous spatial and angular confinement in a homogeneous medium are precluded by the wave nature of light. Such confinement can be, however, achieved when introducing one or more interfaces between homogeneous media that can reflect, refract or scatter light.

1.2 Total internal reflection in high index contrast dielectric waveguides

Light incident on an interface of two homogeneous dielectric media can be reflected or refracted; normally both phenomena occur simultaneously. The angular (Snell's law) and the amplitude (Fresnel's formulae) condition for the reflected and refracted wave can be derived from Maxwell's equations, more specifically from the interface condition of the electromagnetic field (with no charges and no currents):

$$\vec{n} \times (\mathbf{E}_2 - \mathbf{E}_1) = 0 \quad \vec{n} \cdot (\mathbf{D}_2 - \mathbf{D}_1) = 0 \tag{1.8}$$

$$\vec{n} \times (\mathbf{H}_2 - \mathbf{H}_1) = 0 \quad \vec{n} \cdot (\mathbf{B}_2 - \mathbf{B}_1) = 0 \tag{1.9}$$

where $\vec{n}$ is the unity vector perpendicular to the interface. It follows from 1.8 that the tangential components of fields $\mathbf{E}$, $\mathbf{H}$ and the normal components of inductions $\mathbf{D}$, $\mathbf{B}$ must be continuous at the interface; both their phases and amplitudes. The continuity of the fields implies that the tangential component of the k-vector must be also continuous at the interface, which can be graphically illustrated in Fig. (1.2) and mathematically by the following formulas for the reflected and refracted wave:

$$(\mathbf{k}_1 - \mathbf{k}_1') \times \vec{n} = 0 \qquad (\mathbf{k}_1 - \mathbf{k}_2) \times \vec{n} = 0 \tag{1.10}$$

The first equation yields the Snell-Descartes' law of reflection, the second of refraction:

$$\begin{array}{cc} \textbf{Reflection} & \textbf{Refraction} \\ \mathbf{k}_{1t} = \mathbf{k}_{1t}' & \mathbf{k}_{1t} = \mathbf{k}_{2t} \\ \theta_1 = \theta_1' & n_1 \sin(\theta_1) = n_2 \sin(\theta_2) \end{array} \tag{1.11}$$
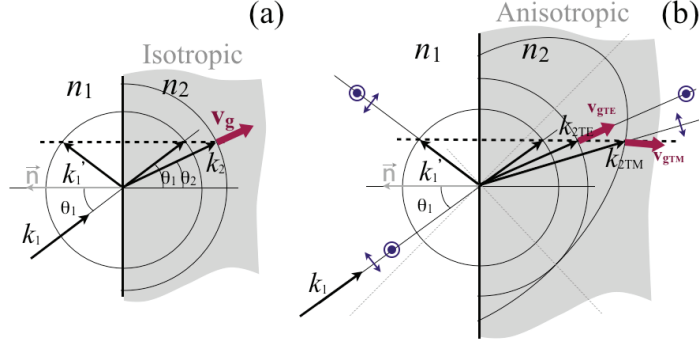
Figure 1.2: Graphical illustration of the continuity of tangential k-vector components at the interface of two homogeneous media. (a) Reflection and refraction from optically thinner to optically thicker isotropic media: figure shows the direction of the phase and group velocity of both the reflected and refracted beams. In isotropic medium, the group velocity equals to the phase velocity and its direction is independent of light polarization. (b) Reflection and refraction from isotropic to anisotropic medium. Direction of the refracted beams depends on the polarisation of the incident light. As the group velocity remains at each point perpendicular to the index ellipsoid, the phase and the group velocity are generally oriented in different directions.
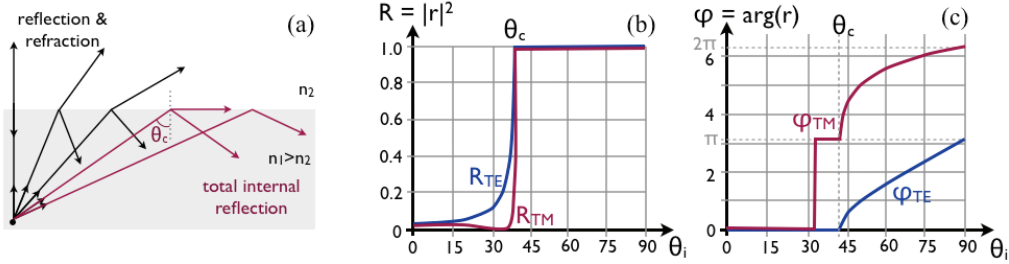
Figure 1.3: (a) Reflection and refraction from optically thicker to optically thiner medium. At incidence angles larger than the critical angle the total internal reflection occurs. (b) Reflectivity and phase of the reflected beam calculated from Fresnel Formulas.

Total internal reflection. Let's assume that the light is incident from a medium with higher refractive index $n_1 > n_2$. As the angle of incidence θ_1 increases, the angle of refraction θ_2 increases accordingly as shown in Fig. 1.3(a) until reaching value $\pi/2$, *i.e.* the refracted wave propagates strictly parallel to the interface. Corresponding angle of incidence is called the critical angle $\theta_{1c} = \arcsin(n_2/n_1)$. For angles larger than θ_{1c} all light is reflected back into the medium of incidence: we speak about the total internal reflection (TIR). The electromagnetic field that penetrates into the medium 2 decays evanescently and does not carry any energy in the direction away from the interface.

Although there is no change in amplitude of the reflected light for angles θ_1 larger than θ_c, the phase difference between between the incident and the reflected light increases as a function of θ_1. The exact amplitude and phase relations upon reflection can be derived from the conditions of electric and magnetic field continuity at the interface (Eq. (1.8,

1.9)), and are expressed by the Fresnel formulas [6, 25] :

$$r_{TE} = \frac{\mathrm{tg}(\theta_1 - \theta_2)}{\mathrm{tg}(\theta_1 + \theta_2)} = \mathrm{e}^{i\varphi_{TE}} \tag{1.12}$$

$$r_{TM} = -\frac{\sin(\theta_1 - \theta_2)}{\sin(\theta_1 + \theta_2)} = \mathrm{e}^{i\varphi_{TM}} \tag{1.13}$$

here r is the reflectivity coefficient and it depends on the polarization of the incident light. We distinguish two principal cases: the TE polarization where the electric field is polarized parallel to the interface, *i.e.* no electric field in the direction of propagation, and the TM polarization, where the magnetic field is parallel to the interface and has no component in the propagation direction. The angular dependence of the amplitude and phase of the reflectivity coefficients at the glass-air interface is graphically shown in Fig. 1.3(b).

1.2.1 Planar (slab) waveguides

Planar dielectric waveguide is a slab of a dielectric material (core) surrounded by media with lower refractive index (cladding). Light which propagates in the slab at angles larger than the critical angle undergoes multiple total internal reflections at the core/cladding interfaces and can be guided in the slab without any out-of-plane losses. This is the concept of so-called *index quiding.*

Nevertheless, light cannot be guided at an arbitrary angle $\theta > \theta_c$; it is necessary that after the two subsequent reflections the electromagnetic wave constructively interferes with the original wave like shown in Fig. 1.4(a). Otherwise, the optical intensity decays along the propagation direction as a result of destructive interference. This is known as *the self-consistency condition*, which determines the optical modes of the waveguide. For a simple step-index slab waveguide the self-consistency condition can be formulated in the following way:

$$\underbrace{\frac{2\pi}{\lambda_0} 2d \sin\theta_m^{\mathrm{TE/TM}}}_{\text{propagation}} - \underbrace{2\varphi^{\mathrm{TE/TM}}}_{\text{reflection}} = 2\pi m, \qquad m = 0, 1, 2...N \tag{1.14}$$

where d is the slab thickness and λ_0 the vacuum wavelength. The angles $\theta_m^{\mathrm{TE/TM}}$ define the wave vector components in the propagation direction, called the propagation constants $\beta_m^{\mathrm{TE/TM}} = n_1 k_0 \cos\theta_m^{\mathrm{TE/TM}}$. Note that the propagation constant differs for TE and TM modes due to the polarization dependence of the phase shift term φ.

The same solution $\beta_m^{\mathrm{TE/TM}}$ can be obtained from electromagnetic formulation of the problem. For the TE-polarized modes propagating along z, the only nonzero component of the electric field points in the y direction (the coordinate system is defined in Fig. 1.4(a)), and since the system is homogeneous in y, it varies only as a function of x and z. Inserting the expected form of solution $E_y(x,z) = E_y(x)\mathrm{e}^{-iz\beta^{TE}}$, which is a harmonic, transversal, TE-polarized wave, into the Helmholz equation (1.4) with $\varepsilon = \varepsilon(x) = n^2(x)$, one obtains:

$$\frac{\mathrm{d}^2 E_y(x)}{\mathrm{d}x^2} + k_0^2 n^2(x) E_y(x) = \beta^2 E_y(x) \tag{1.15}$$

This is an eigenvalue problem of a linear differential operator. Eigenvalues and eigenvectors give the propagation constant and the field distribution of the supported modes, respectively. Solution for the TM modes can be found in an analogous way.
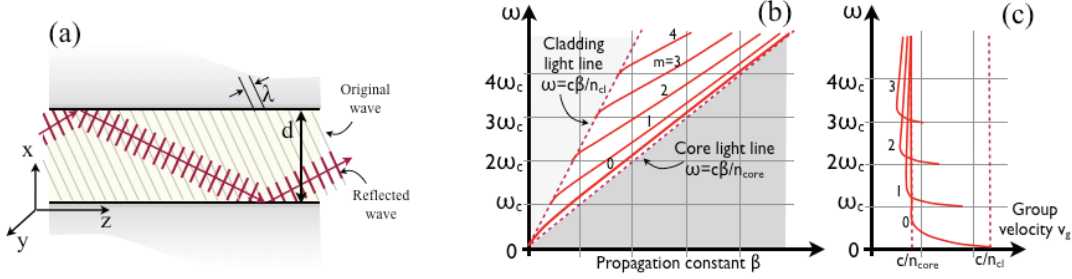
Figure 1.4: (a) Self-consistency condition for a planar waveguide (b) Dispersion diagram and group velocity of TE polarized modes of a planar waveguide.

Frequency dependence of the propagation constant yields the dispersion relation as shown for in Fig. 1.4(b). In a symmetric slab waveguide (same refractive index of the top and the bottom cladding), the fundamental mode $m = 0$ is always supported, while the higher order modes add progressively as soon as their characteristic cutoff frequency $\omega_{c,m}$ is reached. Above the cutoff, the propagation constant of each mode increases from $n_1 k_0$ towards $n_2 k_0$ and the optical field is becoming gradually more confined within the high index medium. In consequence, the dispersion curves of truly guided modes lie between the cladding light-line and the core light-line. Above the cladding light-line, the TIR condition is not satisfied and the modes are partially refracted into the cladding. We speak about radiative or leaky modes that are characterized by intrinsic out-of plane loss.

Group velocity of the guided modes is plotted in Fig. 1.4(c). Note that apart from small region at the mode cutoff, the group velocity is smaller than the phase velocity, which means that the optical information carried by the guided mode can propagate slower than in a homogeneous medium. This effect that results from strong spatial confinement of the mode is even more pronounced in two-dimensional waveguides where the light is confined at the scale of an optical wavelength.

1.2.2 Two-dimensional waveguides

Light guided in planar waveguides is vertically confined, but within the plane of the slab it diverges like in a homogeneous medium. In consequence, the majority of optical devices uses two-dimensional waveguides confining the light in both vertical and lateral directions. The principle of operation and the waveguide dispersion is analogous to the slab waveguides, only the mathematical description is more complex. However, note that in 2D waveguides there are no more pure TE and TM modes, only quasi-TE and quasi-TM modes that always have a weak, but nonzero component in the propagation direction. Moreover, in waveguide bends or in asymmetric waveguides, where the refractive indices of the top and the bottom cladding are not identical, quasi-TE and quasi-TM modes interact, resulting in polarization crosstalk. The modes become completely hybrid at frequencies where their dispersion curves anticross.

The 2D waveguides can be fabricated in different configurations as illustrated in Fig. 1.5 and on different material systems. Silicon on Insulator (SOI) waveguides based on a silicon strip on top of an oxide cladding are probably the most common, as their fabrication is compatible with the CMOS technology. At room temperature and telecom wavelengths of
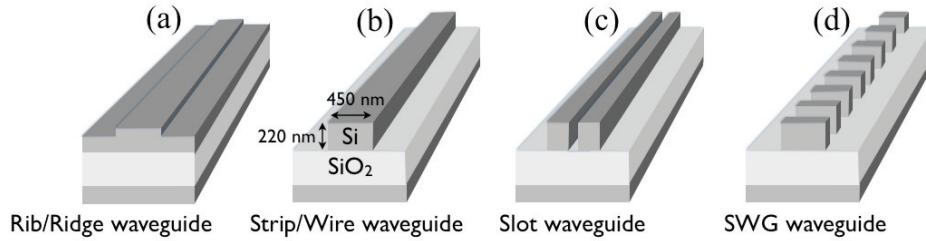
Figure 1.5: Two-dimensional waveguides in different geometries: (a) Rib or ridge waveguide, (b) Strip or wire waveguide, typical dimensions are also shown, (c) Slot waveguide, (d) Subwavelength grating (SWG) waveguide.

1550 nm, the core and bottom cladding layers have refractive indices of 3.48 and 1.44 (silica oxide), respectively. For typical cross-sectional dimensions of 500×220 nm^2, the effective index of the fundamental TE mode is about 2.4, while the group index is approximately twice as large due to strong waveguide dispersion [8]. Besides SOI waveguides, suspended strip waveguides supported by thin lateral pads or waveguides with both top and bottom oxide cladding can be used; these configurations eliminate the polarization mixing and can reduce the propagation losses, however their processing requires an additional fabrication step.
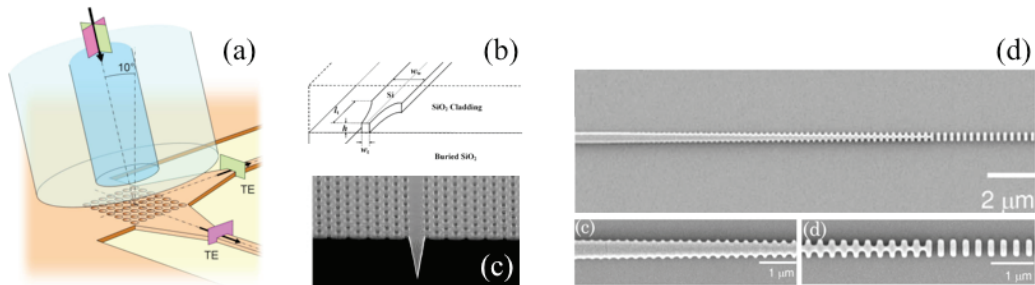
Figure 1.6: Tapering approaches for low-loss coupling between an optical fiber and a SOI integrated waveguides: (a) Vertical polarization-independent grating coupler [26], (b) Inverse taper (nanotaper) [27], [28], (c) Taper based on subwavelength grating waveguide [15].

There are four major issues to be addressed concerning wire SOI waveguides:

- *Propagation losses.* Propagation loss results from scattering due to sidewall roughness, substrate leakage and absorption at imperfect material boundaries [29, 30]. Residual scattering of the propagating mode can occur at the etching-induced roughness of the side walls, or at irregularities of the geometry introduced by e-beam patterning (stitching errors, proximity effects). Propagation losses of the state-of-the-art SOI waveguides are around 2 dB/cm, while in 1-μm radius 90°bends losses as low as 0.086 dB per bend can be achieved [31]

- *Coupling losses.* Coupling between optical fiber with a core radius of 9 μm and

strip waveguide of the cross-section of 500×220 nm^2 necessarily results in loss due to poor spatial matching of the respective mode profiles. Two working schemes were proposed to substantially improve the coupling efficiency: vertical coupling using grating couplers [32] or tapering of the strip waveguides and subsequent butt-coupling using a lensed fiber or microscope objective. Different taper designs are shown in Fig. 1.6; for instance, the subwavelength grating taper reduces the coupling loss to as little as 0.24 dB per interface [15].

- *Polarization dependence.* Due to distinctly different properties of TE and TM modes it is virtually impossible to produce polarization independent circuits. Square cross-section might solve the problem, however, even small geometrical discrepancy leads to strong birefringence. At the moment, the only solution is the polarization diversity, *i.e.* coupling the TE and TM polarizations into two different waveguides and processing them in separate circuits.

- *Temperature dependence.* The temperature dependence of the refractive index in silicon is high, about 1.8×10^{-4}/K at 1530 nm. Since the temperature of the current processors changes easily by $\pm 15°C$ during operation, resulting refractive index change has a detrimental effect on function of all spectrally sensitive devices like Si-based filters or multiplexers. Despite some preliminary achievements [12], this issue has yet to be solved.

1.3 Photonic crystals

Photonic devices that comprise multiple dielectric materials arranged in a periodic manner can confine and guide light by an effect physically different from the total internal reflection, namely the photonic bandgap effect. In periodic devices, light propagation is dictated by multiple scattering and interference at the dielectric *lattice*, which gives existence to frequency bands where the wave propagation is allowed and bandgaps where no waves can propagate as a result of destructive interference. Similar phenomena occur in electronic crystals, where electron scattering at periodic lattice of atoms gives rise to electronic band structure [33]. Therefore, optical devices that exhibit periodic modulation of the dielectric constant are called *photonic crystals* [34–36]. The simplest one-dimensional periodic structure also known as multi-layer stack or Bragg mirror has been studied since the beginning of the 20$^{\text{th}}$, however, the genuine scientific interest in photonic crystals started in 1970's (Bykov [37])) when the generalization of 1D-stacks to higher dimensions was proposed (Bykov [37]) and terms like 'photonic bandgap' were first formulated. The practical photonic crystal devices working at optical wavelength emerged only 20 years later owing to the immense progress in nanoscale fabrication technology.

1.3.1 One dimensional photonic crystals

Bloch-Floquet theorem. Let's assume the simplest, one-dimensional photonic crystal that exhibits periodic modulation in one direction z (see Fig. 1.7) and remains homogeneous in the two other directions. Such a structure is formed by a dielectric unit called *the unit cell* that is repeated along z with the basic step given by the *lattice constant a*: $\varepsilon(z) = \varepsilon(z+a) = \varepsilon(z+ma)$, where m is an integer. We say that the structure has a discrete translational symmetry in the z-direction. According to the the Bloch-Floquet theorem

[33], such discrete translational symmetry implies an electromagnetic wave solution in form of a product of a plane wave propagating in the z-direction and a function $\mathbf{u}(z)$ that is periodic in z with period determined by the lattice constant:

$$\mathbf{E}_{k_z}(z) = E_0 \mathrm{e}^{ik_z z} \mathbf{u}_{k_z}(z) \tag{1.16}$$

In other words, the electromagnetic wave in a periodic medium is actually a plane wave modulated by a periodic function due to the periodicity of the lattice.

One key consequence of the Bloch theorem is that the wave solutions (also called the Bloch states) with k_z and $k_z + m\,2\pi/a$ are identical and have therefore the same optical frequency $\omega(k_z) = \omega(k_z + 2\pi m/a)$. Hence, the dispersion diagram is periodic in the k_z direction with period equal to the *reciprocal vector* of the lattice $\mathbf{G} = 2\pi/a$. To investigate the dispersion properties of photonic crystals, we can restrict ourselves to one period, which is typically chosen such that $-\pi/a < k_z < \pi/a$, called the first Brillouin zone.

Origin of the photonic bandgap. Consider the propagation of an electromagnetic wave along the z-direction in three different 1D photonic crystals shown in Fig. 1.7. The first one exhibits a negligible indext contrast and it can be considered homogeneous with an artificially induced periodicity. The corresponding dispersion diagram is a straight light line as in section 1.1, just folded by the reciprocal vector of the lattice (Fig. 1.7(a)).
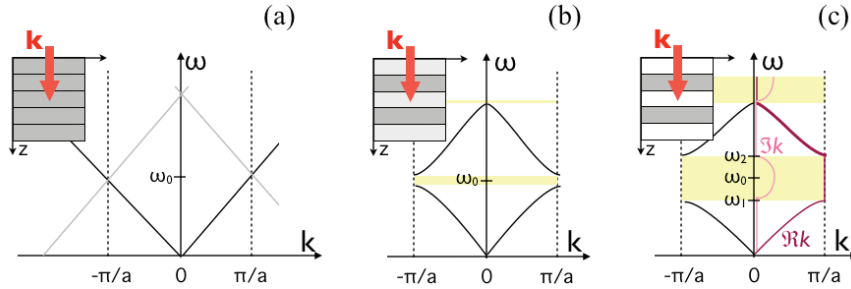
Figure 1.7: (a) Band folding in a periodic 'empty' lattice. (b) bandgap is formed when the refractive index contrast is introduced. (c) The bandgap increases with the refractive index contrast. Real and imaginary part of the k-vector is plotted at the right.

Increasing the refractive index contrast leads to coupling between the optical modes at the points where their folded dispersion curves (anti)cross. As the optical wave propagates within the photonic crystal, it is diffracted by the periodicity of the lattice. At certain locations, which coincide with either the centre of the Brillouin zone or the Brillouin zone boundaries, the diffracted light can couple into counter-propagating wave by means of the reciprocal vector of the lattice $\mathbf{G} = 2\pi/a$. The coupling of the forward ($k = \pi/a$) and the backward propagating wave ($k = -\pi/a$) results in splitting of the originally degenerate state into two states at frequencies ω_1 and ω_2. Since there are no extended states that exist in the frequency range between the two states, one speaks about opening of the photonic bandgap as illustrated in Fig. 1.7(b). The spectral width of the bandgap increases as a function of the refractive index contrast between the dielectric layers (Fig. 1.7(c)).

The lower-energy state (ω_1) has optical field concentrated in the high index layers and the higher-energy state (ω_2) in regions with low refractive index. It is a consequence of

the variational theorem [34]: Mode tends to concentrate its displacement field inregions of high dielectric constant while remaining orthogonal to the modes of lower frequency. Since the high index medium is often a dielectric and the low index medium the air, the photonic band found below ω_1 is called the *dielectric band*, while the photonic band of $\omega > \omega_2$ the *air band*.

Evanescent states. Although there are no extended states in the bandgap, if a light wave is incident at the air/photonic crystal interface, exponentially decaying states with complex k-vector will be excited. If the imaginary component k-vector is small, these states can penetrate rather deep into the photonic crystal lattice and significantly influence on operation of practical finite-size devices. The role of the evanescent states can be both positive and negative. If they are coupled with extended states, they can represent a leakage channel for the energy and thus increase the propagation loss. On the other hand, they may facilitate coupling into specific guided modes such as slow-light modes discussed later in chapter 6). As the frequency is scanned across the photonic bandgap, the imaginary k increases reaching maximum at the band center and converges back to 0 at the band edge as depicted in Fig. 1.7(c).

1.3.2 Two dimensional photonic crystals

Purely two-dimensional photonic crystals exhibit periodic modulation in two dimensions, while they are homogeneous in the third dimension. The physics beyond the light propagation in two-dimensional lattice is similar to 1D crystals: Bloch states and band-structure formation is governed by the same principes as in the case of simple one-dimensional lattice. Additional dimension, however, increases the complexity of the problem in the following aspects:
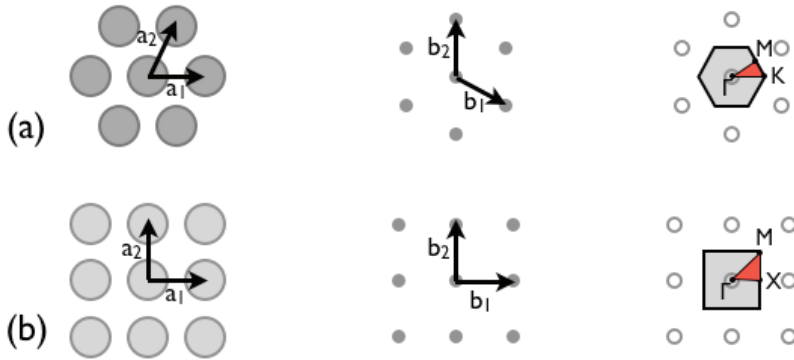
Figure 1.8: Lattice, reciprocal lattice and 1st Brillouin zone of the (a) triangular and (b) square photonic crystal. Geometrical position of the principal symmetry points is indicated for both symmetries.

Two dimensional lattice. Periodicity in two dimensions can be realized in various geometries, the most common are the square and the triangular lattice shown in Fig. 1.8. The lattice is defined by two lattice vectors $\mathbf{a}_1$ and $\mathbf{a}_2$ that can be chosen arbitrarily. Each

set of direct lattice vectors defines two the reciprocal lattice vectors $\mathbf{b}_1$, $\mathbf{b}_2$, $\mathbf{b}_i \cdot \mathbf{a}_i = 2\pi\delta_{ij}$, which specify the reciprocal lattice.

Since two-dimensional photonic crystals are not isotropic, the dispersion diagram has to be specified in all possible propagation directions, *e.g.* as a 2D dispersion map or as its projection into the principal directions of propagations. Fig. 1.9 shows an example of the dispersion map and the dispersion band diagram of photonic crystal of triangular lattice plotted along the three principal dispersion paths: Γ−K, Γ−M, M−K. For TE polarized light, a photonic bandgap opens at both K amd M symmetry points. The frequency range where the two bandgaps overlap defines the so-called omnidirectional photonic bangap, where reflection occurs independently of direction of the incident wave. The TM polarization does not exhibit any bandgap due to degeneracy of the dispersion bands at the K-point.
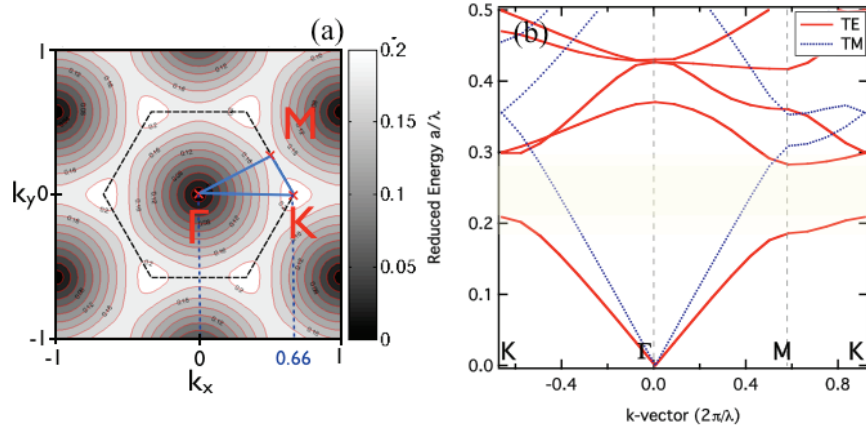
Figure 1.9: (a) Two-dimensional dispersion map od the dielectric band of a photonic crystal with a triangular lattice of air-holes in silicon, air-filling factor is equal to 35%. (b) Dispersion diagram, *i.e.* the projection of the dispersion map into principal crystallographic directions, calculated for the same device as in (a) for both TE and TM polarizations.

Besides the refractive index contrast and the lattice symmetry, another crucial parameter that determines the spectral position and width of the photonic bandgap is the filling factor, *i.e.* the fraction of low-dielectric (hole) surface with respect to the entire surface of the unit cell. Unlike in one-dimensional photonic crystals where the bandgap opens as soon as nonzero index contrast is present, in 2D the full bandgap exists only for filling factors within a specific interval of values. For instance, filling factor of approx. 0.18 is required to create a bandgap for TE polatization in a triangular lattice of air-holes.

Polarization.   In two-dimensional lattice, light can propagate in two orthogonal polarizations: TE with nonzero E_x, E_y and H_z components, and TM polarization with H_x, H_y and E_z. The two polarizations have different bandstructures and their bandgaps don't overlap except for carefully engineered devices. Dielectric bulk with air holes favours opening of the TE bandgap, while the TM bandgap is prevailingly found in pillar-type structures, such as dielectric pillars in the air.

Group velocity.   In the vicinity of photonic bandgaps, one can observe a strong deviation from the linear dispersion dependence that is characteristic for homogeneous medium. The dispersion curves get flatter, which results in a decrease of the group velocity that converges to zero at the actual band edge. The *slow light* allows for creation of broad-area modes where the propagating light is reflected into counter-propagating modes and vice versa, which provides *e.g.* satisfactory optical feedback to trigger the laser action. Band edge modes are often used in vertically emitting photonic crystal lasers in the spectral range from visible to terahertz [38–40].

As illustrated in 2D dispersion map in Fig. 1.9(a), at the proximity of the band edges the equifrequency surfaces deviate from circular shape, as expected for strongly anisotropic media. The direction of the group velocity, which is by definition always perpendicular to the isofrequency lines (Eq. 1.7), strays from the direction of phase velocity leading to interesting phenomena like self-collimation, superprism effect or negative refraction. *Self-collimation* occurs at frequencies where the dispersion isolines are flat; whatever the incident angle, the group velocity and hence, the energy carried by the optical beam, propagates in a single direction, the beam gets collimated (Fig. 1.10(a)) [19]. The *Superprism effect*, on the other hand, makes use of sharply curved equifrequency surfaces to induce strong dependence of the refracted light direction on the angle or frequency of the incident light (Fig. 1.10(b)) [41]. Finally, *negative refraction* at the proximity of certain photonic band edges, which exhibit circular isofrequency contours and negative dispersion slope around the Γ-point [42]. This results in anomalous refraction, similar as observed in left-handed materials.
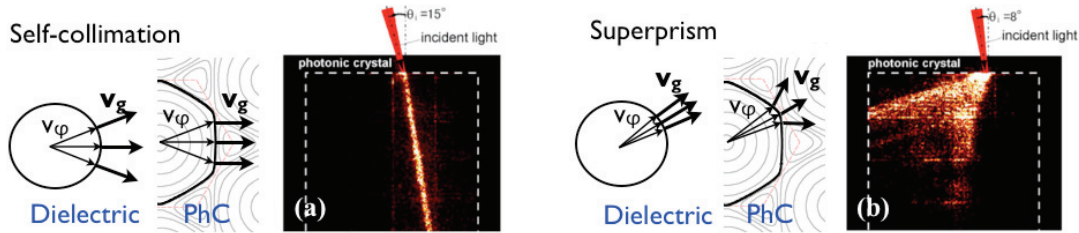
Figure 1.10: (a) Self-collimation and (b) superprism effect explained in terms of group velocity that must be perpendicular to equifrequency contours. Experimental demonstration of both effects was presented in 1999 by H. Kosaka et al. [19, 41]

1.3.3   2D Photonic crystals in dielectric slab

Despite many intriguing properties of 2D photonic crystals, they are by definition infinite in one direction and consequently not suitable for practical applications. The only exception are photonic crystal fibers which can be viewed as a special type of 2D photonic crystal of radial symmetry. In integrated optics, photonic crystals based on slab waveguides are much more common as they can truly confine the light in both direction perpendicular to the direction of propagation. The vertical confinement within the plane of the slab is provided by the total internal reflection, whilst the light propagation in the plane is dictated by the photonic crystal lattice.

Fig. 1.11 compares the dispersion bandstructure of an ideal two-dimensional photonic

crystal and a slab-based photonic crystal. The shape of the dispersion is similar, however, the dispersion curves of the slab waveguide are stretched in frequency due to vertical mode confinement and slightly modified in shape by inherent dispersion of modes of the planar waveguide. Furthermore, as in the case of a simple dielectric slab discussed in section 1.2.1, the lightline argument applies; all modes that are found above the cladding light line can radiate out-of-plane, thus accounting for high propagation loss. Finally, the eigenmodes of the slab PhC waveguide are no longer purely TE and TM polarized, however, still classified as quasi-TE (E_x, E_y, $E_z = 0$, H_x, H_y, H_z) and quasi-TM (E_x, E_y, E_z, H_x, H_y, $H_z = 0$). Both polarizations can interact if the vertical symmetry of the structure is broken, *e.g.* in SOI material system where the top (air) and the bottom (silica) claddings exhibit different refractive indices [43].
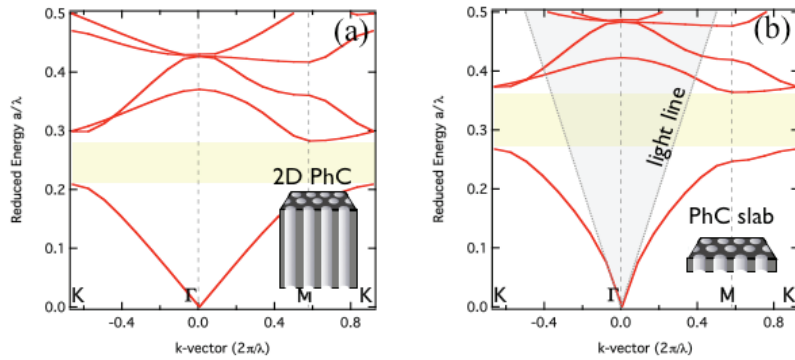
Figure 1.11: (a) Dispersion diagram of an infinitely long, two-dimensional photonic crystal with a triangular lattice of air-holes in silicon. The air-filling factor $f = 35\%$. (b) Dispersion diagram of a 2-D photonic crystal in a 220-nm thick silicon slab surrounded by the air. Other structural parameters are identical as in (a).

1.3.4   Defects in two-dimensional photonic crystals

Any irregularities of the periodic photonic crystal lattice affect the Bloch mode propagation, which gets either scattered at the defects, or localized. In the latter case, the defect gives rise to new 'defect' states, which can be represented as a superposition of all states supported by the photonic crystal, both extended and evanescent. If the new state is found in the photonic bandgap, the field remains localized at the defect position and decays exponentially into the bulk photonic crystal. In two dimensional slab-based photonic crystals we can classify the defects in respect to their dimensionality as 0-dimensional (0D or point defects) and one-dimensional (1D or line defects).

Cavities

Point defects in 2D photonic crystal lattice, or so-called photonic crystal cavities, are created by removing, adding or shifting the position of one or more lattice 'atoms', *i.e.* holes or pillars. If carefully designed, such cavities can achieve extremely high quality factors Q $\sim 10^6$ and strong field confinement [44, 45], resulting in enhanced light–matter interaction within an extremely small volume. Fig. 1.12 plots some typical examples of cavity

geometries. Photonic crystal cavities find a vast number of applications in telecommunications [46], lasers and quantum electrodynamics [47] nonlinear physics [48] and, based on experimental demonstrations achieved to date, they also constitute a promising building block for optical (bio)sensors [22,49,50]. A special attention has been payed to interaction between the cavity mode and a light source, *i.e.* a quantum dot, embedded in the cavity. Effects like spontaneous emission supression, enhancement and strong coupling have been observed experimentally. Other important applications include laser cavities, filters, polarisation splitters, wavelength division multiplexers as well as recent applications in cavity opto-mechanics.
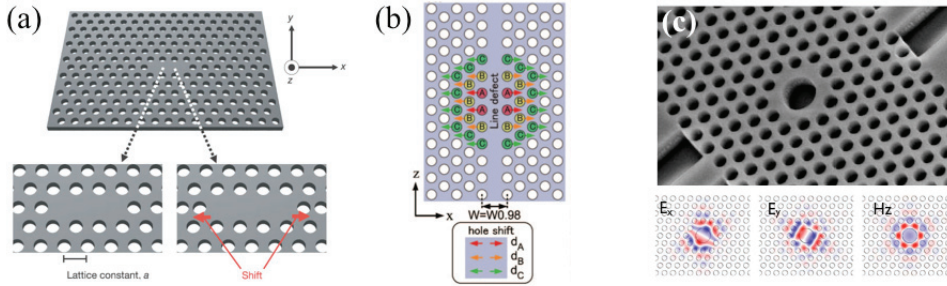
Figure 1.12: (a) L3 and modified L3 cavity by T. Asano et. al [45]. (b) High-Q cavity with lateral shift of holes proposed by Kuramochi et. al. [44], Photonic crystal cavity for optical trapping and sensing applications by M. R. Lee et. al. [51]

Optical cavities concatenated in a chain create a special type of optical waveguide, the so called Coupled-cavity waveguide [52, 53]. Such waveguides are characterized by low group velocity, quasi-zero group velocity dispersion, and hence, they have a large application potential as optical buffers or delay lines.

Waveguides

If one or more lines of 'atoms' are removed from the photonic crystal lattice, optical field of the created defect state is confined in the direction perpendicular to the defect, but can delocalized and become guided along the defect as in a standard one-dimensional optical waveguide. The most famous example of a line defect photonic crystal waveguide is the W1 waveguide depicted in Fig. 1.13 that is created by removing 1 row of holes in the $\Gamma-K$ direction. As shown in Fig. 1.14(a), such a waveguide support two TE-polarizad modes, even and odd, found inside the first bandgap of the bulk photonic crystal cladding.

The projected band structure. The position of the bandgap in one-dimensional dispersion plot can be conveniently visualized by so-called projected band structure of the photonic crystal mirror. In fact, the dispersion of the supported line-defect mode is strictly defined only in the direction of propagation z. As soon as the mode overlaps in frequency with a 2D dispersion band of the photonic crystal cladding, it can couple with any of the Bloch modes with identical k_z component, independently of the k_y value. This can be illustrated in the reciprocal space as in Fig. 1.14(b): for a given frequency ω, all possible
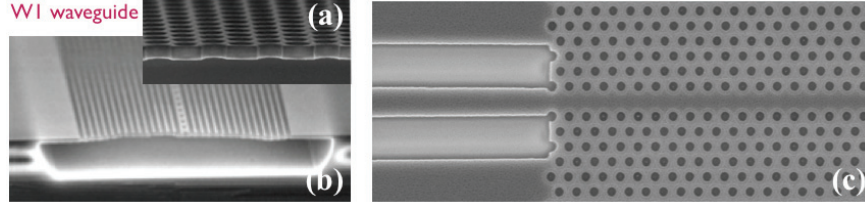
Figure 1.13: (a), (b) SEM image of the W1 waveguide in triangular photonic crystal lattice suspended in the air and (c) its top-view image.

Bloch modes along $k_z = const$ are considered. If there are no Bloch states with given k_z, the line defect mode is truly guided within the photonic crystal plane. However, if such Bloch modes exist, they represent a leakage channel for the defect mode, thus breaking its lateral confinement.

The set of points (ω, k_z) for which a Bloch solution exists forms the so-called projected band diagram of the photonic crystal cladding, as depicted by gray shaded region in Fig. 1.14(a). In this context, the boundary of the projected band structure can be considered as a *lightline* of the lateral photonic crystal cladding; as soon as the originally guided modes crosses such a boundary, it becomes leaky through coupling with the continuum of extended states of the photonic crystal environment. Conversely, the light cone can be regarded as a projected band diagram of the top/bottom cladding of the slab waveguide as also illustrated in Fig. 1.14 (c).

Photonic crystal W1 waveguides can guide light with propagation loss comparable to nanophotonic wire waveguides (5 dB/cm [18, 54]). In addition, they can realize sharp,
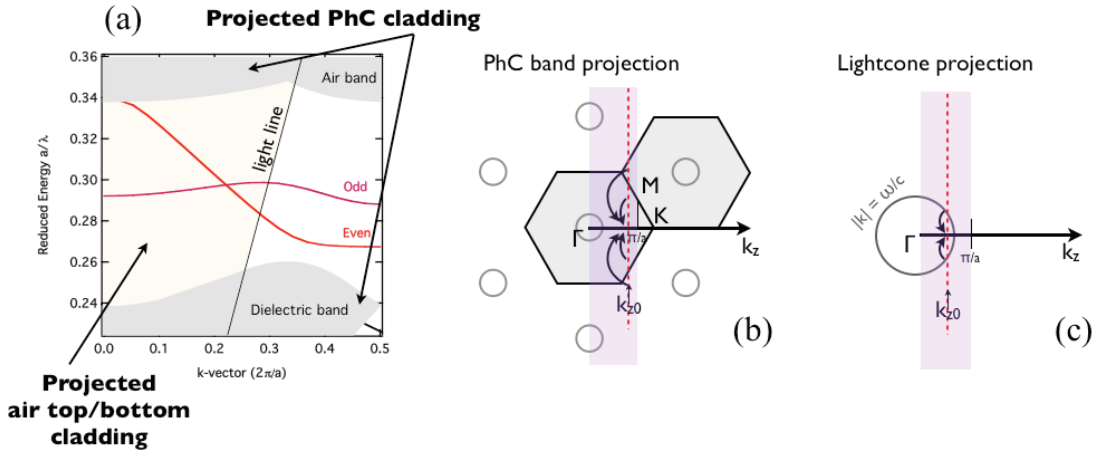
Figure 1.14: (a) Dispersion diagram of a single line defect photonic crystal waveguide (W1 waveguide) processed in a silicon membrane, with lattice constant $a = 420$ nm and air-filling factor equal to 30%. Projected band diagram of the photonic crystal cladding is shown in grey. (b), (c) Schematic illustration of the photonic band projection along a given direction k_z for the photonic crystal and air top/bottom cladding, respectively.

virtually lossless bends and corners thus enable to control the direction of light at the wavelength scale. Nevertheless, a lot of effort have been invested into optimization of such bends (changing the number, size or position of holes at the bends) to avoid spurious back-reflection loss within a reasonable operation bandwidth [55, 56].

W1 waveguides are also intensively studied as a possible candidate for slow light applications [57], as they exhibit a region of flat dispersion in the proximity of the mode cutoff. This region can be extended and linearized by adjusting the size or/and position of holes in the vicinity of the line defect [58, 59]. In such slow-light engineered waveguides, light speed reduction by a factor of ~ 30 within the bandwith of approx. 10 nm has been achieved. Two W1 waveguides coupled laterally can also support slow optical modes with quasi-zero group velocity dispersion as has been recently demonstrated by the group of T. Baba [60, 61].

1.3.5   Three dimensional photonic crystals

3D-complete photonic bandgap, *i.e.* a common bandgap for all directions and polarizations, can be achieved only in 3D photonic crystals, which exhibit periodic modulation of the dielectric constant in all three orthogonal directions. The first 3D-photonic crystal geometry fabricated in 1989 and investigated experimentally was the face-cubic centered (fcc) lattice [62], which was found, however, to not to open omnidirectional bandgap even for an index contrast as high as 4 and filling factor of 96% [63]. After this failure, different working designes mostly based on diamond lattice were proposed, which include:
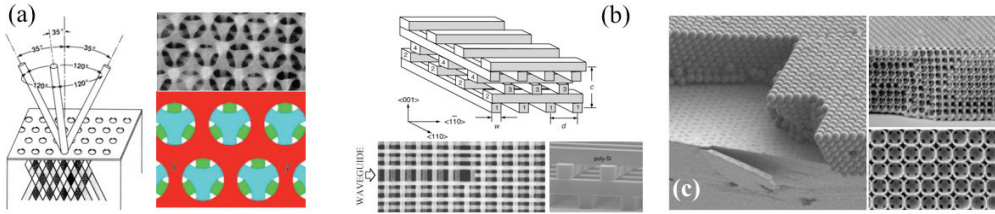
Figure 1.15: (a) The Yablonovite: Schematic drawing of the fabrication procedure by hole drilling [64], top view SEM [65] and hand-drawn [66] image of the structure. (b) The woodpile structure: Schematic drawing [67] and SEM images [67, 68]. (c) Opals and inverse opals [69]

- *Yablonovite* [64]. The Yablonovite is fabricated by drilling holes at specific angles (120°) with inclination of 35°, *e.g.* by means of focused ion beam. (see Fig. 1.15(a))

- *Woodpile structure* [67, 68, 70]. It has a diamond symmetry and could be made layer-by-layer by stacking pre-patterned silicon wafers or rods in crisscross fashion. (see Fig. 1.15(b))

- *Inverse opals.* Artificial opals can be processed from silica or polystyrene colloids by self-assembly techniques suitable for mass production. The spheres assemble in closed packed fcc geometry, which does not exhibit a bandgap, but the inverted structure has one. The inversion is done by infiltrating high index material such as

as silicon into the voids of opal structure and subsequent etching of the spheres [69]. (see Fig. 1.15(c))

An inconvenience of 3D photonic crystal is that, once fabricated, their dispersion properties including bandgap behavior cannot be easily altered or engineered for practical functions. Moreover, the controlled introduction of defects is hard to achieve. Both issues were rather successfully challenged in recent publications [71, 72]

1.3.6 Electromagnetic formulation and numerical simulation

The dispersion band structure render complete information about electromagnetic wave propagation in photonic crystals. It defines the position and the width of the bandgaps, as well as direction and velocity of propagation of Bloch modes within photonic bands. Theoretical calculation of dispersion, however, requires to solve the full vectorial Maxwell's equations 1.1 in a periodic medium, which is a complex task requiring the use of numerical tools, especially if 2D or 3D photonic crystals are involved.

Assuming linear and lossless dielectric medium and harmonic wave solution, the Maxwell's equations can be simplified to so-called master equation for the magnetic field:

$$\nabla \times \frac{1}{\varepsilon(\mathbf{r})} \nabla \times \mathbf{H}(\mathbf{r}) = \frac{\omega^2}{c^2} \mathbf{H}(\mathbf{r}) \tag{1.17}$$

The master equation represents an eigenvalue problem for a Hermitian operator $\Theta = \nabla \times \frac{1}{\varepsilon(\mathbf{r})} \nabla \times$. For a given k-vector, the eigenvalues of the problem give the allowed frequencies, *i.e.* the dispersion relation, and the eigenvectors yield the field distribution of the corresponding Bloch modes.

Scaling properties One interesting property of photonic crystals is the scalability of their optical properties in respecto to the length and the dielectric constant, as can be easily demonstrated from the master equation. If the length scale of the dielectric constant distribution is compressed by a factor s, *i.e.* $\varepsilon(\mathbf{r}') = \varepsilon(\mathbf{r}/s)$, after changing the variables in Eq.(1.17) a new equation is obtained:

$$\nabla \times \frac{1}{\varepsilon(\mathbf{r}')} \nabla \times \mathbf{H}(\mathbf{r}') = \frac{s^2 \omega^2}{c^2} \mathbf{H}(\mathbf{r}') \tag{1.18}$$

which is again a master equation, but with compressed mode profile $\mathbf{H}(\mathbf{r}') = \mathbf{H}(\mathbf{r}/s)$ and s-times higher frequency $\omega' = s\omega$. Similarly, when dividing the dielectric constant by the factor s^2, $\varepsilon(\mathbf{r}') = \varepsilon(\mathbf{r})/s^2$, the optical frequency scales ($\omega' = s\omega$), however, the field $\mathbf{H}(\mathbf{r})$ remains unchanged.

The scalability of photonic crystal makes it possible to tune their dispersion properties as required for particular applications. For instance, one can fit the bandgap into desired frequency range by pure squeezing or stretching the photonic crystal lattice (so-called lithographic tuning). It is therefore often convenient to introduce dimensionless units for the wave vector and frequency, namely the reduced wave vector $\mathbf{k}'$ and the reduced

frequency u:

$$\mathbf{k}' = \frac{a}{2\pi}\mathbf{k} \tag{1.19}$$

$$u = \frac{a}{2\pi c}\omega = \frac{a}{\lambda} \tag{1.20}$$

where a is the photonic crystal lattice constant and λ is the vacuum wavelength. The reduced units $\mathbf{k}'$ and u uniquely identify the Bloch state independently of the spatial scaling of the photonic crystal.

1.3.7   Numerical calculation methods.

There is a large variety of algorithms that can be employed to solve the master equation. The final choice depends on the complexity of the structure (infinite periodic or non-periodic), the desired calculation output (dispersion or transmission) and last but not least, the available time and computational facilities.

Plane wave expansion method (PWE)

The Plane wave expansion method initially proposed by M. Plihal *et. al.* [73] and K. M. Ho *et. al.* [74] is based on decomposition of both the fields and dielectric function into plane waves. In 2D, the plane wave decomposition takes the following form:

$$E_z(\mathbf{r}) = \mathrm{e}^{i\mathbf{kr}}\sum_m A_m \mathrm{e}^{i\mathbf{G}_m\mathbf{r}} \qquad\qquad \text{for TM polarization} \tag{1.21}$$

$$H_z(\mathbf{r}) = \mathrm{e}^{i\mathbf{kr}}\sum_m B_m \mathrm{e}^{i\mathbf{G}_m\mathbf{r}} \qquad\qquad \text{for TE polarization} \tag{1.22}$$

$$\frac{1}{\varepsilon(\mathbf{r})} = \sum_m \eta_m \mathrm{e}^{i\mathbf{G}_m\mathbf{r}}, \qquad \frac{1}{\mu(\mathbf{r})} = \sum_m \theta_m \mathrm{e}^{i\mathbf{G}_m\mathbf{r}} \tag{1.23}$$

Such a decomposition allows to simplify the master equation (1.17) into a matrix eigenvalue problem (magnetic permeability $\mu(\mathbf{r}) = 1$):

$$\sum_n C_n(\mathbf{k}) \cdot |\mathbf{k}+\mathbf{G}_n| \cdot |\mathbf{k}+\mathbf{G}_m| \cdot \eta_{m-n} = \frac{\omega^2}{c^2}C_m(\mathbf{k}) \qquad \text{for TM polarization} \tag{1.24}$$

$$\text{where}\quad C_m(\mathbf{k}) = |\mathbf{k}+\mathbf{G_m}| \cdot A_m(\mathbf{k})$$

$$\sum_n B_n(\mathbf{k}) \cdot (\mathbf{k}+\mathbf{G}_n) \cdot (\mathbf{k}+\mathbf{G}_m) \cdot \eta_{m-n} = \frac{\omega^2}{c^2}B_m(\mathbf{k}) \qquad \text{for TE polarization} \tag{1.25}$$

$$\tag{1.26}$$

where the eigenvalues provide the optical frequencies of Bloch modes for a given $\mathbf{k}$ and corresponding decomposition coefficients, *i.e.* eigenvectors, allow to reconstruct the full electromagnetic field. The advantage of this method is that it can be used for almost any photonic crystal structure (complex structures use the super-cell approach), it yields directly the dispersion diagram and it gives a good insight into the physics of photonic crystals.

Modification of this method proposed in [75] uses an alternative approach: fix the

frequency and scan the k-space in order to find the appropriate solutions. Such an inverse task allows to find both real and imaginary components of the wave vector **k** and, hence, calculate the radiation losses and the dispersion of the evanescent modes. It makes is also feasible to account for the dispersion of dielectric permittivity (and permeability). However, plane wave expansion in any of its modifications it is not appropriate to calculate properties of large non-periodic devices (calculation time increases rapidly with the size of the supercell), finite structures, and is not capable of calculating the transmission/reflection spectra.

Dispersion of slab-based 2D photonic crystals can be calculated using an alternative method, namely the **Guided mode expansion** (GME) [76]. This method uses guided modes of the dielectric slab instead of plane waves as the basis set for the Bloch mode decomposition, and in this way it allows to shrink the full three dimensional problem into two dimensions, while taking into account the slab dispersion. As experimentally demonstrated in the next chapters of this thesis, the GME method is in ideal tool for simulation of slab-based photonic crystals: it allows to reproduce the experimental dispersion to a large degree of precision, and at the same time it saves the computational time compared to full 3D PWE.

All photonic band structure calculations presented in this work were performed using 2D PWE and GME routines developed by D. Leuenberger [35] and V. Zabelin [77]. The PWE method combined with effective index approach allows us to quickly and accurately simulations dispersion properties of two-dimensional PhC devices; it can calculate the dispersion diagram, 2D full dispersion maps and electromagnetic field distribution of the supported Bloch modes. It uses the perturbation theory to rapidly calculate the variation of dispersion properties upon fine tuning of structural parameters. Last but not least, frequency-based modification of the PWE method is implemented, allowing for calculation of both the real and imaginary part of the wave-vectors.

The GME method is used for dispersion calculations of 2-dimensional photonic crystals in thin dielectric slabs (typically 220 nm). Unfortunately, up to this date, the GME tool does not allow to simulate the field-distribution, nor calculate the optical loss.

Finite difference time-domain methods (FDTD).

FDTD is widely use to calculate the transmission and reflection spectra of any photonic device including photonic crystals, however, it is not very suitable to solve for the dispersion relation. Moreover, it is a 'black box' method, which does not facilitate the physical understanding, it is extremely time consuming and requires a *smart* choice of initial and boundary conditions to excite all the desired Bloch modes and to avoid spurious reflections due to finite size of the calculation area.

The FDTD-based Crystal Wave software package by Photon Design is used in our group to simulate the temporal evolution of light propagation, as well as transmission and reflection spectra.

Finite element method (FEM)

FEM is a frequency domain method based on variational principle. It allows to calculate system eigenmodes, and hence, the dispersion relation including the mode profiles. Material discontinuities can be treated more efficiently than in the case of PWE.

We use the commercial FEM-based COMSOL simulation software to calculate the dispersion and electromagnetic distribution of optical defects and cavities, including their quality factors and optical loss.

Transfer matrix method

For completeness, the Transfer matrix method divides the structure into layers and solves the propagation of light through the media using scattering matrices of individual layers. It is less universal as the scattering centres (*i.e.* the photonic crystal 'atoms') have to be arranged in layers.

Film mode matching method by J. Čtyroký (initially proposed by A. S. Sudbo [78]) and CAMFR Maxwell solver developed at INTEC, Ghent University, fall into this category. Both methods were used to calculate the dispersion properties of non-periodic nanophotonic waveguides discussed in the fourth chapter of this thesis.

Chapter 2

Fabrication techniques for nanophotonics

High index contrast photonic nanostructures are characterized by dimensions that are of the order of, and typically smaller than the wavelength of light for which they are designed. In devices intended for telecom applications that operate at near-infrared wavelengths the smallest features scale down to one hundred nanometers, and the requirements on their precision are of order of one nanometer. Such devices call for mature nano-scale machining technology, that should, ideally, allow for cheap and massive production.

Because of similar size scale, material, and precision requirements, the same technology is used to process both the TIR-based nanostructures and the photonic crystal devices. Although certain photonic bandgap materials appear in nature (silica opals or tissue of certain butterfly wings, peacock feathers, etc.), they are extremely rare and introduction of defects as well as scaling of their dispersion properties to desired wavelengths cannot be easily achieved. In particular, 2D slab-based photonic crystals dealt in this thesis, with carefully designed and well-defined material properties, can be processed only artificially.

The state of the art fabrication process is based on the following steps:

- Lithographic patterning of the structures using deep UV or electron beam lithography.

- Pattern transfer to the design layer, typically by dry etching of the device layer.

- Buried oxide removal to achieve vertically symmetric structures, such as free standing membranes. This step is omitted in SOI-based structures, or can be replaced by deposition of the top cladding oxide layer.

All three technological steps are subject to variations dependent on particular material system; the process flow used for SOI-based structures treated in this thesis is schematically shown in Fig. 2.1, and each of the steps will be detailed below.

Several modification of the above listed fabrication steps are possible; an example includes etchless silicon waveguides formed by thermal oxidation reported by Cardenas et. al. [79]. Such waveguides are fabricated by selective oxidation of extremely thin silicon layer buried within the silica cladding, which produces ultra-smooth sidewalls with roughness as small as 0.3 nm, compared to standard values of 5 nm for etched sidewalls [30]. The

SOI Process Flow   Si Membrane
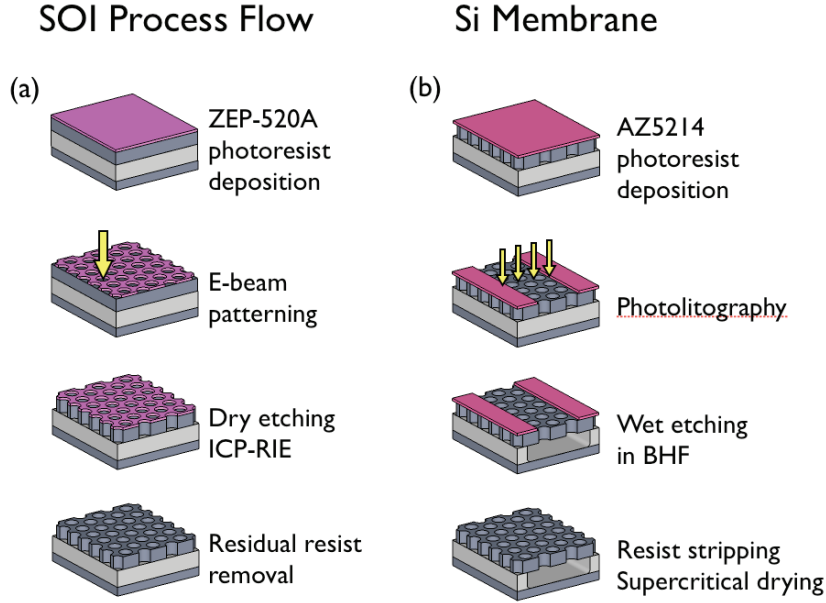
Figure 2.1: Schematic image of the process flow used at EPFL to fabricate Silicon-based nanophotonic devices and photonic crystals. (a) Fabrication of the SOI devices using E-beam patterning and Inductively Coupled Plasma Reactive Ion Etching (ICP-RIE). (b) Buried oxide removal by wet etching in BHF.

waveguides have a propagation loss of 0.3 dB/cm at 1.55 μm, however, the price to pay are larger dimensions (width of 1 μm) and weaker lateral field confinement.

For completeness, it should be mentioned that there are ongoing attempts to fabricate different nanophotonic structures, in particular photonic crystal devices, by direct writing using focused ion beam [80,81]. With exception of few working grating-based devices made by this technique [82], the optical quality is generally too low for practical applications.

2.1 Lithographic patterning

Standard ultra-violet (UV) lithography uses light to transfer a geometric pattern from the photo mask to a light-senitive photoresist. From the photoresist, the pattern is translated to the device layer by etching. Historically, the wavelength of the UV light sources used for lithography has decreased from ≈ 400 nm to presently used 193 nm line of ArF excimer lasers. Combined with liquid immersion optics, the smallest possible feature sizes that can be achieved with193 nm lithography are of the order of 50 nm, and are being currently reduced beyond 22 nm. Such resolution is already satisfactory to define the majority of nanophotonic devices based on semiconductor material systems. The main advantage of the deep-UV lithography is its potential for massive production and ability to expose large areas, which is inevitable for successful technology transfer to industry. The technique was adopted by our collaborating partners at IMEC (Interuniversitary Micro-electronic Centre, Belgium) [83] to pattern arrayed waveguide circuits and photonic crystal structures investigated in the Chapters 4 and 7 of this thesis, respectively.

Holographic lithography represents an alternative to standard lithography that can be

used to pattern periodic structures such as photonic crystals. By simultaneous exposure of the resist with several coherent laser beams, a two or three dimensional interference pattern is formed, defining the low or the high index regions. This technique has intriguing applications especially in combination with electron beam writing that allows to create defects in otherwise perfectly periodic structure [36].

2.1.1 Electron-Beam Lithography

Nanophotonic devices of the best optical quality are achieved by direct electron beam writing, *i.e.* the *Electron Beam Lithography*. Current e-beam machines allow for an exquisite resolution of ≈ 1 nm, they can expose any type of pattern on a large variety of available resists, and are therefore often the first choice in research and prototyping activities. The drawback is slow exposure speed that results from the serial nature of the writing process where the pattern is exposed point by point, and relatively small area that can be exposed in one step.

Stitching errors. To write a pattern, the e-beam machines scans the focused electron beam over the sample by deflecting the beam with electromagnetic coils. At large deflection angles the deflection accuracy decreases due to unavoidable electric current noise in electromagnetic coils and finite addressing accuracy of digital-to-analog converters that translate digital design to analog deflection signals. Therefore, precise exposure of small features over large writing field is impossible and the pattern is broken into so-called main writing fields; their dimensions depend on the required resolution and vary from several tenths of micrometers for the smallest to several hundreds of micrometers for the largest features. Larger areas are then written by combining the deflection with a mechanical movement of the sample stage to create a patchwork of single exposure fields. The mechanical shift has a limited accuracy, which is as large as 20 nm in the best e-beam systems, resulting in *stitching errors* easily visible in scanning electron microscopy (SEM) images. As shown in Fig. 2.2, such errors act as point defects, inducing important scattering and back reflections due to impedance mismatch at the position of the stitching. The problem of stitching can be reduced by maximizing the main field size, however, it cannot be avoided with the currently available technology.

Subfield corrugation. The pattern within each main writing field is further fractured into elementary shapes as rectangles, trapezoids, arrayed rectangles and arrayed trapezoids. Each of the elementary shape is written sequentially in meander fashion, then the beam steps to another one. The fracturation into such trapezium fields, or subfields, can also have an impact on the written pattern, in particular, if the e-beam exposure dosage is low. The subfield fracturation is then imprinted on the actual pattern in form of a weak, residual grating with (sub)nanometer corrugation, which might not be visible in the SEM, but produces undesired light scattering contributing to the propagation loss.

Fig. 2.3 shows an example of periodic subfield corrugation of a nanowire waveguide that causes scattering along the waveguide core. Periodic nature of the corrugation is demonstrated by measuring the angular spectrum of the scattered light, which exhibits two peaks found at two discrete angles. These peaks correspond to the first and second diffraction order of the waveguide TM-polarized mode diffracted into the air by the corrugation grating. The angular spacing between the two diffraction orders gives the grating
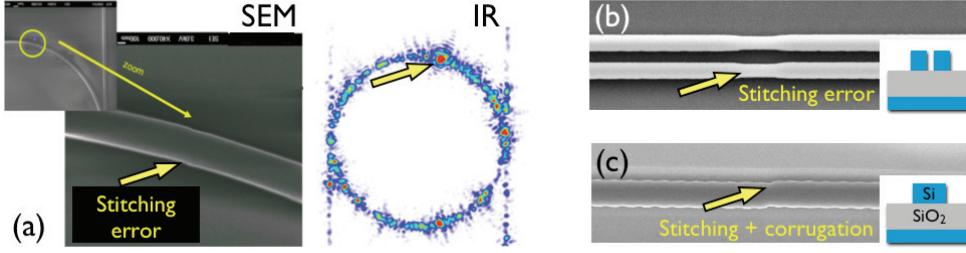
Figure 2.2: Examples of fabrication errors due to main write field stitching. (a) Top-view scanning electron microscopy (SEM) image of a ring resonator with barely visible lateral stitching error. Scattering of the guided mode at the stitching is demonstrated by infrared (IR) near-field imaging. (b) Stitching error observed on a slot wire waveguide. Overlay of the main write fields causes double exposure and consequently the waveguide thinning. (c) Stitching error in combination with waveguide corrugation due to subfield fracturation under low-dose exposure.

period of 1.28 μm, that is exactly the dimension of trapezoidal subfield used in the e-beam writing process. Further, the intensity of the scattered light allows us to roughly estimate the root mean square (rms) roughness of the corrugation to 1 nm, which is not detectable by standard SEM imaging [84].
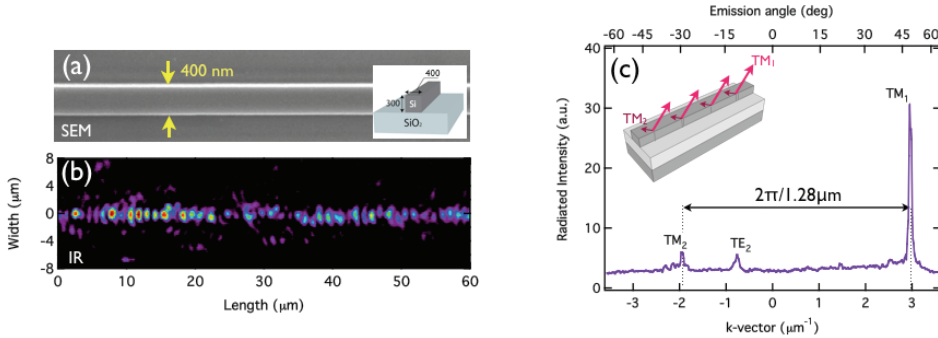
Figure 2.3: (a) SEM and (b) infrared (IR) image of a nanowire waveguide. Although the side-wall corrugation is not visible in the SEM, the near-field IR image shows increased light scattering along the waveguide core. Angularly resolved spectrum of the scattered light exhibits discrete diffraction peaks, thus confirming the periodic nature of the corrugation.

The scattering induced by subfield corrugation will be detailed in Chapter 3 and 4. If the e-beam dose is too low, the effect of the corrugation can be drastic, as illustrated in Fig. 2.2(c). On the other hand, the proper setting of the e-beam dose can (almost) completely eliminate this problem.

Proximity effects. Another issue distorting the original pattern is related to backward scattering of electrons as well as to production of secondary electrons in the photoresist and the device layer. Back scattered electrons lead to secondary exposure of the resist that can be classified as follows [85]:

- *Inter-proximity effects.* If two features are closely spaced, the electrons exposing one shape contribute to the dose of the neighbouring pattern; the boundary of both features gets overexposed and their size enlarged.

- *Intra-proximity effects.* the dose in the centre of the pattern is larger than at the edges and the corners, hence, the corners are underexposed and the sharp edges are rounded.

The proximity effects are more pronounced for low electron acceleration voltage, since the back-scattering occurs in the proximity of the photoresist. The higher the energy of the incoming electrons, the deeper they penetrate into the device and substrate layers, and the contribution to the resist exposure is reduced. Fig. 2.4 shows that going from 10 kV to 20 kV increases the penetration depth of the electrons from 1 μm to around 6 μm [85]. At 100 kV the penetration depth in silicon is around 100 μm.
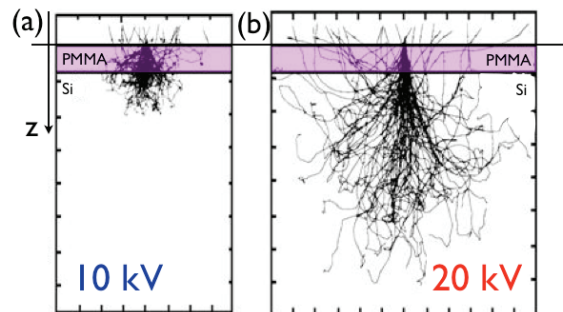
Figure 2.4: Electrons back-scattered towards the photoresist contribute to the exposure, causing the proximity errors. Increasing the acceleration voltage from 10 kV to 20 kV already largely reduces the amount of scattered electrons that can reach back the resist layer [85].

There are two solutions to reduce the impact of the proximity effects: either to use high enough acceleration voltage (100 kV) or to apply proximity error correction tools, such as the e-beam dose modulation. The latter require extensive calculations to determine the proper dose for each individual part of the pattern.

2.2   Dry etching

After lithographic patterning of the photonic devices, the pattern has to be transferred from the photosensitive resist to a high-index device layer, *i.e.* silicon, by highly anisotropic etching. There are a few requirements that have to be fulfilled to fabricate working, high quality devices:

The pattern transfer must yield vertical holes and trenches with high aspect ratio and low surface roughness. Non-vertical side-walls break the symmetry of the device, which leads to TE/TM polarization mixing [43] and to excessive out-of-plane radiation loss [35]. On the other hand, low surface roughness of vertical side-walls is required to reduce the scattering loss.

The etching process must be highly selective in respect to the photomask used. In other words, the photoresist layer must resist the etching process until the device layer is etched through. For SOI devices, 200 nm thick layer of ZEP-520 resist can sustain etching of 200 to 300 nm thick silicon layer typically used to fabricate singlemode waveguides. It is very important to etch through the whole device layer down to the buried oxide, especially if the sample is to be membraned. Unopened holes in photonic crystal devices make it impossible for wet etch to penetrate to the buried oxide layer and the whole membraning process fails, which is shown in Fig. 2.5(a).

Figure 2.5: (a) Holes not etched down to the buried oxide layer prevent formation of homogeneously etched membrane. Oxide residues visible in the central part of the image induc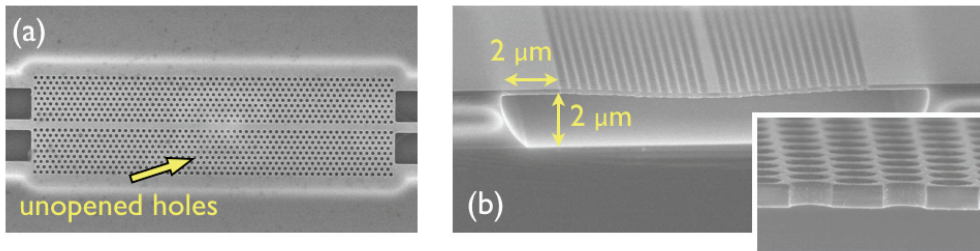e strong scattering of the propagating mode, which has a drastic effect on the device performance. (b) Example of a good quality membrane, where the buried silicon oxide was completely etched away. Isotropic nature of the wet etching process is visible from the comparison of the lateral underetch (visible in the top-view SEM images) and the thickness of buried oxide layer.

The above condition can be fulfilled by highly anisotropic dry etching techniques such as reactive ion etching (RIE), which is a combination of chemical an physical etching (sputtering) in chemically reactive plasma. The plasma is generated under low pressure (vacuum) by an electromagnetic field. High-energy ions from the plasma are accelerated towards the sample surface, attack the surface and react with it.

An example of a Deep-RIE technique that can yield nearly vertical sidewalls with high aspect ratio up to 50:1 is called the Bosch process, also known as pulsed or time-multiplexed etching [86]. The process alternates repeatedly between two modes:

1. A standard, nearly isotropic plasma etch. In case of silicon, the plasma contains sulfur hexafluoride SF_6 ions, which attack the wafer from a nearly vertical direction.

2. Deposition of a chemically inert passivation layer. For instance, C_4F_8 source gas yields a substance similar to Teflon.

Each phase lasts for several fractions of seconds. The passivation layer protects the entire substrate from further chemical etching. However, during the etching phase, the directional ions bombard the the passivation layer at the bottom and they sputter it off, exposing the bottom to the chemical etchant. The side wall passivation layer remains intact, which results in highly directional etching.

These etch/deposit steps are repeated many times over resulting in a large number of very small isotropic etch steps taking place only at the bottom of the etched pits. The two-phase process causes the sidewalls to undulate. The cycle time can be adjusted: short cycles yield smoother walls, while long cycles yield a higher etch rate.

2.3 Buried oxide removal

Removing the bottom cladding layer creates vertically symmetric structures where no polarization mixing occurs, and moreover, it results in an increase of the vertical index contrast. The latter increases the optical field confinement and reduces propagation loss due to radiative or evanescent leakage into the substrate.

The buried oxide is typically removed by isotropic wet etching; in SOI devices, the process involves the use of buffered hydrofluoric acid (BHF) to selectively remove the silica cladding with the etching rate of about 70 nm/min. Free-standing silicon membrane is formed as shown in Fig. 2.5(b).

Care needs to be taken to protect the sample facets as well as long nanowire devices that would, unlike the photonic crystal membranes, collapse without the buried oxide cladding or properly designed lateral support. Fig. 2.6 shows an SEM image of an access nanowire waveguide supported by thin lateral tethers, which represents one solution to fabricate free-standing nanowire devices [87]. The supporting tethers should be extremely thin (down to 60 nm if spaced by 20 μm) to not to substantially disturb the propagating mode. Note, however, that periodic tethers act as one-dimensional Bragg grating that creates photonic mini-stop bands in the waveguide transmission spectra as well as intramodal coupling as discussed in [88]. Therefore, aperiodic spacing between the tethers is preferred to avoid spectral dips in transmission, which are observed *e.g.* in Fig. 2.6 (c) reproduced from [87].
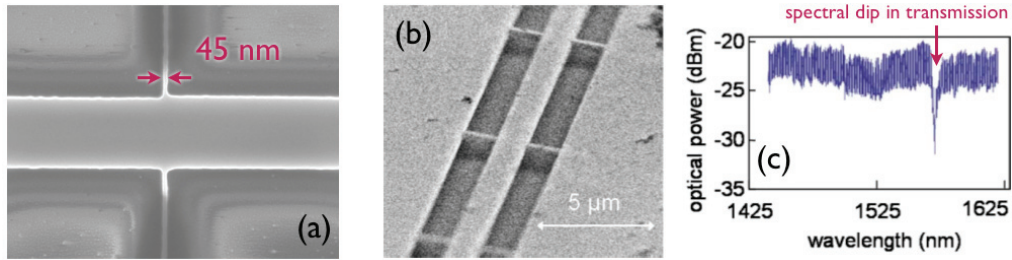
Figure 2.6: (a,b) SEM image of nanowires suspended by 45-nm thin lateral supporting pads. (c) Transmission showing that the supporting pads don't influence the transmission spectrum except from a narrow region; the observed dip in transmission can be attributed to coupling between first and third order TE modes mediated by the periodic perturbation of the waveguide. Figures (b) and (c) have been taken from [87]

2.3.1 Nanophotonic fabrication at EPFL

Technological facilities at Centre of Micronanotechnology (CMI), EPFL, allow for fabrication of high quality silicon-based nanophotonic structures including photonic crystals devices. The fabrication process for SOI and silicon membrane photonic crystals at EPFL was developed and optimized by Hua Zhang, and its detailed description is given in [89]. This section will briefly summarize the main points of the process flow.

Substrates. Silicon-on-Insulator wafers were obtained from SOITEC S.A. Grenoble, France. Wafers of 200 mm in diameter consist of 700 μm silicon substrate and 220 μm

silicon device layer separated by 2 μm-thick silica buried oxide layer.

The most critical parameter is the thickness of the device layer; even small variations in the dimensions of nanostructures can induce an important shift in the dispersion, which can strongly affect the device performance. For instance, the thickness variation of 5 nm causes the W1 mode cutoff to shift by 8 nm. Such a shift is critical in the slow light regime, where the full exploitable operation bandwidth is not larger than 10 nm. The device layer thickness and its tolerance given by the manufacturer is 220 ± 3 nm, however, measurements by spectroscopic ellipsometry [89] give the average value of 222 nm with total variation of 9 nm. The strongest deviation from the average values occurs in concentric rings at the borders and the center of the wafer. By excluding these areas for real sample processing, the expected thickness variation can be reduced to the specified ± 3 nm.

Prior to patterning, the SOI wafer is diced into rectangles of 10×14 mm^2 and the substrate is polished down to 270 μm. Thinning the substrate helps to improve the accuracy of cleaving the processed samples into the final dimensions of 4×14 mm^2, providing for straight and smooth sample facets.

Resists.   There are two positive photoresists sensitive both to e-beam and UV radiation used in the fabrication process:

- ZEP-520A resist is used as a dry etch mask for silicon due to high resolution and sensitivity to e-beam lithography as well as high selectivity to ICP etching. After standard sample cleaning, 200 nm thick layer of the resist is spin-coated on the sample surface and baked at 180° for 3 minutes. Such a thickness is sufficient to etch down through the 220 nm silicon device layer.
- AZ5214 image-reversible photoresist is employed as a wet-etch mask and it is patterned by standard lithography.
- PMMA resist was employed to define surface probe gratings as discussed in Chapter 3. 300-nm thick layer spin-coated on the sample surface is patterned by standard lithography.

E-beam lithography.   Vistec EBPG5000 electron beam lithography machine housed in the class 100 clean room facilities of CMI centre has the following key features:

- 20 to 100 keV acceleration voltage. Such high voltage eliminates the necessity of proximity error correction.
- 1.25 nm minimum pixel size, which makes it possible to write and expose features smaller than 10 nm.
- 20 nm mean stitching and overlay accuracy. Different layers specified in the mask design file that are to be written with different resolutions can be overlaid with an accuracy of 20 nm, which is equal to the accuracy of the main writing field stitching.

Dry etching   The technology uses Inductively Coupled Plasma (ICP) AMS-200 machine to create the plasma by radio-frequency electromagnetic field (13.56MHz, power 1.5 W, chamber pressure 3×10^{-2} mBar). Optimized Bosch process with SF_6 dissociation and C_4F_8 passivation at a balanced ratio 26/63 sccm yields smooth, vertical sidewalls.

Wet etching   After dry etching, the sample is spin-coated with 1.4 μm film of image-reversible photoresist AZ5214, and standard lithography is used to delimit the surface areas

to be membraned. Etching for 30 minutes in BHF results in completely opened membrane as shown in Fig. 2.5(b). Finally, supercritical drying in hot isopropanol vapor follows in order to release any strain in the membrane caused by water surface tension.

2.3.2 Nanophotonic fabrication at the University of St Andrews

The platform uses silicon-on-insulator (SOI) wafer from SOITEC consisting of a 220 nm thick silicon layer separated by a 2000 nm thick silica layer from the silicon carrier. The periodic patterns are defined in ZEP-520A electron beam resist using a hybrid RAITH Elphy Plus/LEO Gemini 1530 electron beam writer with 2 nm placement accuracy. The system uses proximity correction by dose modulation. The pattern transfer into the device layer is performed using a high performance home built reactive ion etching system with a 1:1 blend of SF_6 and CHF_3 gases, a DC bias of 200 V and relatively low power (20 W). The silica cladding beneath the devices is selectively removed with hydrofluoric acid.

2.3.3 Nanophotonic fabrication at IMEC

The Interuniversitary Micro-electronic Centre, IMEC, is a partner organization of the ePIXfab platform (`www.epixfab.eu`), which realizes wafer-scale fabrication of silicon photonic integrated circuits's for research and prototyping. The IMEC's key process is oriented on fabrication of passive photonic functions of 200 mm silicon-on-insulator wafers with 220-nm thick device layer and 2-μm buried oxide layer, *i.e.* the same wafers as used at EPFL and the University of St. Andrews. The nanophotonic devices are patterned by 193 nm deep UV lithography, which is capable of achieving a minimal line width of 120 nm with the minimum pitch of 300 nm. Besides patterning, the process modules available at IMEC include: cleaning, dry etching down to 70, 160 or 220 nm, top oxide cladding deposition (without planarizing), substrate thinning and wafer dicing.

2.3.4 Nanophotonic fabrication at AMO

AMO, Gesellschaft für Angewandte Mikro- und Optoelektronik (`www.amo.de`), offers a versatile and flexible technology platform for research, development and small-scale production of silicon nanophotonic devices and circuits. AMO's Technology is optimized for 220 nm/3000 nm and 340 nm/2000 nm (SOI/BOX) SOI wafers of dimensions up to 6". Other substrate types are possible on request. Patterning is performed by high resolution E-beam Leica (Vistec) EBPG 5000 lithography for ultrasmall features below 50 nm with proximity correction and automated CD-SEM for accuracy check. Modules available at AMO include processes for waveguides and passive devices (strip, rib, slotted and combined technology waveguides fabrication, processes for ring resonators, splitters, couplers and photonic crystals) active devices with n+ and p+ doping and metal interconnects, integrated microheaters and finally processes for or patterned top cladding, membrane etching, metal integration etc.

2.3.5 Nanofabrication at LPN

Laboratoire de Photonique et de Nanostructures (LPN, `www.lpn.cnrs.fr`) focuses mainly on the InP material system. The wafers used comprise typically 260 nm to 310 nm the thick InP device layer on top of 1.5 μm InGaAs sacrificial layer, which separates the devices from 500 μm thick InP substrate. PMMA resist on top of 250-nm thick SiO2 hard mask is

patterned by e-beam lithography using the Leica EBPG 5000+ machine with 2.5 nm beam step size, stitching and overlay accuracy better than 30 nm. ICP etching is performed using Sentech SI500 system with Cl_2/N_2 plasma with addition of BCl_3.

Chapter 3

Experimental characterization, Fourier-space imaging

Despite advanced simulation tools and precise fabrication techniques, optical properties of fabricated devices often differ from the designed ones. The discrepancy might stem from the technology, as nanometer and subnanometer precision is difficult to be achieved even with the state-of-the art fabrication methods, as well as from simulations that are to a certain extent approximative. For example, approximations that are often made in expansion methods as PWE or GME include truncation of the expansion matrices, neglect of the material dispersion and residual disorder, approximation of 3D devices by 2D models and disregard of the absorption induced or out-of-plane radiation losses. In this context, accurate, simple and noninvasive experimental characterization techniques are highly desired. The most common are briefly introduced in the first part of this Chapter, while an overview of their principles and characteristics is given in Table 3.1.

3.1 Overview of experimental characterization techniques

Complete optical characterization of nanophotonic structures typically requires the measurement of two quantities: spectral transmission and the dispersion diagram.

The transmission measurement provides us with quantitative information about the amplitude of light transmitted through the device. It allows us to retrieve information *e.g.* about the bandgap position, wavelength dependent absorption and the propagation loss. Equally, it makes it possible to find the resonance frequencies of localized (cavity) modes and quantify their quality factors.

On the other hand, dispersion measurement gives information about the phase of propagating light, *i.e.* the phase velocity, group velocity and higher order dispersion. It allows us to identify the supported modes, both propagative and evanescent, as well as the mechanism of their mutual coupling. Knowledge of either phase or group index dispersion is essential especially in ultra-fast optics and non-linear optical applications, where the evolution of pulse envelope upon propagation is of primary importance. Equally, understanding and molding the dispersion is of high interest in photonic crystal devices, which often exhibit complex dispersion characteristics.

The methods to measure these two quantities can be roughly divided into the end-fire based methods, where the optical signal is launched into the input port of the waveguide
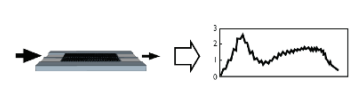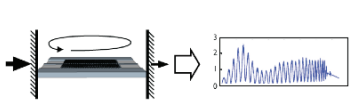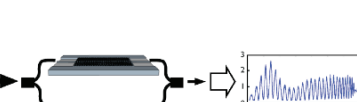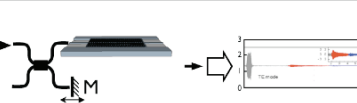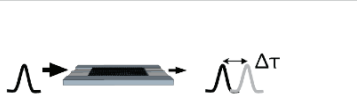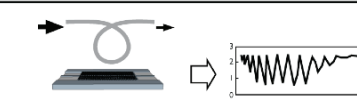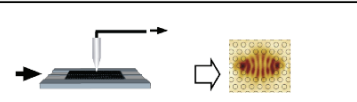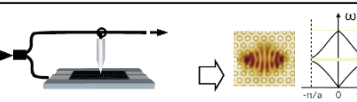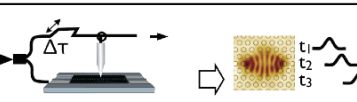
Method	Schema	Output	Comments
End-Fire		Transmission Q-factors	- Black-box method
Fabry-Perot Fringe Analysis		Transmission Group index	- Poor resolution
Spectral Interferometry		Transmission Group index	+ Improved resolution
Optical Low Coherence Interferometry		Reflectance maps Localized states Group index	+ Local information
Time-Of-Flight		Transmission Group index	+ Direct measurement
Far-Field Imaging		Dispersion Q-factors Loss	+ Local + Non-invasive - Additional probes for guided modes
Angle resolved Interferometry		Dispersion	+ Local probe - Complex - Localized and slow modes undistinguishable
Loop Fibre Method		Group index Loss	+ Local - Short devices only
SNOM		Near-Field	+ Extremely Powerful - Complex - Time consuming
Homodyne SNOM		Near-Field Dispersion	+ Amplitude and phase - Complex
Time-Resolved SNOM		Near-Field Time evolution	- Pulse tracking - Localized and slow modes undistinguishable - Complex

Table 3.1: Overview of experimental measurement techniques

and the transmitted or reflected signals are recorded, and the surface-probe methods, which examine the signal reflected or emitted by the sample surface.

3.1.1 End-fire based methods

A schematic layout of a basic end-fire setup is shown in Fig. 3.1. Light from a monochromatic tuneable (or broadband) source is injected through the sample facet into the input port of a nanophotonic device, either using a lensed/tapered optical fiber or microscope objective. Since the size of the focal spot at the sample facet is about 3 μm in diameter, *i.e.* about 10 times larger than the mode profile of a high index contrast waveguide, tapered access waveguides must be designed to reduce the coupling losses. They act as mode profile converters and at the same time they spatially separate the device from the in-coupling region where a lot of spurious scattering occurs. Tapering sections may be used also between access waveguides and the functional devices, *e.g.* to improve the coupling efficiency into slow light modes as reported in [90]. Analogical access waveguide design is used at the sample output to out-couple the transmitted signal, which is then detected by a detection unit such as a photodiode or a spectral analyser. Polarization controllers might be used at both the input and output to select or filter out the desired light polarization.

As an example, Fig. 3.1(b) shows a typical transmission spectrum of a W1 waveguide. It allows us to identify the transmission bandwidth of the waveguide delimited at lower frequencies by the W1 mode cutoff and at higher frequencies by increasing out-of plane radiation loss. Note, however, that it is impossible to determine the exact frequency at which the W1 mode crosses the light line, as well as is it is difficult to tell if the transmission drops strictly at the mode cutoff or above. The latter case occurs very often due to an onset of the slow light regime, in which the light transmission is hindered by enhanced light scattering, localization, or by inefficient coupling into the slow light modes. Simple end-fire measurement does not allow to identify and distinguish these phenomena, it is a "black-box" method that provides only a limited understanding about the character of light propagation within the nanophotonic structures. Therefore, if a conflict between the theory and experiment is found, more advanced techniques are utilized to find the underlying cause for the discrepancy.

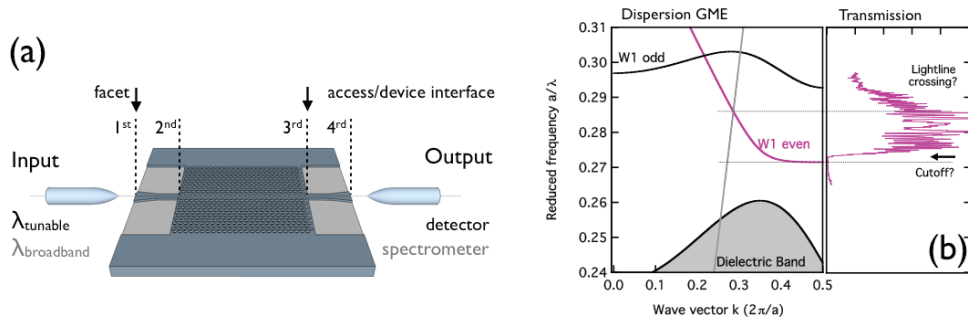**Figure 3.1:** (a) End-fire measurement configuration showing a typical sample layout. The tapered access waveguide section facilitates the light coupling into the nanophotonic structure. (b) Dispersion diagram calculated by the Guided Mode Expansion method (GME) compared to the measured transmission spectrum. The transmission suffers from strong Fabry-Perot interference due to reflections at the sample facets.

Fabry-Perot resonances.

As also visible in Fig. 3.1(b), the experimental transmission spectrum is modulated by interference fringes, *i.e.* the Fabry-Perot resonances, that arise from spurious reflections at the sample facets, stitching errors or structural defects. Reflections may occur also at interfaces between dissimilar structures such as access waveguides and photonic crystal devices. In the simplest case of a straight waveguide with cleaved facets, the Fabry-Perot modulation takes the following form:

$$T(\lambda) = \frac{(1-R)^2 \, \mathrm{e}^{-\alpha L}}{1 + R^2 \, \mathrm{e}^{-2\alpha L} - 2R \, \mathrm{e}^{-\alpha L} \cos(4\pi n_g/\lambda)} \tag{3.1}$$

where L is the waveguide length, R the reflection coefficient at the facet, α the waveguide loss coefficient and n_g the group index of the waveguide mode. For 1-mm long silicon waveguide with typical reflection of $R = 22\%$, propagation loss 2 dB/cm and group index $n_g = 4.5$, the modulation depth reaches as much as 60% of the signal amplitude.

Generally, Fabry-Perot resonances are detrimental to the signal propagation, since the pulse bandwidth is not fully transmitted due to dips in the transmission spectrum. This leads to an overal decrease in transmission, as well as to pulse broadening and echoes. To remove the spurious resonances, several methods have been proposed. The most straightforward solution is to deposit an antireflection coating on the cleaved facet. The optimal refractive index and thickness of the coating layer for normal incidence can be calculated as $n_c = \sqrt{n_{eff}}$ and $\lambda/(4n_c)$, respectively, with n_{eff} the effective index of the waveguide [91]. In the case of a 220 nm thick silicon access waveguide operating around 1.55 μm, the optimal coating index should be $n_c = 1.68$ and the layer thickness $d = 230$ nm. The Fabry-Perot resonances can be also reduced by modifying the sample facet as in [28], where the use of inverse nanotip taper allows for suppression of the residual reflectivity to as little as 1.3%, or as in [15], where the subwavelength grating couplers were employed.

Group index measurement

Fabry-Perot fringe analysis. For the purpose of experimental characterization, however, Fabry-Perot fringes can be also beneficial as they make possible to deduce phase information about the propagating light. Note, that the Fabry-Perot oscillation period is not constant, but becomes smaller when approaching the W1 cutoff, suggesting a strongly dispersive character. The wavelength spacing between two subsequent Fabry-Perot oscillations is actually inversely proportional to the group index $\Delta\lambda \approx \lambda^2/2n_g L$, and therefore the spectral dependence of the group index can be reconstructed from the oscillation spacing measured as a function of frequency. This approach was adopted *e.g.* in the original work of M. Notomi *et.al.* [92], where the group index larger than 100 was reported for a standard W1 waveguide.

Spectral interferometry. In practice, the spacing between Fabry-Perot oscillations might not be easily resolved due to multiple reflections at sample defects, as well as due to limited spectral resolution of the detection unit. To overcome this difficulty, several modifications of the method based on Mach-Zehnder configuration were proposed. The investigated structure is placed in one arm of the interferometer, while the second arm contains a reference waveguide of known dispersion [93], or is formed by a free path with
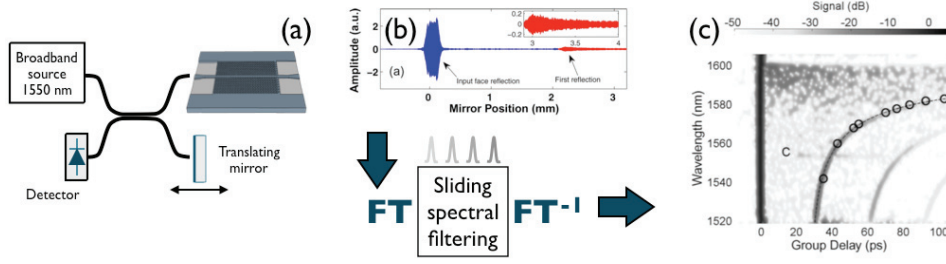
Figure 3.2: (a) Experimental setup for Optical Low-Coherence Reflectometry (OLCR); intensity of the reflected light is measured as a function of the position of the translating mirror, which yields the interferogram shown in (b). The reconstructed reflectance map od a photonic crystal W1 waveguide coupled to a point defect cavity.

an adjustable length [94]). The interpretation of the interference spectrum is similar as for the Fabry-Perot analysis, however, an external interferometer allows to enhance the fringe visibility to override spurious resonances, and to adjust the absolute spacing between the interference maxima in order to increase the maximal resolvable group index while keeping the same spectral resolution.

Optical low-coherence reflectometry   Optical low-coherence reflectometry (OLCR) [95,96] allows to reconstruct the dispersion properties by analysing the signal back-reflected at the sample facets.

The setup is based on a Michelson interferometer excited by a broadband source, in which the investigated device is in one arm and a translating mirror in the other one as shown in Fig. 3.2(a). Interference between the signal reflected from the sample and the mirror is scanned as a function of the mirror position, yielding an interferogram as in Fig. 3.2(b). Further numerical processing of the interference data, *i.e.* Fourier transform followed by spectral filtering and back Fourier transform, makes it possible to reconstruct so-called reflectance maps of the device. Such reflectance maps show the pulse delay within the investigated structure as a function of the wavelength, which gives directly the information about the group index of the propagating mode(s). In addition, the method allows to identify scattering at the sample defects as well as enhanced back-scattering due to slow light regime as detailed in [95].

In contrast to other transmission-based techniques detailed bove, the OLCR is not fully a "black box" method as it allows to track the back-scattering along the waveguide, providing not only spectral, but also spatial information about the propagating light. However, the method can be used to retrieve only the group index and the higher order dispersion, while the phase index remains unknown.

Time-of-flight methods.   Probably the most straightforward way of measuring the group index in transmission configuration relies on the use of the time-of-flight methods. They measure the phase delay of optical pulses with relatively narrow bandwidth of the order of 1 nm and less, transmitted through the structure under study. The phase delay of the pulse envelope is directly related to the group index, as demonstrated *e.g.* in [97] and references therein. Time-of-flight measurement compared to the result of Fabry-Perot fringe analysis is presented *e.g.* in [98].

3.1.2   Surface probe methods

The methods rely on observation of resonant patterns in emission or reflectance spectra, which typically allows to retrieve the dispersion band diagram of 1D or 2D photonic crystals or angular emission distribution of localized modes including their quality factors. As can be seen in Tab. 3.1, several configurations in respect of light in- and out-coupling can be employed:

Far-field imaging.   The excitation light is butt-coupled into the structures as in end-fire configuration and the angular distribution of the radiative (leaky) modes as well as their dispersion is observed in the far-field. An example is the Fourier-Space imaging method developed at EPFL, which will be discussed in detail in the second part of this chapter.

Angle-resolved reflectometry.   The sample is excited directly from the sample surface and reflection from (resp. transmission through) the device layer is recorded. When the energy and the wavevector of the excitation matches those of the allowed modes, part of the incoming light is coupled into the modes and dips are observed in the measured reflection (resp. transmission) spectrum [99, 100].

However, only radiative modes that light above the light line can be excited by this technique, and hence, the technique as such cannot be used to probe the dispersion of truly guided modes. This limitation can be overcame by means of **angle-resolved attenuated total reflectance** method (ATR) reported by M. Galli et al. [100]. By placing a high-index hemisphere (*e.g.* ZnSe) at a small distance from the surface of the sample, coupling between the evanescent fields of the guided modes and light at the air-prism interface occurs, therefore allowing for excitation of modes lying below the light line.

The main difficulty with this method is the hemisphere alignment: perfectly flat hemisphere and a nanometer precision of the distance between the hemisphere and the sample surface is necessary to efficiently couple into the supported modes of the structure and at the same time to not to disturb its dispersion properties. The optimal distance is only ~ 250 nm [100]. Furthermore, the method cannot resolve between truly guided modes and localized states; once the light is coupled into a resonance state of the structures, it is not possible to check only from reflection if the mode further propagates or remains localized due to *e.g.* disorder and enhanced scattering in the slow light regime. Finally, the maximum k-vector to be probed is strictly limited by the refractive index of the hemisphere.

Loop fiber method.   Highly curved tapered fiber with the radius of curvature of approximately 25 μm can be also used to excite the sample within a wide range of wavevectors both above and below the light cone. M. Lee et al. [101] used this approach to probe the group index of short waveguides terminated by photonic crystal mirrors, by recording the transmission spectrum of the looped fiber. Fabry-Perot resonances observed in the spectrum allowed to reconstruct the group index and its dispersion in a similar way as described above for the end-fire based methods. Note, that this approach does not yield the absolute phase index of the guided modes.

Near-field probes

One quantity that cannot be retrieved neither from transmission, nor from dispersion measurement is the near-field distribution of electromagnetic field inside the nanophotonic
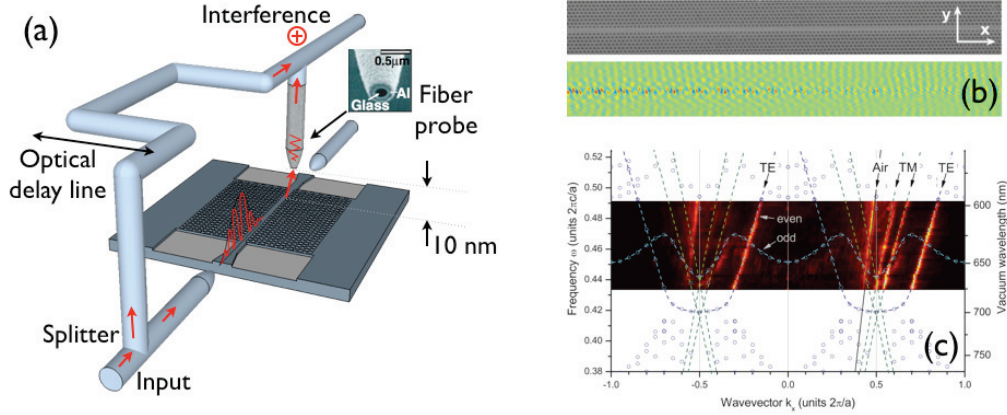
Figure 3.3: (a) Schematic drawing of a heterodyne SNOM setup, which allows for retrieval of both the amplitude and phase of the electromagnetic field. (b) Optical field measured along a W1 photonic crystal waveguide. (c) Dispersion diagram of the propagating TE and TM modes reconstructed by numeric Fourier Transform of the electromagnetic field shown in (b). [102].

structures. Such a near-field pattern is not accessible by far-field imaging techniques, since the subnanometer variations of the electromagnetic field typical for nanophotonic structures cannot be resolved by simple imaging because of the diffraction limit. Scanning near-field optical microscopy (SNOM) is currently the only technique capable of providing reliable data of the experimental near-field distribution (Fig. 3.3).

SNOM. Traditional SNOM techniques use a tapered optical fiber, often metal coated, to disturb the evanescent field just above the sample surface. The scattered light can be collected either directly by the optical scanning fiber [103], using far-field detection unit [104] or in a transmission configuration as in [105]. In the latter case, the scattered and absorbed light manifests itself as a drop in measured transmission signal. By raster scanning the probe over the sample, the near-field distribution is measured (optionally, at the same time as the topography of the sample). Typically, resolutions attainable with this technique are ∼50 nm and better.

When two orthogonal polarizations are present in the excitation signal, one can select either one or the other by setting the polarization of the reference arm, and hence, make the setup sensitive to the polarization state of the near field. For instance, E_x and E_y field components can be retrieved separately, and polarization properties of the investigated mode can be reconstructed. This approach was adopted by [106] to observe polarisation singularities in photonic crystal W1 waveguides. Nevertheless, special SNOM probe has to be chosen for this experiment to guarantee conservation of polarization within the SNOM tip.

Homodyne (Phase-sensitive) SNOM. An alternative to the conventional SNOM is the heterodyne SNOM [107], in which the collected signal is interferometrically mixed with the reference signal split from the same laser source. In the measurement, the length of the reference branch is kept constant while the length of the signal branch changes due to

the raster scan along the sample. As a result, interference fringes are observed that allow to reconstruct the phase evolution along the propagation direction.

The wavevector of light can be recovered from the phase image, and when plotted as a function of the excitation wavelength, the full bandstructure diagram can be reconstructed as reported *e.g.* in [103, 108]

Time resolved SNOM.   Heterodyne SNOM yields the complete, *i.e.* both the phase and amplitude spatially-resolved information about the propagating electromagnetic field. In addition, when combined with a tuneable delay line, it can be used to visualize the dynamic effects inside the structure, such as tracking the femtosecond laser pulse propagation in standard [109] or slow light photonic crystal waveguides [103].

3.2   Fourier-space imaging

Fourier-space imaging (FSI) combined with end-fire setup is a technique proposed and successfully applied in our laboratory to retrieve in one step both the dispersion and transmission properties of complex photonic nanostructures. This non-invasive optical technique allows for direct imaging of supported modes, both in real space and in k-space. The technique gives access to the location of the near-field maxima, the dispersion relation, as well as reflection and transmission coeficients of modes found both above and below the light cone.The present section has for objective to give a comprehensive description of the technique and the experimental setup used at EPFL, while the intriguing results we obtained thanks to this tool are discussed in the following chapters of the thesis.

The FSI technique is based on far-field analysis of optical signal, which is either directly radiated from the sample (leaky modes) or diffracted by the use of intentionally designed periodic perturbations (guided modes). Let's first focus on the case of leaky modes that are guided within the plane of the sample but are not fully confined in the vertical direction, i.e. they can radiate out-of-plane.

3.2.1   Far-field imaging

We assume that optical signal of a given frequency ω_0 is butt-coupled into the nanophotonic structure and propagates along the waveguide in the propagation direction z. Since the mode under consideration is radiative, a portion of its intensity can *leak out* of the guiding structures into the far-field. Due to wave-vector conservation at the sample-cladding interface (eq. (1.8)), such radiation occurs only at well-defined angles β that are strictly related to the propagation constants, or the Bloch wave-vectors, k_z, of the supported modes:

$$k_z = k \cos \beta = \frac{2\pi n}{\lambda_0} \cos \beta \qquad (3.2)$$

where λ_0 is the vacuum wavelength and n is the cladding refractive index, equal to 1 for the typical case of air cladding. Hence, measuring the angles under which the mode radiates gives us a direct access to the propagation constant k_z, and vice versa.

To practically probe the emission angles β, or equivalently, the wave-vectors k_z, we use the Fourier transforming property of a thin, aberration-free optical lens; As is illustrated in Fig. 3.4, if an object is placed one focal length in front of the lens, its optical Fourier
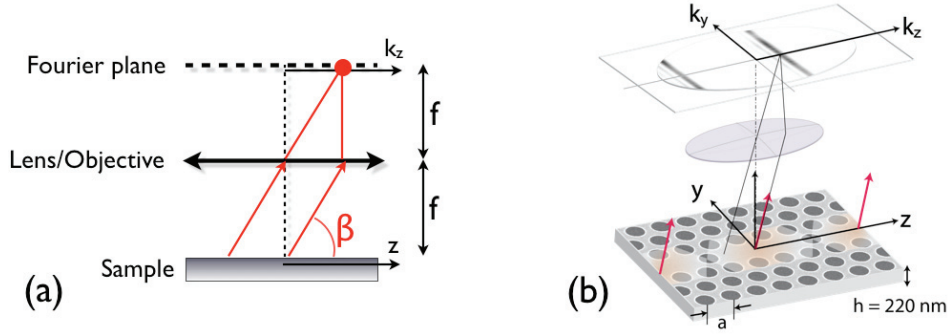
Figure 3.4: (a) Schematic drawing and (b) practical realisation of Fourier-space imaging using the Fourier transforming property of a lens.

transform will be found in the back-focal plane of the lens, where the so-called Fourier-space image is formed. The proof can be found *e.g.* in [110, 111]. In such a Fourier-space image, every point is uniquely related to one angle, or one k-vector of the radiated field, *i.e.* to the quantity we seek to measure.

Far-field profile of a one-dimensional waveguide

Fig. 3.5 shows an example of a Fourier-space, or far-field image recorded for a W1 photonic crystal waveguide, in the wavelength range where it operates above the light line. The pattern is formed by two vertical lines, located at discrete positions k_{z1} and k_{z2} along the propagation direction z, and extended along the perpendicular direction k_y. The shape of the far field pattern can be explained by the fact that the radiation angle along the propagation direction is strictly related to the propagation constant of the guided mode, so only one or several discrete radiation angles are allowed, while there is no restriction on the emission angle in the perpendicular direction. Due to strong spatial confinement along y, the angular spread of the emission is large, it extends well beyond the objective aperture. The intensity profile along k_y appears to be nearly homogeneous, however, weak intensity modulation is still observed due to the specific mode profile and possible interference with light reflected from the substrate layer [112].

Looking closer at the profile along the propagation direction k_z, one can notice that the positions of the lines are symmetric relative to the k-plane origin, *i.e.* $k_{z2} = -k_{z1}$. In fact, the two lines correspond to the forward and backward propagating W1 mode; the latter is present due to spurious reflection at the output facet of the sample. Knowing the length of the sample, the relative intensity of the two peaks measured at different positions along the sample can provide us information about the propagation loss along the waveguide, or give an estimate of the reflectivity at the sample facet.

Furthermore, each of the lines is broadened along k_z due to the propagation loss and the finite size of the structure. Under finite size one should understand either the finite physical length of the waveguide, or finite size of the field of view restricted by the collecting lens or spatial filtering. Assume first that the sample is infinitely long, but suffers from the out-of-plane and scattering loss α that manifest itself as an exponential decay along
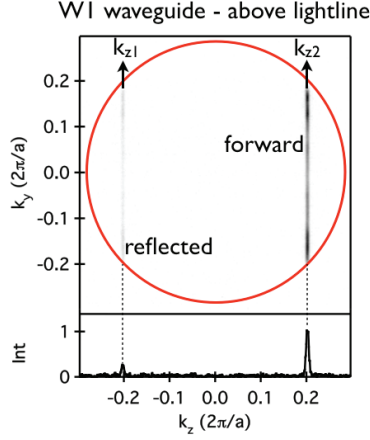
Figure 3.5: Fourier-space image of a W1 waveguide operating above the light line. Bottom: Integrated far-field profile.

the propagation direction:

$$E(x, y, z) = E(x, y)\theta(z)\mathrm{e}^{-\frac{\alpha}{2}z}\mathrm{e}^{-ik_{z_0}z} \tag{3.3}$$

where $\theta(z)$ is the Heaviside step function. In the Fourier space, such exponential decay results in a convolution of the original, infinitely narrow line with the Lorentzian function:

$$\mathcal{E}(k_y, k_z) = \mathcal{E}(k_y)\delta(k_z - k_{z_0}) * \frac{1}{\frac{\alpha}{2} - ik_z} = \mathcal{E}(k_y)\frac{1}{\frac{\alpha}{2} - i(k_z - k_{z_0})} \tag{3.4}$$

$$\mathcal{I}(k_y, k_z) = \mathcal{I}(k_y)\left|\frac{1}{\frac{\alpha}{2} - i(k_z - k_{z_0})}\right|^2 = \mathcal{I}(k_y)\frac{1}{\left(\frac{\alpha}{2}\right)^2 + (k_z - k_{z_0})^2} \tag{3.5}$$

The normalised FWHM linewidth Δk is directly equal to the loss parameter α.

On the other hand, if the sample has a finite size, but the propagation loss is neglected, the real-space field pattern can be expressed as multiplication of the infinite field by a rectangular function:

$$E(y, z) = E(x, y)\mathrm{e}^{-ik_{z_0}z}\,\mathrm{rect}(z/L) \tag{3.6}$$

where L is the length of the sample. The Fourier-space image will be then modulated by a *sinc* function:

$$\mathcal{E}(k_y, k_z) = E(k_y)\delta(k_z - k_{z_0}) * \mathrm{sinc}(\frac{L}{2\pi}k_z) = E(k_y)\,\mathrm{sinc}(\frac{L}{2\pi}(k_z - k_{z_0})) \tag{3.7}$$

$$\mathcal{I}(k_y, k_z) = \mathcal{I}(k_y)\,\mathrm{sinc}^2(\frac{L}{2\pi}(k_z - k_{z_0})) \tag{3.8}$$

The normalised FWHM linewidth Δk is related to the sample lenght L as $\Delta k = 0.886/L$.

In practice, both effects will contribute simultaneously to the linewidth broadening. Nevertheless, if the sample is long enough, the latter contribution can be neglected and the Fourier-space FWHM linewidth can be considered equal to the radiation or scattering induced loss α. This approximation can be used *e.g.* to quantify the decay rate of evanes-

cent modes inside a photonic crystal bandgap directly from the k-space linewidth as was done by N. Le Thomas et al. in [113].

Dispersion measurement

In the example above, the position of the lines k_{z1} and k_{z2} correspond to monochromatic excitation. If the excitation frequency is tuned, the lines move along the k_z axes following the dispersion relation of the W1 waveguide. Hence, measuring the line pozition k_z as a function of the frequency of excitation allows us to reconstruct the full dispersion relation of the supported modes. Typically, the far-field profile is integrated along the vertical k_y direction and plotted versus the excitation frequency, which results in an accurate and smooth dispersion curve as graphically illustrated in Fig. 3.6. Such dispersion curves can be numerically differentiated to yield the group index or higher order dispersion.
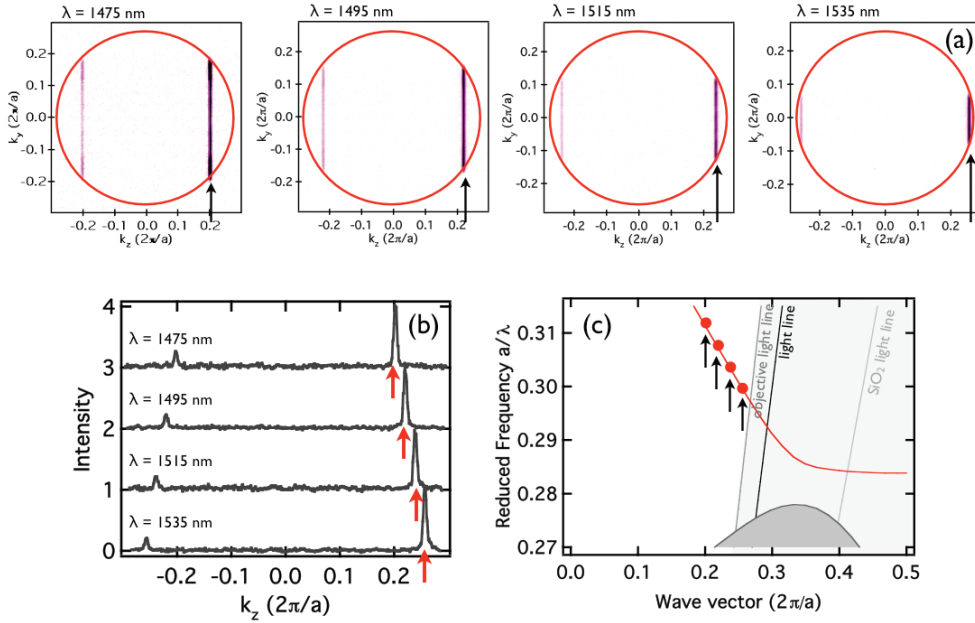
Figure 3.6: Reconstruction of a dispersion curve for a W1 waveguide operating above the light line. (a) Shift of the far-field pattern when the excitation wavelength is scanned between 1475 nm and 1535 nm. (b) Integrated profiles of far-field images in (a) plotted as a function of k_z. (c) Reconstruction of the dispersion curve from the position of peak maxima in (b), the k-vector position for each wavelength is indicated by an arrow.

Far-field profile of a point defect emitter

Another example of the Fourier-space image recorded for a photonic crystal L3 cavity, *i.e.* a cavity formed by omitting three adjacent holes in the Γ-K direction, is shown in Fig. 3.7. Such image gives directly the angular intensity distribution of light emitted from the cavity. The radiation pattern extends continuously over the whole pupil, until reaching the maximal spatial frequency that is limited by the Numerical Aperture (NA)

of the imaging lens. In the present example the NA = 0.9, which corresponds to the full collection angle of 130°.

It can be observed that the L3 cavity is characterized by intensive emission occurring in the vertical direction as well as at high spatial frequencies, while there are angles, *i.e.* $k_z = \pm 0.1252\pi/a$, at which the cavity radiation is almost entirely suppressed.
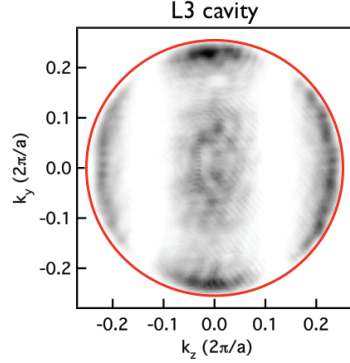
Figure 3.7: Fourier-space image of an L3 cavity.

Knowledge of the experimental far-field emission pattern is crucial for engineering the high-quality factor cavities and low-loss coupled-cavity waveguides as will be discussed in Chapter 7, as well as for applications that deal with enhanced or directive extraction of light [114, 115].

3.2.2 Probing the guided modes

In contrast to leaky modes considered until now, the truly guided modes that are typically of primary interest for practical applications lie below the light cone and do not radiate into the far-field. Their field is well confined within the guiding structure and decays exponentially into the air cladding. In the high index contrast devices, the field intensity drops practically to zero within the first 200-1000 nm away from the waveguide core, and therefore, it cannot be accessed by use of conventional far-field optics.

To be able to probe the dispersion of the guided modes with the FSI technique, we have to artificially introduce a mechanism that enables coupling of a small portion of guided light with the radiative modes. In other words, we need to introduce small perturbations that scatter a part of the guided mode into the far-field. The scattering process should be weak enough not to disturb the original dispersion and at the same time yield light intensity of detectable level. Furthermore, it must be well-controlled in a manner to conserve both the amplitude and phase information about the original field. This can be achieved by periodic one-dimensional probe gratings (PGs) designed in the proximity of the waveguide core that diffract a small amount of the guided mode intensity into the far-field (see Fig. 3.8).

Diffraction at a grating is a coherent process that preserves the phase relation between the guided and the diffracted field. The actual dependence of the wave vector of the diffracted light k_0 on the propagation constant of the guided mode k_{prop} is given by the
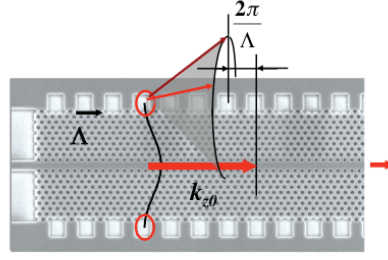
Figure 3.8: Photonic crystal waveguide with rectangular linear probe gratings designed at the boundaries of the photonic crystal region. The light scattered into the light cone obeys the grating equation $k_{z_{diff}} = k_{z_{prop}} + m\frac{2\pi}{\Lambda}$.
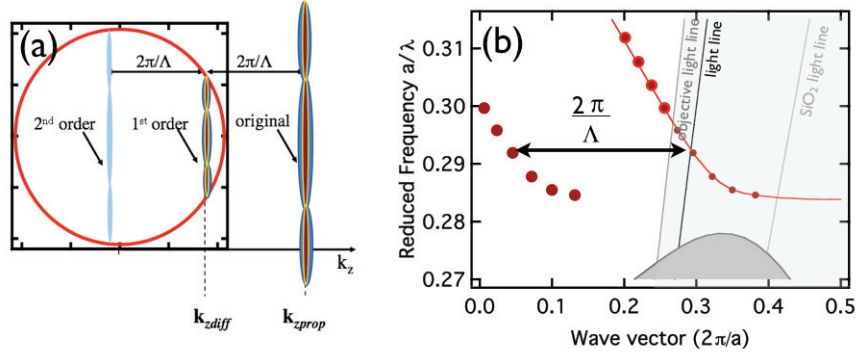
Figure 3.9: Reconstruction of the dispersion relation of the guided modes. (a) Far-field image schematically showing the first and second diffraction order inside the light cone as well as the original Bloch k-vector lying below the light cone, outside the pupil of the collecting lens. (b) Dispersion relation of the guided mode is equal to the dispersion relation of the scattered light, just folded by one (resp. two) reciprocal vector of the probe grating.

grating equation:

$$\mathbf{k}_{diff} = \mathbf{k}_{prop} + \mathbf{G} \tag{3.9}$$

where $\mathbf{G}$ is a reciprocal lattice vector of the probe grating. In the case of a one-dimensional grating designed along the propagation direction z the grating equation simplifies to:

$$k_{z_{diff}} = k_{z_{prop}} + m\frac{2\pi}{\Lambda} \tag{3.10}$$

with Λ the grating period and m an integral number giving the order of diffraction. Hence, the k-vector of the guided mode $k_{z_{prop}}$ can be inferred from the knowledge of $k_{z_{diff}}$ and the grating period Λ. Similarly, the dispersion of the guided mode $\omega(k_{z_{prop}})$ is equal to the dispersion of the diffracted field $\omega(k_{z_{diff}})$, just shifted by m-times the reciprocal vector of the probe grating along k_z as illustrated in Fig. 3.9.

Grating designs

The period of the PGs is chosen such that ideally the first or the first two diffraction orders of the guided mode are folded into the light cone. In the case of photonic crystal structures, it is beneficial to set the period as a multiple of a lattice constant, most often $\Lambda = 3a$ or $\Lambda = 4a$ for one or two diffraction orders in the light cone, respectively. In such a design the diffraction orders from different Brillouin zones would overlap, increasing the signal-to-noise ratio and facilitating the interpretation of the measured pattern. If Λ is not an integer multiple of the lattice constant, different diffraction orders from each individual Bloch mode component appear in the light cone, at different positions and intensities. They are often closely spaced, and the assignment of which feature belongs to which Brillouin zone is complex and might lead to misinterpretations.

The amplitude of the grating, i.e. the amount of light scattered by the grating depends on the following factors: grating distance from the waveguide core, physical size of the form factor of the grating, its refractive index and the grating duty cycle. As shown in Fig. 3.10, several different designs of the PGs were tested. Most of them are etched during the fabrication procedure together with the sample structure, however, we also successfully tested designs with add-on gratings (PMMA PGs) that can be removed one the characterization is finished. The summary of advantages and disadvantages of each individual design is given below:

- *Linear probe grating* designed in the evanescent tail of the guided field. Typically, the grating has a form of rectangular or circular pillars for nanophotonic SOI waveguides, or holes in photonic crystal devices, etched at both sides alongside the guiding structure as shown in Fig. 3.10(a). Interference of light diffracted at the two gratings results in a characteristic modulation of the far-field pattern along the k_y direction, as depicted in Fig. 3.9(a). Such a modulation facilitates the identification of the probe signal, distinguishing it from spurious background noise even for weak signal amplitudes.

   The main advantage of the linear probe grating is that it can be designed arbitrarily far away from the guiding structure, thus not disturbing the guided mode dispersion. As experimentally tested, the nanophotonic wire waveguides on Silicon-on-insulator substrate, the ideal distance between the PGs and the waveguide core is 500-700 nm, and in the case of photonic crystal waveguides, 9-11 rows of holes away from the line defect region. However, the strength of the interaction between the guided mode
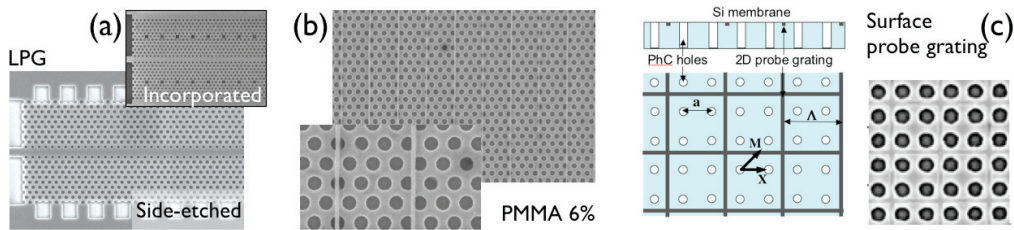

Figure 3.10: Top-view SEM images of severa probe grating designs: (a) Linear probe grating designed alongside and inside the photonic crystal region. (b) PMMA grating with a duty cycle of 6%. (c) Shallow etched, two-dimensional surface probe grating.

and the grating largely depends on the mode profile. If the mode profile changes with frequency, the interaction changes accordingly, which might result in either too strong or too weak interaction at certain frequencies. A good example is the W1 photonic crystal air-bridge waveguide upon transition between the fast light and slow-light regimes. In the slow light regime, the exponential decay of the W1 field in the direction perpendicular to the propagation is faster [77] and the signal scattered at the probe gratings decreases. Thus, while the dispersion curve can be clearly followed in the fast light regime, its signature often disappears in the slow light regime as demonstrated in Fig. 3.11(b).
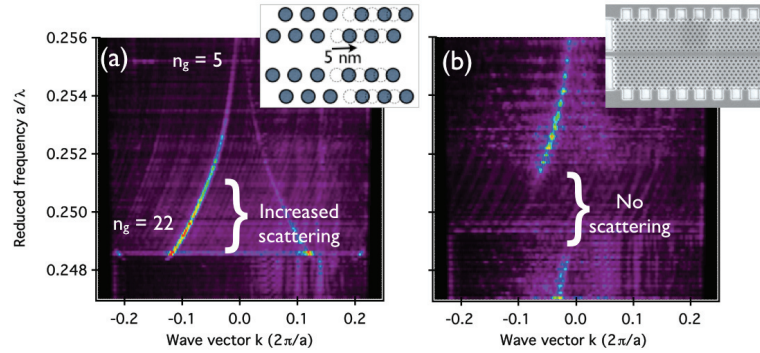
Figure 3.11: Comparison of different grating designs applied to measure the dispersion of a slow-light tailored photonic crystal W1 waveguide designed for a group index of 32 [58]. (a) One-dimensional volume grating allows us to follow the dispersion curve to the proximity of the mode cutoff. In the slow light regine, one can observe an increase in the intensity of the out-of-plane scattering due to slow-light enhanced interaction between the light and the grating. (b) Linear probe grating makes it possible to reconstruct the dispersion on the fast-light regime, however, the scattered signal decreases to zero when the group index increases above ≈ 15. This is attributed to a change of the mode profile of the slow, bandgap-guided mode.

Another drawback of the linear probe gratings in photonic crystal environment is that gratings etched at the boundary between the photonic crystal and the surrounding high index layer can scatter all the spurious light found in that layer, thus increasing the background noise. We tried to solve this issue by designing the linear probe grating *inside* the photonic crystal mirror as shown in Fig. 3.10(a). However, it turns out that such a grating does not only scatter the guided mode, but often supports its proper modes that can couple to the guided modes, which equally increases the noise in the Far-field.

- *One-dimensional volume grating.* This approach induces extremely weak periodic perturbation directly at the waveguide core, so that the optical mode is diffracted at the grating independently of its mode profile. Such a grating can be easily realized in the photonic crystal waveguides by periodically shifting the positions of holes at the waveguide core. If the shift is of the order of 5 nm, it only negligibly alters the mode dispersion and at the same time it creates sufficiently strong probe for the FSI.

Fig. 3.11(a) shows an example of a dispersion curve measured using an one-dimensional volume grating together with the schematic drawing of the grating design; For every

third period of the waveguide, the lattice constant of the photonic crystal along the propagation direction was increased by 5 nm. In this particular case, the grating shouldn't be referred as a *probe grating* as the intentional increase of the lattice constant also slightly shifts the original dispersion curve, however, the neat dispersion curve serves as a proof of principle that the FSI method with properly designed probes can accurately probe the dispersion and be of a great help *e.g.* for dispersion engineering for slow light applications. Moreover, the design can be modified in the future to respect the periodicity of the photonic crystal by *e.g.* by shifting not the whole supercells, but only the position of individual holes within otherwise periodic photonic crystal lattice.

• *PMMA surface grating* is a modification of the volume grating design, however, its great advantage is that it can be introduced just for the characterization purposes and removed once the dispersion curve is measured. It can be fabricated using the following steps: thin, ≈ 300 nm thick layer of PMMA is spin-coated on the sample surface and patterned by standard lithography. The resulting grating shown in Fig. 3.10(b) consists of narrow, 100-nm wide stripes of PMMA sitting on the surface of the photonic crystal structures. For the refractive index of PMMA equal to 1.5 and height of the PMMA layer of 300 nm, the duty cycle of the grating must be lower than 10% to not to critically increase the scattering loss.

As in the previous design of the volume grating, the advantage of the surface PMMA grating is that it probes the entire lateral profile of the guided mode. On the other hand, its fabrication requires an additional technological step and it is difficult to be used on air-bridge structures due to fragility of the membrane and leakage of PMMA through the holes into the bottom cladding region.

• *Shallow-etched surface grating* design was tested on 2-dimensional bulk photonic crystal of square lattice of holes as shown in Fig. 3.10(c). The probe grating composed of 70 nm wide and 20 nm deep etched lines allowed to efficiently probe the extended states of the PhC dielectric band as reported in N. Le Thomas *et.al.* [116].

The 2D probe grating has to be etched very shallow in order to avoid detrimental losses or the creation of a double PhC structure that would imply a strong modiÞcation of the dispersion, which is technologically rather challenging. As in the case of PMMA grating, two technological steps are required, and in addition, this type of grating cannot be removed leaving the original structure intact.

• *Residual periodic disorder.* As already discussed in the Chapter 2, the intrinsic residual periodic errors resulting from the e-beam patterning process are sufficient to create a probe grating. In particular, the trapezoidal write field corrugations that have a periodic character with a period typically about 1 μm can serve as a probe that diffracts a sufficient amount of light to reconstruct the dispersion.

If the precise knowledge of the dispersion curve is not needed and only the value of the group index is sought, the latter can be retrieved from scattering at arbitrary non-periodic scatterers located along the waveguiding structure such as defects, stitching errors and structure interfaces. In the Fourier-space, the light scattered from the defects forms an interference pattern, which is characteristic for the given distribution of scatterers. When tuning the wavelength of excitation, the features of such interference pattern move in

k-space following the dispersion relation as in the case of scattering at periodic probes. Hence, the shape of the dispersion curve can be reconstructed as $k_{z_{prop}} = k_{z_{diff}} + c_z$, while its exact position along the k_z axes given by the constant c_z remains unknown.

Pros and cons of the FSI technique

The FSI technique allows for local imaging of propagating modes, both in real space and in Fourier space. In contrast to the black box methods, it can map the mode properties at each spatial position along the guiding structure and, hence, identify the evolution or changes in the dispersion properties. Due to the local nature of the technique, it can be used even when the structure is integrated on a chip with other optical functions.

The phase and group index dispersion is probed with a high accuracy, fine spectral resolution, and without the need for cumbersome near-field scanning and data post-processing techniques (SNOM) or complex alignment (ATR). It can easily distinguish between dispersive propagating modes and non-dispersive localized states, which is not the case of *e.g.* ATR.

It is fully non-invasive in the case of radiative modes.

For the guided modes, the added grating probes may perturb the original dispersion properties of the structures. Interaction of the optical mode depends on the grating design, but also on the mode profile and the group index. Due to increased light-matter interaction in the slow light regime [117, 118], the originally non-invasive grating can lead to creation of ministopbands at the crossing points of the folded dispersion curves (formation of a double-period photonic crystal structure). Therefore, careful design of the grating probes properly designed and adjusted for each particular structure and application is required.

3.2.3   Experimental setup

Resolution and quality of the Fourier-space image and, hence, the accuracy of the reconstructed dispersion depend to a large extend on the concrete realization of the Fourier-space imaging setup. The experimental setup built in our laboratory is schematically shown in Fig. 3.12 and consists of three principal parts: end-fire path to measure the transmission spectra, infrared path to perform the actual Fourier-space imaging, and the visible path for the alignment purposes.

End-fire path.   We use a standard end-fire setup to excite the structures under study and obtain their transmission spectra. The excitation laser source is a highly monochromatic external cavity laser Nettest Tunics Plus, tuneable within the wavelength range of 1470 nm to 1660 nm. The resolution of the wavelength tuning $\Delta\lambda = 1$ pm and the absolute wavelength accuracy of 5 pm are guaranteed by the manufacturer at the laser power of 1mW. The laser output is linearly polarized in the vertical direction, however, we can control the polarization direction in the excitation path using a $\lambda/2$ plate in combination with a polarizer to excite separately the TE or TM modes. The optical signal is then injected into the sample via a lensed fiber and adiabatically tapered ridge access waveguides. The signal transmitted through the sample is coupled out by means of another lensed fiber and detected using a InGaAs power meter. The lensed fibers purchased from OZ Optics LTD, Canada, are based on SMF 28 fiber which is tapered to provide a ~2.5 μm focal spot at the working distance of approx. 6 μm. The ends are antireflection coated for 1550 nm.
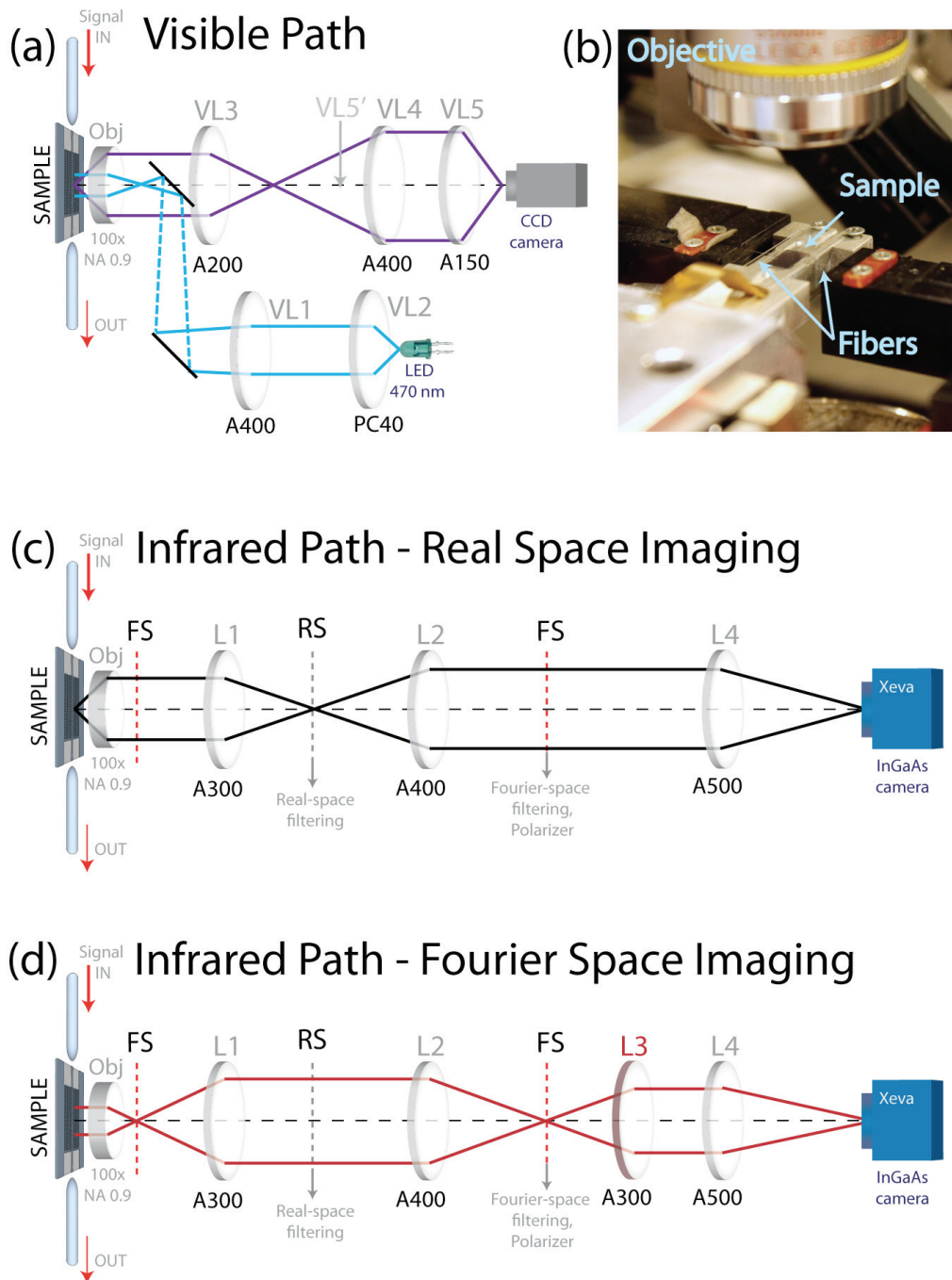
Figure 3.12: Fourier-space imaging setup. (a) Visible path for alignment purposes. (b) Photography image of the sample installed below the collecting microscope objective and coupled in end-fire configuration. (c), (d) Infrared path used for real-space and Fourier-space imaging, respectively. Switching between the two is accomplished by removing the L_3 lens.

Prior to detection, second polarizer is used to filter out a part of the unpolarized spurious background noise, thus increasing the signal-to-noise ratio.

Visible path. The visualization of the sample surface is indispensable for the alignment of the end-fire path, *i.e.*, for adjusting the position between the lensed fibers and the integrated access waveguides to allow for light in/out-coupling. Nevertheless, it also allows for a quick visual check of the sample surface that can disclose possible imperfections in the sample quality. Beside obvious damage such as broken structures and large sample defects, visible imaging allows us to detect with a spectacular contrast the stitching errors, fine changes in the filling factor and/or lattice constant of photonic crystal devices, as well as variations in the homogeneity of the bottom cladding removal in case of the air-bridge structures (see Fig. 3.13).
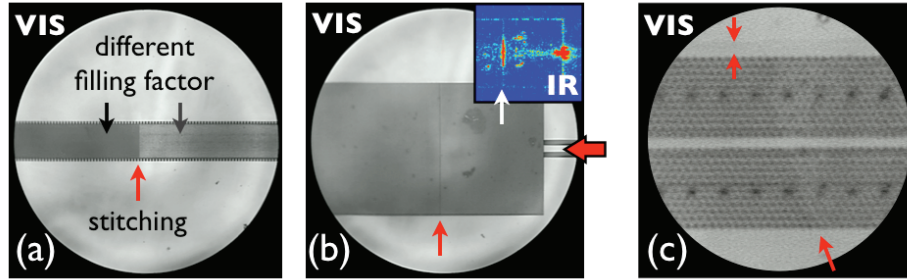
Figure 3.13: Fabrication errors visible with a standard optical microscopy: (a) filling factor change, (b) stitching errors, (c) a membraning problem.

The light from a blue light emitting diode (LED) is collected by a condenser lens system VL_1, VL_2 and collimated on the sample surface using either a low NA = 0.25 or high NA = 0.9 microscope objective (see Tab. 3.2 for specifications of the used objectives). In this way, a homogeneous illumination of the sample surface is achieved. The silicon or InP nanophotonic devices are not transparent in the visible wavelength range, which makes it possible to obtain a high contrast image of the sample surface in reflection configuration. Light reflected from the sample surface is collected by the same objective and projected by lenses VL_3, VL_4 and VL_5 on a CCD Camera as shown in Fig. 3.12(a). All lenses with exception of VL_2 are achromat doublets antireflection coated for the visible; VL_2 is a plano-convex lens. Changing the position of the VL_5 lens to VL_5' allows us to switch between high and low magnification. The combination of 470-nm illumination, high numerical objective of NA = 0.9 and the high magnification of the visible path make it possible to resolve features at the resolution limit of 300-nm, as demonstrated *e.g.* in Fig. 3.13(c) by imaging a photonic crystal device with distinctly resolved holes with a diameter of 250 nm and pitch of 420 nm.

Infrared path. The infrared (IR) path constitutes the main part of the imaging setup and it allows for both near-field imaging, *i.e.* imaging of the light intensity distribution at the sample surface, and the far-field, or Fourier-space imaging. Switching between the near-field and the far-field is accomplished by adding/removing one single lens.

Objective name, NA	Magnification	Focal VIS	Focal NIR	FWD	FN
Leica PL Fluotar, 0.25	10×	20.00	-	19.80	25
Leica PL Fluotar, 0.45	20×	10.00	10.08	2.4	25
Leica PL Fluotar, 0.85	50×	4.00	-	0.38	25
Leica PL Fluotar, 0.90	100×	2.00	2.01	0.28	25
Leica PL APO, 0.95	150×	1.33	-	0.20	28
Olympus LMPlanFI, 0.80	*100×	1.80	1.81	3.3	26.5

Focal = Focal Length (mm), FWD = Free Working Distance (mm), FN = Field Number (mm)

Table 3.2: Technical specifications of objectives used as a collecting lens in the FSI setup: FWD and FN are specified by the manufacturer for VIS; the correction for the NIR is in the order of 1%. Focal NIR is determined experimentally. All objectives are flat-field corrected for a tube length of infinity.
* specified for the tube lens of 180 mm, otherwise 200 mm.

Light radiated from the sample surface is collected by a high numerical aperture microscope objective (typically NA = 0.9; see Tab. 3.2), which is placed at one focal distance from the sample surface. It is indispensable that the collecting objective is flat-field corrected[1] for the infinite tube length to fulfill the Abbe sine condition and, hence, retain the Fourier-transforming property of an ideal lens. The sample surface, or alternatively the back focal plane of the collecting lens where the Fourier-space image is found, is projected onto a near infrared (NIR) camera by a series of IR-coated achromat doublets L_1, L_2, (L_3) and L_4 as shown in Fig. 3.12(c) and (d). The lenses are placed in the so-called f-f configuration, where the back focal plane of one lens coincides with the front focal plane of the following lens. All lenses are oriented with the convex facet towards the collimated beam in order to minimize spherical aberration.

The lens L_1 positioned after the collection objective creates the first intermediate near-field image RS_1, allowing for spatial filtering in the real-space. Properly positioned spatial filters (rectangular or spherical apertures, or spatial light modulator located in the near-field image plane) block light scattered at defects and structure interfaces as well as spurious reflections, which would otherwise contribute to speckle-like background noise in the far-field. As verified in experiment, scattering at sample imperfections decreases the signal-to-noise ratio and in the extreme case it can completely spoil the Fourier-space image. In this context, careful real-space filtering is a prerequisite for high-precision measurements.

The second lens L_2 performs another Fourier transform of the near-field patern, and the second intermediate Fourier-space image is formed in its back-focal plane. Such intermediate Fourier-space image brings along the possibility of spatial filtering in the Fourier-space, which makes it possible, *e.g.*, to filter out spurious back-reflections and recover a smoothly decaying loss profile of forward propagating mode as reported in [119].

The lens L_3 allows to switch between the real-space and the Fourier-space image and finally, the lens L_4 projects the image on the InGaAs Xeva camera (by XenICs), sensitive between 0.9 - 1.7 μm. The 320×256 pixel array of the camera with a pixel pitch of 30 μm is thermo-electrically cooled to 263 K, offering a 12 bit dynamic range.

---

[1]PL or Plan inscribed on the outer housing of the objective

Calibration

Calibration of the images in both real- and Fourier-space is done by several different methods, whose results are compared and cross-checked to assure the highest possible accuracy.

In the real space, the simplest and most accurate calibration technique is to image a reference object of known dimension and calculate the real space length corresponding to one pixel z_{1pix} directly. However, such calibration must be repeated whenever the setup is realigned or any of its elements is changed. It is often more practical to calculate the calibration constant from the optical magnification along the optical path, using the fundamental principles of paraxial optics:

$$z_{1pix} = c_{RS} \cdot \frac{1}{L_1} \frac{L_2}{L_4} \cdot p \cdot f_{obj} \tag{3.11}$$

here p stands for the camera pixel pitch, f_{obj} for the focal length of the collecting objective and c_{RS} is a correction factor. The correction factor stems from the approximation of real optical elements by ideal, infinitely thin ones, from neglecting the chromatic aberrations, as well as from small uncertainty in position of optical elements and the pixel dimensions of the camera chip. It is obtained by imaging a reference object of known dimensions and my be slightly different in the both perpendicular directions.

The Fourier space image can calibrated using one of the following methods:

From the paraxial optics. Similar calculation as in the real space leads to the following formula:

$$k_{1pix} = c_{FS} \cdot \frac{2\pi}{\lambda} \frac{L_1}{L_2} \frac{L_3}{L_4} \cdot p \cdot \frac{1}{f_{obj}} \tag{3.12}$$

where λ is the excitation wavelength and c_{FS} a correction factor in the Fourier space that is typically different from the correction factor in the real space.

From the numerical aperture of the collecting lens, which sets the limit of the maximal spatial frequencies present in the image. In other words, the circular pupil of the Fourier-space image corresponds to $k_{max} = NA\frac{2\pi}{\lambda}$, where NA is the numerical aperture of the collecting lens.

From the emission pattern of a reference grating. The diffraction orders of a periodic grating are equidistantly spaced in the Fourier-space, and their separation is equal to $k = \frac{2\pi}{\Lambda}$, where Λ is the known period of the reference grating. Therefore, by measuring the k-space separation of two adjacent diffraction orders and comparing it to the known quantity $\frac{2\pi}{\Lambda}$, one finds the value of k_{1pix}. Of all the methods, this one is the most accurate and is therefore used to calculate the correction factor c_{FS} in Eq. 3.12.

Calibration formulas for the current FSI setup and the microscope objective of NA = 0.9 are summarized in Tab. 3.3.

Resolution

In the real space at near-infrared wavelengths, the resolution R, *i.e.* the minimal distance between two distinguishable points, is limited by the Raileigh criterion $R = 0.61\frac{\lambda}{NA}$, which corresponds to ~ 1 μm for the objective of NA = 0.9 and the wavelength 1.5 μm.

Dimension	Formula	Value for 1 pixel
FS k_z (horizontal)	$k_{1pix} = 0.946 \cdot \frac{2\pi}{\lambda} \frac{300}{400} \frac{300}{500} \cdot 30 \cdot \frac{1}{2010}$	$0.02576 \ \mu m^{-1}$
FS k_y (vertical)	$k_{1pix} = 0.96 \cdot \frac{2\pi}{\lambda} \frac{300}{400} \frac{300}{500} \cdot 30 \cdot \frac{1}{2010}$	$0.02614 \ \mu m^{-1}$
RS z (horizontal)	$r_{1pix} = 1.01 \cdot \frac{1}{300} \frac{400}{500} \cdot 30 \cdot 2.010$	$0.162 \ \mu m$
RS y (vertical)	$r_{1pix} = 1.02 \cdot \frac{1}{300} \frac{400}{500} \cdot 30 \cdot 2.010$	$0.164 \ \mu m$

Table 3.3: Calibration formulas in the Fourier-space and the Real-space for objective NA = 0.9.

The situation is more complicated in the Fourier space, where the minimal spot-size, and, hence, the resolution, primarily depends on the field of view (FW) of the imaging setup, and secondarily, is limited by the raster of the IR camera chip. In our experimental system, the optical element that limits the field of view is the collecting microscope objective with FW = Field Number[2]÷Magnification. For the standardly used objective 100x, NA = 0.9, the FW is as large as 250 μm and the corresponding resolution in k-space $\Delta k = 1.22/\text{FW} = 0.005 \ \mu m^{-1}$.

The resolution given by the raster of the IR camera chip is equal to $2k_{1pix}$, *i.e.* twice the k-vector value corresponding to one pixel obtained from the calibration procedure. For the objective 100x, NA = 0.9, the value of $2k_{1pix} = 0.05 \ \mu m^{-1}$ (see Tab. 3.3), which is one order of magnitude larger than the resolution given by the field of view.

In the current experimental setup, the k-space resolution in clearly limited by the pixel pitch of the camera to $0.05 \ \mu m^{-1}$. Nevertheless, this can be easily increased by magnifying the final Fourier-space image, *e.g.*, by replacing the lens L_4 by a lens with a larger focal distance or a more complicated lens system Alternatively, the collecting objective can be replaced by a lens with lower magnification and a larger field of view.

The resolution limit imposed by the camera pitch can be also largely increased by numerical post processing of the image data, *e.g.* by fitting and tracking the spot position in k-space. In the particular case of excellent signal-to-noise ratio, no overlap between features and an ideal feature size covering 5-10 pixels, the resolution can be increased up to 10 times, *i.e.* to $0.005 \ \mu m^{-1}$.

---

[2]Field Number gives the diameter of the viewfield expressed in millimeters as measured at the intermediate image plane. It is specified by the manufacturer as in Tab. 3.2

Chapter 4

Dispersion properties of nanowire waveguides

Dispersion relation of nanowire waveguides exhibits a simple, close-to-linear dependence within a broad spectral range, which can be in most cases rather easily calculated by a number of numerical tools. However, the dispersion and, especially, its higher order derivatives such as group velocity and group velocity dispersion (GVD) vary finely with small change of the structural parameters, which can't be avoided even with the state of art fabrication techniques. The question to be asked is how precisely the numerical tools can simulate the real dispersion of nanophotonic devices. The precise knowledge of group velocity, for instance, is crucial for identifying the phase matching conditions between interacting pump and probe beams that must be addressed to increase nonlinear efficiencies [120]. The exploitation of such non-linear effects in high index contrast SOI waveguides is currently an active research area [13,121] and in this context efficient, reliable and *accurate* experimental dispersion measurement techniques are highly appealing.

In the first part of this chapter, we use the Fourier-space imaging technique to experimentally investigate the dispersive properties of Si nanowire and slot waveguides by analysing the emission diagram either of residual scattering losses or of losses induced by properly engineered probes. Nanowire waveguides are simple enough to callibrate and validate the limitations our experimental approach, and at the same time, the experimental results are interesting for a large scientific community due to their frequent use. We also demonstrate that current advanced e-beam patterning process still induces coherent optical losses that are associated with periodic subnanometer perturbations of the dielectric map of the waveguides.

Nanowire waveguides are often used as a fundamental building block of more complicated optical components, such as directional couplers or coupled-waveguide arrays, which can be found in all-optical switches, cross-connects, add-drop multiplexers, or in a variety of interferometric devices such as Mach-Zehnder interferometers. Increased complexity of such devices leads to complicated dispersion, and, in consequence, to an accentuated need for accurate experimental characterization. In the second and third sections, we illustrate the suitability of the Fourier-space imaging for this purpose, showing that its applicability reaches far beyond measuring the dispersion of straight nanowire waveguides. More specifically, the second sections reports on dispersion measurement of coupled co-directional waveguides, and in the last section, the Fourier-space imaging is applied to investigate emission properties of optical phased arrays intended for off-chip beam steering.

4.1   Nanophotonic rectangular and slot waveguides

The top-view scanning electron microscope (SEM) images and cross-sectional layouts of the investigated waveguides are shown in Fig. 4.1(a). The rectangular waveguides have the nominal width of 300 and 400 nm (labelled as R300 and R400, respectively) and were fabricated in a 300 nm thick silicon layer on top of a 1-μm-thick buried oxide layer. According to simulations by film mode matching method [78], such waveguides with air-cladding are singlemode, supporting both the fundamental TE-polarized and the fundamental TM-polarized mode.
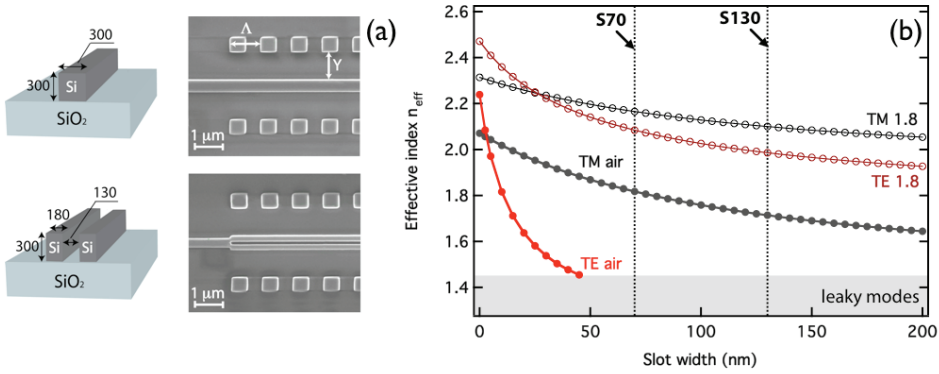

Figure 4.1: (a) Perspective layout and top-view SEM images of rectangular R300 and slot S130 wire waveguides. (b) Calculated effective index of slot wire waveguide modes plotted as a function of the trench width for air (n = 1, filled circles) and polymer (n = 1.8, empty circles) trench and overlay cladding.

Concerning the slot waveguides, their lateral profile consists of two 180 nm wide silicon sections spaced by an air trench of 70 and 130 nm, labelled as S70 and S130, respectively. Slot waveguides were firstly proposed by Almeida et al. [13, 14] as a special type of waveguide that can enhance and confine the field of the TE-polarized fundamental guided mode in the nanometer-wide slot filled with a low index material. Physical origin of this confinement stems from a large discontinuity of the transverse component of the Electric field at the Si-air interface, while much higher amplitude is at the low-index side. The slot waveguide mode can be seen as a superposition of the fields at both interfaces, resulting in the E-field enhancement in the slot by a factor of $n_{Si}^2/n_{air}^2 \approx 12$ for Silicon-air interface [13]. If the trench is filled with nonlinear material, a large overlap between the material and the mode-field is achieved and an important enhancement of the nonlinear effects is expected.

In the current project, the original purpose was to infiltrate the slot with organic nonlinear material, such as DDMEBT polymer with refractive index of n_0 =1.8 and off-resonant Kerr coefficient n_2 approximately $(1.7 \pm 0.8) \times 10^{-17}$ m^2 W^{-1} at the wavelength of 1.5 μm [122], in order to study the enhancement of Kerr processes such as ultrafast Kerr-induced all-optical wavelength conversion. The principal task of our laboratory was to accurately measure the dispersion of the waveguides before and after the slit filling, to observe the shift of the dispersion and identify the phase matching condition for the pump and probe beams. The second part of the project was never realized due to poor homogeneity of the trench filling. Figure 4.1(b) shows the theoretically calculated effective refractive index of the slot waveguide modes for an air-clad and polymer-filled slot

waveguides, plotted as a function of the trench width (calculations performed in collaboration with Prof. J. Čtyroký at the Institute of Photonics and Electronics ASCR, Czech Republic). With the current design and air-filling, the slot waveguides support only a single TM polarized mode, *i.e.*, the interesting fundamental TE mode is not guided. This mode would, however, appear if the trench is filled with the polymer of refractive index of $n_0 = 1.8$.

Besides the waveguide design, the Fig. 4.1(a) shows also the design of a linear probe gratings (LPG) formed by square pillars, which have been etched on both sides of the waveguides at the separation distance of $Y = 1$ μm and $Y = 3$ μm in order to probe the evanescent tail of the guided field effectively and with a minimal disturbance. The $\Lambda = 1$ μm period of the LPGs was carefully chosen to fold the dispersion curve of the waveguides into the light cone, *i.e.* to couple the guided modes into the radiative continuum.

Both samples were processed at AMO, Germany, using standard electron-beam lithography (EBL) followed by reactive-ion etching (fore details see section 2.3.4), within the collaboration with the group of Dr. Michael Först at the University of Aachen.

4.1.1   Fourier-space imaging and the side-wall roughness

Propagation constant of both the guided modes was measured using the Fourier-space imaging as described in Chapter 3. Polarization of the excitation was set to 45° so that both the TE and TM polarized modes were excited at the same time, and the light scattered from the sample surface was collected by the NA = 0.9 microscope objective. The reconstructed Fourier-space measured for each of the structures at the excitation wavelength of 1620 nm and for the grating - waveguide separation of $Y = 1$ μm, is presented in Fig. 4.2. It consists of a pattern of vertical lines that is characteristic for each individual waveguide design.
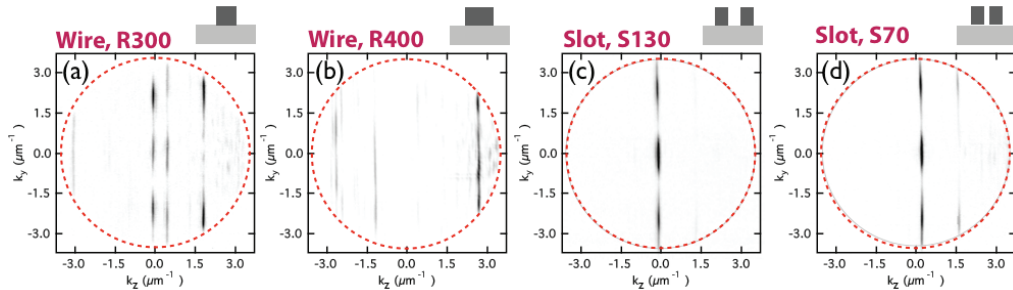
Figure 4.2: Characteristic far-field pattern measured at the wavelength of 1620 nm for all four considered waveguide designs: (a) R300, (b) R400, (c) S130, (d) S70.

To explain the physical origin of the pattern, let's first focus on the example of the 300-nm-wide rectangular wire waveguide shown again in figure 4.3 a) and b), for $Y = 1$ μm and $Y = 3$ μm, respectively. For $Y = 1$ μm, the pattern exhibits two groups of sharp straight lines RG1^{TM}, RG1^{TE}, RG2^{TM}, and PG^{TM}, PG^{TE}, perpendicular to the 1–dimensional propagation direction $\vec{k}_{prop}$ and limited by the pupil of the collecting lens.

Note first, that the "PG" lines are present only for the grating - waveguide separation distance of $Y = 1$ μm while for $Y = 3$ μm, *i.e.* for a decreased interaction between the guided mode and the LPG, the PG^{TM} and PG^{TE} lines are missing. These lines are therefore attributed to the radiated fields of the fundamental transverse magnetic (TM)
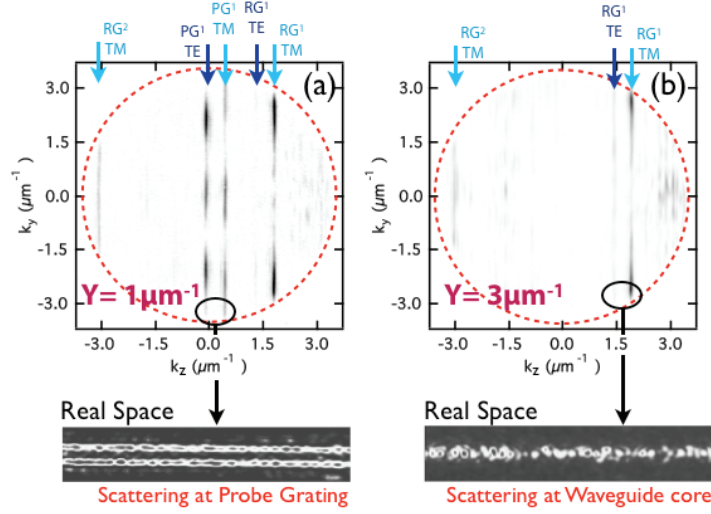
Figure 4.3: Far-field pattern of the R300 waveguide for the waveguide - grating separation distance of (a) $Y = 1$ μm, (b) $Y = 3$ μm. Vertical lines of the pattern are identified as TE and TM polarized modes corresponding to light scattered as intentionally designed probe grating ("PG" lines) and residual side-wall grating ("RG" lines). Real space (near-field) pattern corresponding the the "PG" and "RG" lines is shown at the bottom of figures (a) and (b), respectively.

and transverse electric (TE) modes of the wire waveguides scattered by the LPGs. The hypothesis was confirmed by near-field imaging; by applying an appropriate filter in the intermediate Fourier plane FS (see Fig. 3.12), we can block the "RG" lines and observe the near-field pattern corresponding exclusively to the "PG" lines. As shown in Fig. 4.3, such pattern is indeed located at the LPG, etched at both sides of the waveguide. The optical signal radiated from each individual LPG interfers in the far-field, producing the modulation observed along the $k_\perp$ direction. The TE and TM polarization assignment was performed by polarization analysis in the collecting path.

On the other hand, the far-field "RG" lines, which corresponding image in the near field is located at the waveguide core (Fig. 4.3(b)), are not related to the scattering at the LPGs. This is also confirmed by the fact that their intensity profile does not depend on the LPG separation Y as evidenced in Fig. 4.3(a) and (b). Looking at the vertical profile of the "RG" lines, the signal is mainly located near the boundary of the pupil of the collecting lens. This indicates that the light is preferentially scattered within the plane of the sample, supposedly by a vertical surface constituted by the waveguide sidewalls. Therefore, we attribute these lines to the first and second orders of a small corrugation gratings on each sidewall of the wire waveguides. The k_{prop} spacing between the RG1^{TM} and RG2^{TM} corresponds to a spatial modulation of 1.28 μm, which is exactly the dimension of the trapezoidal write sub-field border used in the e-beam lithographic process as explained in section 2.1.1.

The aforementioned experimental observations imply that the residual nanometer-scale imperfections inherent to the technological processing such as subfield fracturation still result in optical scattering loss detectable by standard far-field imaging. Note that these imperfections are not visible at the SEM images, and optical imaging is an unique way to identify them, and possibly quantify. On the other hand, scattering at a residual grating

is a coherent process that conserves the phase of the input guided field. In combination with the FSI, it can be used to non-invasively reconstruct the propagation constant and dispersion properties of the supported modes as shown below:

From the knowledge of the reciprocal vector of both the probe and the residual gratings and the k_{z_0} position of the lines, the mode propagation constants are entirely determined as shown in Fig. 4.4. Note, that folding the "PG" and "RG" by an appropriate reciprocal grating vector results in strictly identical values of reconstructed propagation constants for both polarizations. This *a posteriori* confirms the 1.28 μm periodic corrugations at the sidewalls. In addition the results for $Y = 1$ μm and $Y = 3$ μm are strictly identical in the resolution limit of the set-up which demonstrates the non-invasive nature of the LPGs approach. Note also that the determination of the wave vector of the TE modes of the 400 nm wide waveguide corresponds to an effective NA of the far-field microscope as high as 2.5.
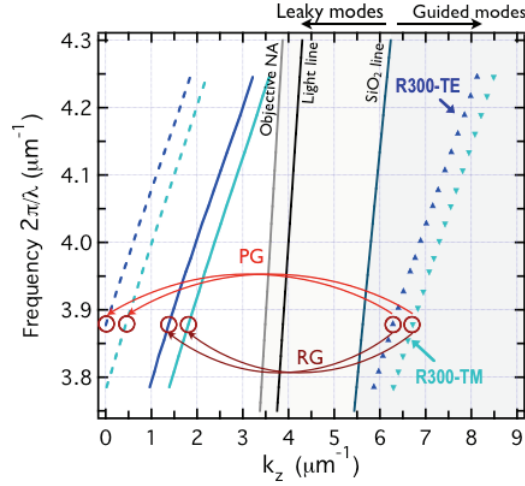
Figure 4.4: Reconstruction of the guided mode dispersion by unfolding the measured dispersion curve by one reciprocal vector of the probe (resp. residual) grating.

Fig. 4.5(a) and (b) plot the reconstructed dispersion curves for the wire and slot waveguides, respectively, as the excitation wavelength was tuned within 1480-1660 nm. The narrowing of the waveguide width as well as the presence of a slit are accompanied with a decrease of the modal effective index as a result of the guided mode spreading into the surrounding low index material. In agreement with theoretical calculations, for the slot waveguides with given dimensions, only the TM modes are supported.

Comparison of these experimental dispersion curves with simulations reveals a very good agreement for the 400-nm-wide rectangular waveguide. Small discrepancies that are observed for other waveguides investigated can be assigned to either substrate thickness variations, or larger uncertainties in lateral dimensions of nanowires introduced upon fabrication. The deviation is most pronounced for the S70 waveguide (70-nm wide slot), where the relative error in the slit thickness is expected to be the largest. Another effect that may play a role but was disregarded in the dispersion calculations is the influence of the mode leakage into the Si substrate, which is separated by only 1-μm-thick SiO_2 layer from the waveguide core region.
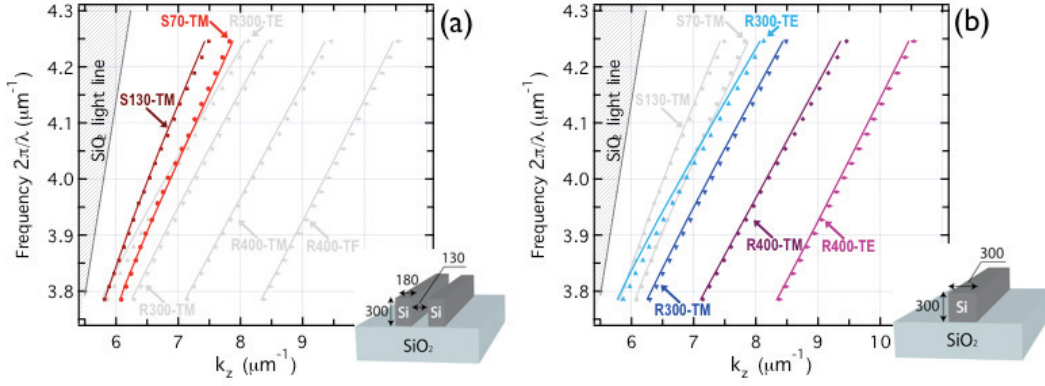
Figure 4.5: Experimentally measured dispersion of slot (a) and rectangular (b) nanowire waveguides.

Fig. 4.6 shows the group index $n_g = c\frac{\mathrm{d}k}{\mathrm{d}\omega}$ of all investigated modes, which was obtained by numerical differentiation of the experimental dispersion data. The observed group index reaches values up to 5.2 and 4 for the wires and slot waveguides, respectively, which is notably larger than the material index of silicon. The high group index values as well as the anomalous group index dispersion result from the effect of the sub-wavelength waveguide geometry that dominates the material dispersion [123, 124].
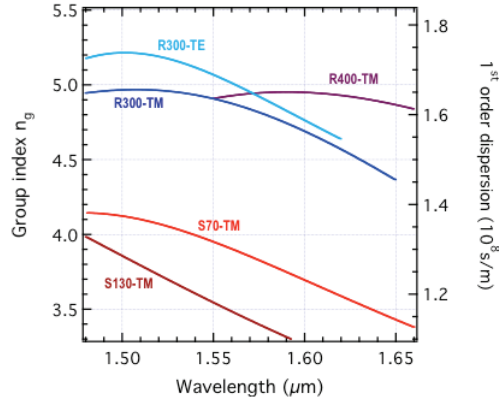
Figure 4.6: Group index and first order dispersion calculated by numerical differentiation of the measured dispersion curve.

4.2   Co-directional couplers

In this section, the Fourier-space imaging technique is applied to directly probe the fundamental physical interactions within the coupled waveguide structures. More specifically, we focus on the state-of-the-art co-directional waveguide couplers based on Silicon-On-Isolator (SOI), which are characterized by coupling lengths typically about 10 μm (or even shorter in a photonic crystal environment), and propagation losses as low as 2.5 dB/cm [8,10].
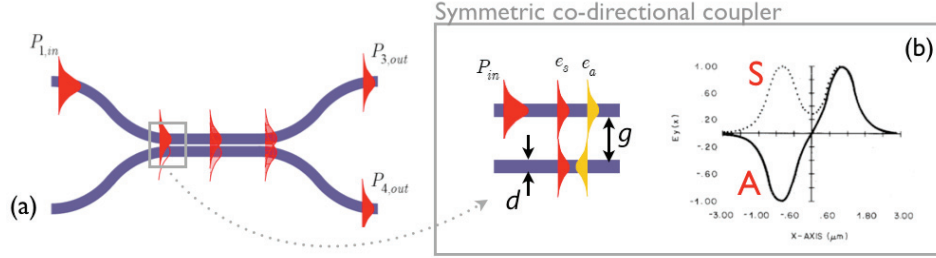
Figure 4.7: (a) Schematic drawing of a co-directional coupler. (b) Symmetric and antisymmetric mode of a directional coupler. Calculated mode profiles adopted from [125].

The physical properties of coupled waveguides have been intensively studied since the early days of integrated photonics in 1970s, both theoretically and experimentally. Along with numerical simulation tools (Finite-difference time-domain or guided mode expansion methods), analytical coupled mode theory proved suitable for modelling the mutual intensity transfer within the coupled systems [126, 127]. As follows from the coupled mode theory, the guided mode of an isolated waveguide splits into two as soon as the mutual coupling with a second, identical waveguide is introduced. As shown schematically in Fig. 4.7, the split modes can be categorized as a symmetric and an antisymmetric one, according to the symmetry of the mode field in respect to the waveguide structure. Each of the modes has a different propagation constant and therefore, their mutual phase relation changes periodically as a function of the length of propagation. This leads, in return, to a periodic exchange of the energy between the waveguides with a period equal to twice the so-called coupling length L_c:

$$L_c = \frac{\pi}{\Delta k} = \frac{\pi}{|k_S - k_A|} \tag{4.1}$$

where k_S and k_A denote the propagation constants of the symmetric and antisymmetric modes, respectively.

Up to now, the experimental verification has been almost exclusively limited to transmission measurements [9], which provide spectral information about the coupler performance, but cannot probe the coupling length or the coupled mode dispersion directly. However, using the Fourier-space imaging, the mode splitting of the original isolated waveguide mode is observed directly in the k-space and the dispersion relation of the split modes is studied in detail for different coupler geometries. From the Fourier space images, valuable information about the coupling length/strength and its spectral dependence can be directly reconstructed, with high accuracy and without the need for time-consuming repetitive measurements.

Symmetric directional couplers and isolated reference wire waveguides were designed

and fabricated in a silicon layer using a silicon-on-insulator (SOI) wafer (220 nm$\pm$5 nm thick Si layer on top of a 2 μm SiO$_2$ buffer) within the ePIXnet nanostructuring platform in St. Andrews. Total of 21 different coupler and waveguide structures with varying wire width d (from 320 to 460 nm) and coupled waveguide separation distance g (from 220 to 390 nm) were prepared from seven distinct mask patterns (labelled as A-G) under different e-beam-dose conditions. An overview of the designs including exact structural parameters determined from the scanning electron microscopy (SEM) are summarized in Table 4.1. The present coupler designs are intended for operation under TM-polarized excitation; efficient coupling of TM-polarized modes results in coupling lengths several times larger that the excitation wavelength, $i.e.$ $L_c \approx 7$ μm. This is not the case for weakly interacting TE-polarized modes, whose coupling lengths at the given waveguide separation distance g were as large as 100 μm. Therefore, in the further text, only the TM-polarized modes are considered.

| | Dose D0.9 | | | Dose D1.0 | | | Dose D1.1 | | |
	d	g	L_c	d	g	L_c	d	g	L_c
A	460	220	**6.3**	435	245	**6.7**	390	290	**6.6**
B	460	250	**7.4**	430	280	**7.5**	390	330	**7.6**
C	460	300	**9.6**	430	330	**9.8**	385	375	**9.5**
D	430	220	**5.6**	400	250	**5.6**	350	296	**5.8**
E	405	225	**5.2**	380	250	**5.2**	330	300	**5.3**
F	395	260	**6.3**	375	285	**6.0**	325	330	**6.3**
G	390	320	**7.6**	370	345	**7.8**	320	390	**7.9**

Table 4.1: Overview of structural parameters and experimentally measured coupling lengths of all investigated coupler designs.
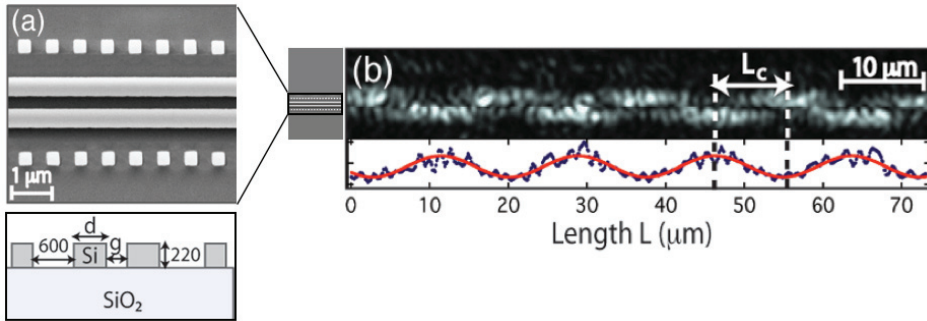
Figure 4.8: (a)Top-view SEM image and schematic cross-sectional layout of directional coupler with linear probe grating (LPG) designed alongside the structure; dimensions are given in nanometers. (b) Corresponding near-field IR image. Below: intensity profile at the bottom LPG.

A typical top-view scanning electron microscope (SEM) image together with a schematic cross-sectional layout of the final device is given in Fig. 4.8. Besides the coupler, a linear probe grating with the period $\Lambda = 700$ nm was designed at both sides of the coupled waveguides at the waveguide-grating separation distance of 600 nm. As in the previous case of

nanophotonic wire waveguides, the purpose of the grating was to coherently scatter a small portion of the guided light into the far-field. Standard imaging of the sample surface yields a real-space image, which reflects the intensity distribution of light scattered at each of the two LPGs. As shown in Fig. 4.8(b), this allows us to map the intensity transfer between the coupled waveguides. In the absence of the probe gratings, no intensity pattern can be observed, because of the low intrinsic scattering loss of SOI structures as well as the low spatial resolution of the NIR imaging, which cannot resolve two closely spaced wire waveguides.
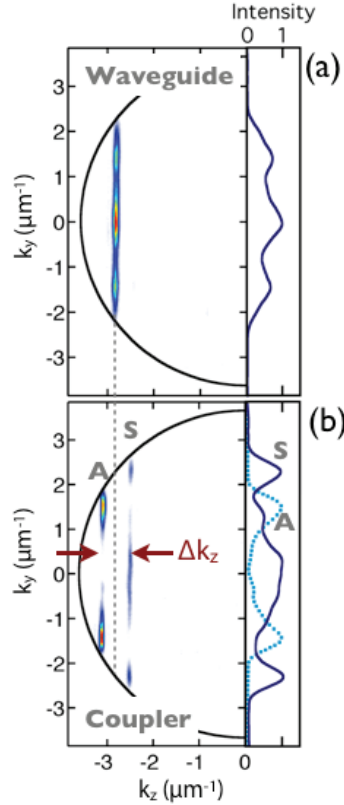
Figure 4.9: Far-field image of a reference wire waveguide (a) and directional coupler (b) of identical cross-sectional dimensions measured at $\lambda = 1550$ nm. The corresponding vertical line profiles are shown at the right.

Figures 4.9(a) and (b) show a far-field image of a reference wire waveguide and a directional coupler of the same waveguide geometry ($d = 380$ nm, $g = 250$ nm). While the k-space image of an isolated waveguide yields a single line shape, the directional coupler figure consists of two closely spaced lines, characterized by different modulation pattern along the vertical k_y axis. The two lines correspond to the two modes of the coupled waveguides, which appear upon splitting of the isolated waveguide mode in the coupled configuration. While the position of the lines along the k_z axis determines the propagation constant(s) of the modes, careful analysis of their k_y profile makes it possible to identify their symmetry: As the guided field is diffracted at the two LPGs, it produces an interference pattern that is

observed in the far-field along the k_y direction (plotted in the right sector of Fig. 4.9(a) and (b)). An intensity maximum of the interference profile at $k_y = 0$ implies that the field at both LPGs is in phase and the mode under investigation is symmetric. On the other hand, the far-field intensity of the antisymmetric mode, which has an opposite phase at each of the LPGs, must drop to zero at $k_y = 0$ as a result of destructive interference. Following these considerations, symmetry assignment of the measured modes was performed as indicated in Fig. 4.9(b), where A designates the anti-symmetric and S the symmetric modes.

Figure 4.10(a) shows the measured dispersion diagram of the coupled modes of directional coupler with d = 370 nm and g = 345 nm compared to the dispersion curve of the isolated reference waveguide. In both cases the dispersion curves were obtained by recording the spectral shift of the k_z line position when tuning the excitation wavelength from 1480 to 1650 nm, which was then folded by one reciprocal vector of the LPG grating $k_{R/A/S} = k_z + 2\pi/\Lambda$, where k_R, k_S, k_A are the propagation constants of the reference waveguide, the symmetric and the antisymmetric split modes, respectively. Dashed lines that are also shown in the figure represent the dispersion curves simulated by the guided mode expansion based CAMFR solver [128]. A very good agreement between the theory and experiment is achieved, especially for the frequencies well above the mode cut-off.
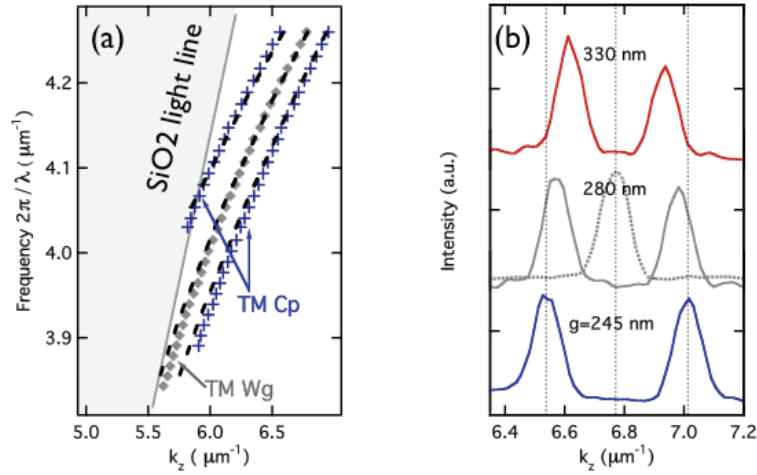
Figure 4.10: (a) Experimental dispersion curve of symmetric and antisymmetric modes of a directional coupler ($d = 380$nm, $g = 250$ nm) and a reference waveguide ($d = 380$ nm) compared to numerical simulation by CAMFR (dashed lines). (b) Far-field line profiles along k_z plotted for a constant wire width $d = 430$ nm, wavelength $\lambda = 1500$ nm and decreasing waveguide separation distance g (couplers - solid line, reference waveguide - dotted line).

The magnitude of the mode splitting Δk_z is a direct measure of the coupling strength, increasing for enhanced interaction between the coupled waveguides. It is proportional to the mode field overlap between the two waveguides, which depends in particular on the proximity of the two coupled waveguides g and the waveguide width d. The latter is a measure of the lateral mode field confinement. As an example, Figure 4.10(b) illustrates an increase in the mode splitting Δk_z when decreasing the waveguide separation distance from 330 to 245 nm, keeping the constant waveguide thickness of 430 nm. In our experimental

configuration we can determine Δk_z with a precision[1] of 0.0025 μm^{-1}. Expressed in terms of the coupling length L_c, this can be measured with an accuracy of ± 50 nm, which is quite remarkable. The experimentally determined coupling lengths of the different designs range from 5 to 10 μ and are listed in Tab. 4.1.

In order to investigate the relation between the mode splitting Δk_z and the two structural parameters g and d more closely, we use the coupled mode theory derived for symmetric slab waveguides [125] combined with the effective index method. This approach allows us to express the mode splitting function $\Delta k_z = f(d, g)$ in an analytical form:

$$\Delta k_z = \frac{\pi}{L_c} = \frac{2\kappa^2\gamma \exp(-g\gamma)}{k_0^2 k_R \left(n_{eff}^2 - 1\right)\left(d + \frac{2}{\gamma}\right)} \tag{4.2}$$

where $\kappa = \sqrt{n^2 k_0^2 - k_R^2}$, $\gamma = \sqrt{k_R^2 - k_0^2}$, k_0 is the free space wave vector, k_R the d-dependent propagation constant of an isolated waveguide and n_{eff} is the effective refractive index of an unpatterned SOI membrane.

In Fig. 4.11(a), the theoretical mode splitting given by Eq. 4.2 is compared to the experimental data measured at $\lambda = 1500$ nm for all available coupler designs. In the theoretical model the effective index of the 220-nm thick Si device layer $n_{eff}^{TM} = 2.01$ was used and the propagation constant $k_R(d)$ was extrapolated from the experimental data measured on isolated reference waveguides. The two-dimensional function $\Delta k_z = f(d, g)$ is shown as a surface plot with dot markers at positions (d, g) corresponding to parameters of investigated devices. The markers help to visualize the discrepancy relative to the experimental values plotted in the same Figure as empty circles. An excellent consistency of the measured data and the theoretical results is achieved, demonstrating that the presented analytical model can closely describe the mode splitting even in 2D high index contrast SOI coupled systems.

Having a closer look at the Fig. 4.11(a), one can notice that within the studied parameter range, the magnitude of the mode splitting decreases roughly linearly with the wire width d and the waveguide separation distance g. The proportionality constants of this dependence have similar values for both parameters d and g, which means that if the wire width is increased and the gap thickness reduced by the same amount, the resulting change in the coupling strength is minimal. Hence, the quantity $d + g$ can be considered as a measure of the coupled interaction. This is demonstrated in Fig. 4.11(b), which plots the experimental coupling length of individual coupler designs as a function of $d + g$. The shaded region represents ± 5 nm uncertainty in the coupler lateral parameter specification. Such an uncertainty reflects the accuracy with which the dimensions of actual devices can be determined.

The coupling length L_c increases monotonically with $d + g$, nevertheless, it only weakly depends on the e-beam dose although the structural parameters vary upon the dose change considerably. Variation in the dose of the e-beam patterning keeps the sum $d + g$ constant and has therefore only a negligible effect on the resulting coupling length; for all three reported e-beam doses the relative difference in L_c lies within the error of the structural parameter specifications, as can be seen in Fig 4.11(b). Hence, once the proper mask design is available, the fabrication procedure is robust against small deviations from the target

---

[1]Two times higher resolution than stated in Chapter 3 is due to a different camera IR used for image acquisition with a approx. two times smaller pixel pitch
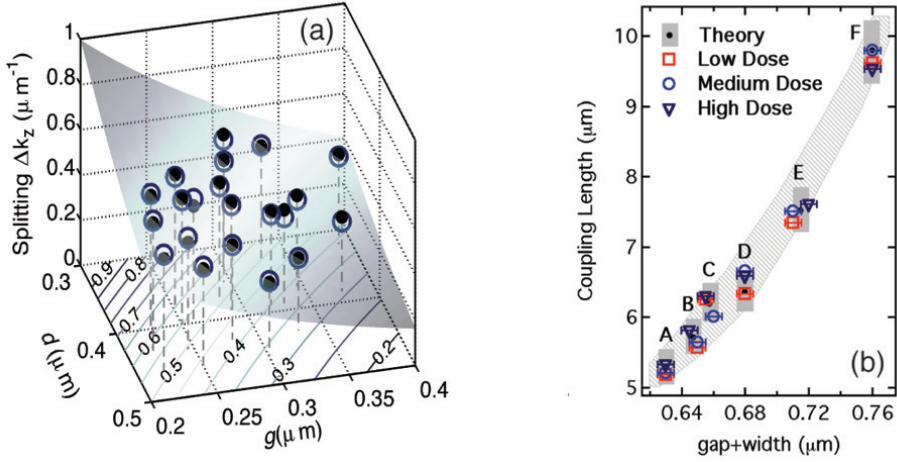
Figure 4.11: Magnitude of the line splitting $\Delta k_z(d,g)$ at $\lambda = 1500$ nm. Experimental data ($\bullet$) are compared to the theory (surface plot with $\circ$ datapoints). (b) Experimental and theoretical coupling lengths of different mask designs and e-beam doses from Tab. 4.1 (theory: medium e-beam dose only) plotted versus the sum of the wire width d and waveguide separation distance g. Theoretical coupling length $L_c(d+g)$ is shown as a shaded region.

settings that shall not influence the performance of the final devices.

To sum up, we have non-invasively and accurately determined the dispersion properties and the coupling lengths of directional couplers, and in addition, revealed a low sensitivity of the coupling length to the e-beam dose used upon fabrication. Beyond, it should be noted that due to local nature of LPG probes, the presented technique equally allows for on-chip measurements of more advanced systems, *e.g.* dynamic switches or coupled slow light PhC waveguides, where the increasing losses make the transmission measurements difficult.

4.3   Beam-steering with arrayed waveguides

Recently, there has been a lot of effort invested to the development of devices that allow for full-optical beam steering, either adopting the concept of phased arrays [129] or in photonic crystal environment [130]. The optical control allows for very stable, rapid and precise beam steering without mechanical motion, making the devices robust to specific external constraints such as acceleration. Within the collaboration with Prof. R. Baets, Dr. W. Bogaerts and K. Van Acoleyen from the Ghent University, we adopted the concept of optical waveguide phased arrays that work on the same principle as microwave antenna arrays: the directionality of the output beam is controlled by the number of emitters, *i.e.* waveguides, and the steering is accomplished by controlling the phase relation between the individual waveguides in the array.

The schematic drawing of the device under study is shown in Fig. 4.12 and it principally consist of three sections: access waveguide section, section of phase control and finally, section of coupled waveguide arrays with embedded grating couplers for the optical signal

extraction.
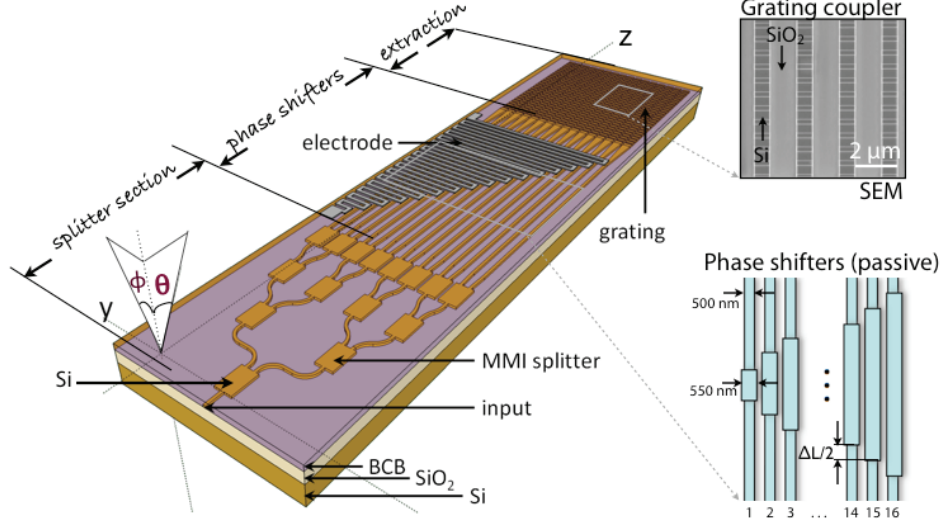
Figure 4.12: Schematic drawing of the beam-steering device, showing the full layout of the sample and defining the principal angles (θ, Ψ) and directions (y, z). The two insets give a more detailed image of the passive phase shifter design and the grating coupler shallow-etched on the top of the arrayed waveguides.

The structure is excited with TE-polarized light via the end-facet of the sample as in a standard end-fire setup. The signal is firstly coupled into a 3 μm wide access waveguide, which is gradually tapered to the width of 500 nm, and subsequently split by a cascade of Multi-Mode Interference splitters (MMI) into 16 parallel waveguides of 500-nm width and lateral separation of 2 μm.

The section of phase control is realized in two ways: passive control and active phase control using the thermo-optic effect in silicon. In the first case, the waveguide width is locally increased by 50 nm as shown in Fig. 4.12 and the length of the modified waveguide section is gradually varied for adjacent waveguides to induce a linear phase shift. In the case of the active phase control, the device is planarised by 600-800 nm thick layer of benzocyclobutene (BCB) and a 100-nm thick titanium electrode is sputtered on top. When the current is flowing through the electrode, a linear phase shift is induced in the arrayed waveguides due to Joule heating and the specific shape of the electrode. At the end of this section, waveguides are adiabatically tapered to the width of 800 nm, retaining the same lateral period of 2 μm.

Finally, the device section for light extraction contains a 32 μm long first-order diffraction grating shallow-etched on top of each waveguide. The grating is characterized by a period of $\Lambda = 630$ nm and duty cycle of 0.5, and is optimized for efficient TE mode extraction.

The devices for both active and passive phase control were fabricated in SOI wafers with 220-nm thick Si device layer on top of a 2 μm burried oxide layer at IMEC in two steps. In the first step, the waveguides and the MMI splitters were fabricated, and in the second step the shallow-etched, 70-nm deep grating coupler was introduced. The processed devices

were investigated using the Fourier-space imaging technique at the excitation wavelength of $\lambda = 1550$ nm (if not specified otherwise). Besides the standard NA = 0.9 Leica objective, the long-working distance Olympus LMPlanFI objective with NA = 0.8 was used to collect light and perform the optical Fourier transform; this objective offers a sufficiently high numerical aperture, while leaving enough space above the sample surface to facilitate for the current injection.

Fig. 4.13 shows the far-field image of light radiated from the reference structure, *i.e.*, structure with zero phase shift between the adjacent waveguides. As can be seen in the figure, the TE-polarized optical signal is diffracted by the grating coupler in three principal directions, forming three highly directive beams. One beam is directed vertically from the sample surface and two others at wave vectors $k_y = \pm 3.14$ μm^{-1}, which corresponds to angles $\Phi = \pm 51°$ at $\lambda = 1550$ nm. The angles θ and Φ are defined as the outcoupling angles in the longitudinal plane, *i.e.* along the waveguide axis, and transverse plane, *i.e.* perpendicular to the waveguide axis, respectively, with respect to the normal of sample surface. The beam profiles along both perpendicular directions are shown in Fig. 4.13(b) and (c).
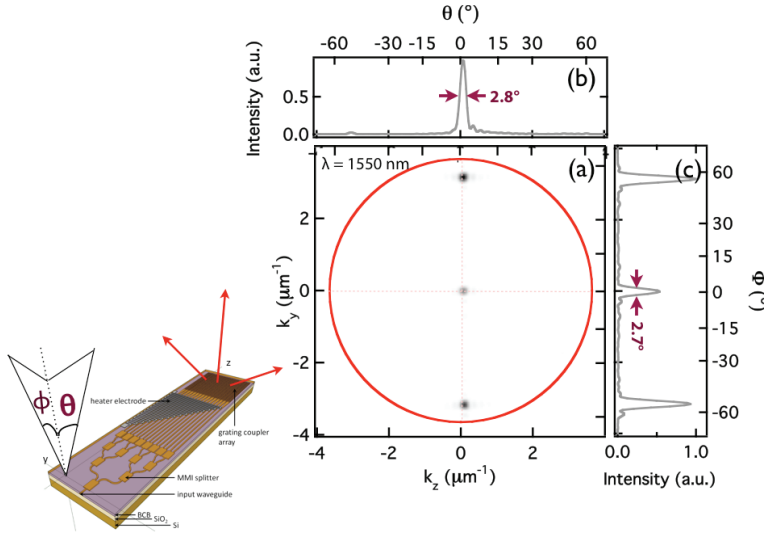
Figure 4.13: (a) Far-field image of light extracted from a reference device (no added phase shift between the waveguides). The three points in k-space represent three beams of close-to circular profile, directed at angles $\theta = 1.9°$ and $\Phi = 0°, \pm 51°$. (b,c) show the horizontal and vertical beam profiles, respectively.

The beam position and size along the k_z axis are determined by the specific design of the grating coupler. The linewidth Δk_z is given by the k-space broadening due to optical signal decay along the coupler and to the finite length of the coupler. The physics behind is the same as detailed in Section 3.2.1, where the line broadening due to radiation loss and finite size of the structure are discussed. The experimentally measured Δk_z of the peak at 1550 nm is equal to 0.2 μm^{-1} (2.8°).

In the k_y direction, the far-field profile depends primarily on the number N and separation d of waveguides in the array. The waveguide array acts as a grating with three diffraction orders inside the light cone at $k_y = 0, \pm \frac{2\pi}{d} = 3.14$ μm^{-1}, where d is the period of the waveguide array. The profile of each diffraction order is determined by the Fourier

transform of the total aperture size of the array ($\sim \mathrm{sinc}(\frac{Nd}{2\pi}k_y)$), resulting in the FWHM linewidth:

$$\Delta k_y = 0.886 \frac{2\pi}{Nd} \tag{4.3}$$

The experimentally measured $\Delta k_y = 0.19 \ \mu\mathrm{m}^{-1}$ (2.7°), which is in a close agreement with the theoretical linewidth of $0.175 \ \mu\mathrm{m}^{-1}$ (2.5°) calculated from Eq. 4.3. Finally, the relative intensity of individual diffraction orders is modulated by the angular intensity distribution of light radiated from a single waveguide. The latter, however, varies considerably as a function of the wavelength resulting in a threefold decrease of the intensity of the central beam when the wavelength is tuned from 1470 to 1660 nm. This intensity decrease upon tuning could be solved by using more directive elements of the array, *e.g.* by employing a more elaborate design on the grating coupler and/or the waveguides. Furthermore, the two oblique beams that are typically not desired for practical applications can be easily removed by slightly decreasing the waveguide separation d, which shifts the first diffraction orders below the light line.

Beam steering along the θ direction. The grating coupler shallow-etched at the waveguide core acts in a similar way as the probe gratings discussed in section 3.2.1: it diffracts a part of the propagating guided mode into the far-field, in the direction k_z given by the grating equation:

$$k_z = k_{z_{prop}} - \frac{2\pi}{\Lambda} \tag{4.4}$$

where $k_{z_{prop}}$ is the propagation constant of a waveguide in the array. By tuning the wavelength of excitation, the propagation constant $k_{z_{prop}}$ changes following the quasi-linear dispersion relation of the waveguide, and, hence, the emission direction k_z changes accordingly. Using the Fourier-space imaging, we can easily monitor the beam direction as shown in Fig. 4.14. Within our tuneable wavelength range of 1470-1660 nm, we can steer the beam by the 1.8 $\mu\mathrm{m}^{-1}$, which corresponds to approx. 26°.
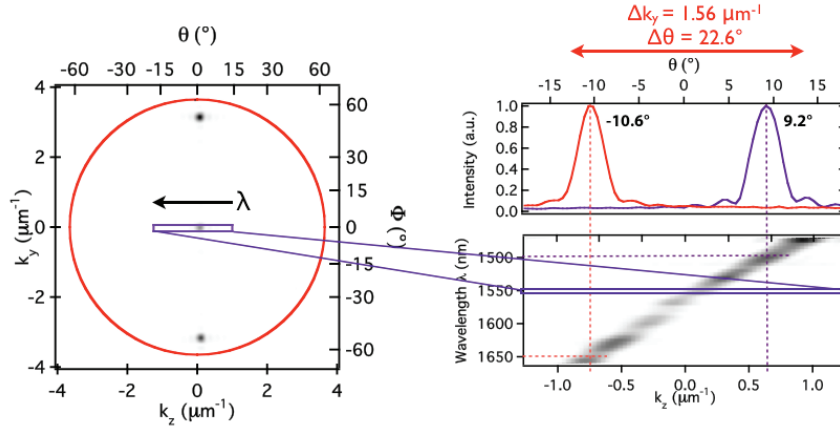

Figure 4.14: Wavelength steering. Figure shows how the position of the central beam shifts along the k_z axis when the wavelength of excitation is tuned between 1470 and 1660 nm. The k-space shift of the beam corresponds to the beam steering by angle $\theta = 26°$

Passive phase shift   The designed passive phase shifters have the length of L, $L + \Delta L$, $L + 2\Delta L$... $L + 15\Delta L$, imposing a linear phase ramp on the waveguides. The parameter ΔL, which varies from 0 to 10 μm in total of 11 different structures, determines the final relative phase shift φ between the waveguides and, hence, the emission angle Φ of the device. The direction of the diffracted beam is related to the relative phase shift φ by the following relation:

$$k_y = \frac{\varphi}{d}, \qquad \text{resp.} \quad \Phi = \arcsin\left(\frac{\varphi\lambda}{2\pi d}\right) \tag{4.5}$$

Fig. 4.15 illustrates how the central beam position is steered from $k_y = 0$ to $k_y = 1.56\,\mu\text{m}^{-1}$ (22.6°) by successive switching between structures 0 ($\Delta L = 0$) to 10 ($\Delta L = 10\,\mu\text{m}$). As expected, the beam deflection k_y increases linearly as a function of ΔL; small deviations are due to random phase errors resulting from the fabrication, which are also visible in Fig. 4.15 as a background noise.
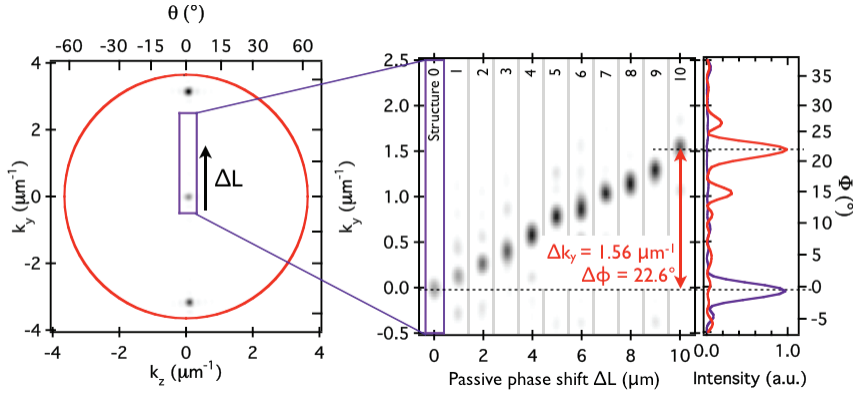
Figure 4.15: Passive steering. The passive phase shifters induce the shift od the central beam along the k_y axis, allowing for the beam deflection as large as $\Phi = 22.6°$ (structure design widh $\Delta L = 10\,\mu$m).

Active phase shift

The phase shift φ can be tuned dynamically by varying the magnitude of current injected into the heater electrode:

$$\varphi \sim c\frac{2\pi}{\lambda_0}\frac{\partial n}{\partial T}R\,I^2\Delta L \tag{4.6}$$

where $\frac{\partial n}{\partial T}$ is the thermooptic coefficient of silicon, RI^2 the Joule heat produced by an electrode of resistance R and direct current of magnitude I, ΔL is the difference of the electrode length of the adjacent waveguides and finally, c is a proportionality constant that relates the temperature change of the silicon waveguide ΔT to the Joule heat produced by the electrode.

The result of the active beam steering is reported in Fig. 4.16. The peak is no longer centered at $\Phi = 0$ owing to a fixed phase shift present in the investigated structure. By increasing the current from 0 to 3.95mA, the peak shifts continuously from 1.43 μm^{-1} to 1.59 μm^{-1}, *i.e.* by $\Delta k_y = 0.16\,\mu$m^{-1} (2.4°). Higher currents were not used owing to practical limitations and the possibility of burning the resistor electrode.
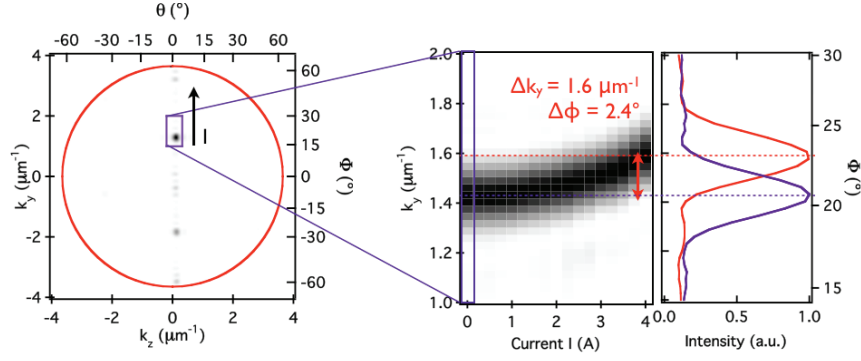
Figure 4.16: Active steering. Increasing the current in the heater electrode induces a continuous shift of the central beam along k_y by as much as $2.4°$ at $I = 4A$. Square dependence of the beam direction in k-space on the injected current I is clearly visible.

The shift of $2.4°$ implies a phase difference of $\varphi = 0.11\pi$ between individual grating couplers. The electrode thus imposes this phase shift on the first waveguide, twice the phase shift at the second waveguide, etc. The total phase shift induced by the electrode is $\varphi_{tot} = 0.11\pi(1 + 2 + ...16) = 14.28\pi$. The measured resistance of the electrode was $15\ \mathrm{k\Omega}$ of which approximately half was used for heating up the device. Hence, one can estimate the power needed for a π phase shift as $P_\pi = 8.2\ \mathrm{mW}$.

Chapter 5

Two-dimensional dispersion map of a bulk photonic crystal

Photonic crystal structures are characterized by complex dispersion, which on one hand complicates their physical understanding and structural design, but on the other hand makes them suitable for principally any application in the field of nanophotonics, as detailed in the introductory Chapter 1. In this context, dispersion relation represents a key characteristic for understanding and molding the light propagation within photonic crystals. The aim of this chapter is to present the experimental measurement of intricate two-dimensional dispersion relation of a bulk photonic crystal, obtained using the combined End-fire–FSI technique. Special attention is payed to the slow-light regime where the physics of light propagation - especially in the presence of residual disorder - is not yet fully understood.

5.1   2D Dispersion of triangular-type lattice photonic crystal

Bulk photonic crystal realized in a high-index slab represents the most fundamental example of a CMOS-compatible photonic crystal. The propagation of light in this structure is governed by a relatively simple dispersion relation shown in Fig. 1.9, which divides the frequency spectrum into photonics bands supporting optical modes and photonic bandgaps, where no extended Bloch solution exists. In this section, we will focus on the topmost part of the dielectric band of a triangular photonic crystal lattice, excited in the $\Gamma-K$ direction by TE-polarized light.

Figure 5.1 shows a top-view SEM image and the theoretical dispersion map of such a photonic crystal with the lattice constant $a = 380$ nm and filling factor $f = 35$ %. The calculations were performed using a 2-dimensional PWE method taking into account the dispersion of the slab waveguide. As can be observed in Fig. 5.1(c), the equifrequency surfaces (EFSs) at low frequencies have a circular shape centered around the Γ point. The comparison with the dispersion map of a homogeneous dielectric depicted in Fig. 1.1(a) implies that at the bottom of the band the photonic crystal behaves as a homogeneous isotropic medium. The light incident at the photonic crystal undergoes standard diffraction, independently of the direction of excitation.

However, as the frequency increases, the circular EFSs gradually evolve towards hexagonal shape with apexes oriented in the direction of the M symmetry points. The curvature of the EFSs in the $\Gamma-K$ direction decreases accordingly, becoming locally flat approxi-
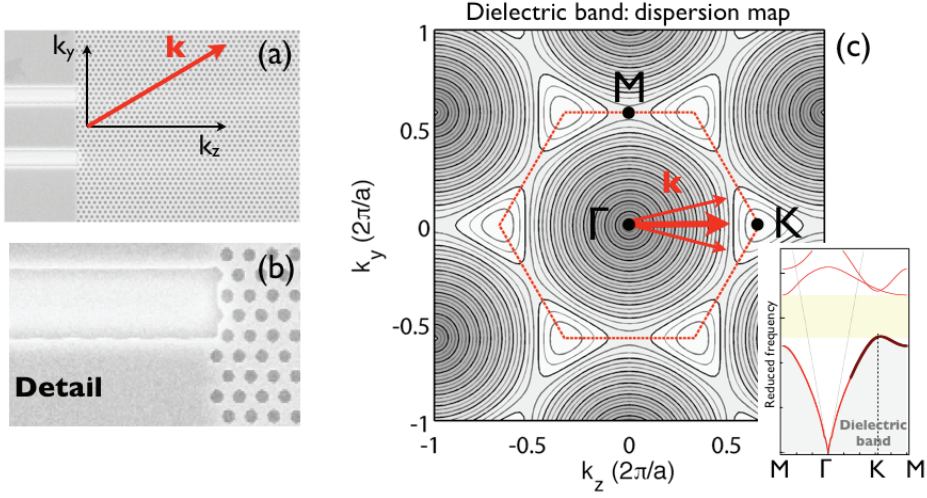
Figure 5.1: (a) Top-view SEM image of a bulk photonic crystal in Si slab including the input ridge access waveguide. (b) Theoretical dispersion map and dispersion curve (inset) of the dielectric band under TE excitation. Calculations were performed using the PWE and GME methods, respectively.

mately at the same frequency as the EFS reaches the M point. As explained in section 1.3.2, energy of optical beam incident at a flat EFS will propagate in one single direction given by the normal to the EFS, we speak about the phenomenon of self-collimation.

Further on, as the excitation frequency approaches the band edge, the EFSs take the trinagular form which gradually converges towards a singular point. At corresponding frequencies, the slope of the dispersion curve decreases as shown in the inset of Fig. 5.1(c), which implies a progressive slow down of the speed of propagation of the Bloch mode. At the extremum of the band edge, the group velocity reaches 0 and the optical field of the mode delocalizes across the whole structure. Such a behavior leads to creation of a broad-area band-edge mode with high density of states, which is particularly appealing for construction of band-edge photonic crystal lasers; both vertically and in-plane photonic crystal band-edge lasers have already been successfully realized in visible [38], infrared [39] as well as in terahertz wavelength range [40].
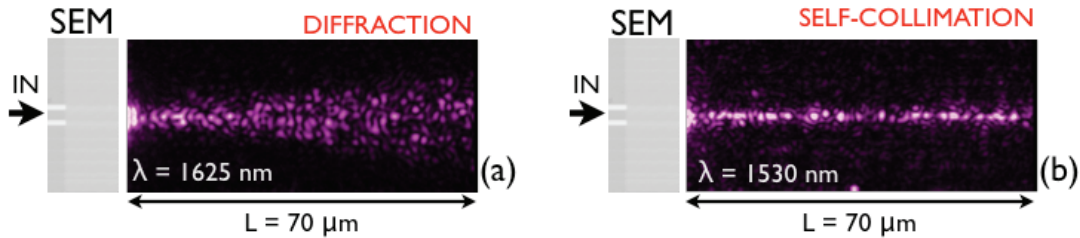
Figure 5.2: (a) Diffraction and (b) self-collimation regime observed in real-space due to light scattering at residual disorder (sample with $a = 350$ nm).

Generally, it is not straightforward to clearly visualize the above described effects in

experiment, primarily due to the fact that the Bloch modes of the dielectric band are found below the light cone. In the real space, one can typically trace the light propagation due to residual defects and imperfections that scatter light out-of plane as illustrated in Fig. 5.2. This allows us for example to discriminate between the regime of beam diffraction and collimation, however, in a general case, the exact dispersion characteristic is difficult to be retrieved using just a set of random scatters. In particular, such approach does not allow to map the EFS at the top of the dispersion band, where the optical signal is delocalized over all the structure and strong spatially incoherent back-scattering due to residual disorder is expected to occur [131].

### 5.1.1 Experimental reconstruction of the dispersion map

Using the Fourier-space imaging in combination with grating probes, we are able to visualize the dispersion map and its evolution towards the extremum of the dielectric band in experiment, including the interesting phenomenon of self-collimation as well as the regime of 'frozen' light at the extremity of the band. For this purpose, one can intentionally design a probe grating, *e.g.* a shallow-etched two dimensional surface grating as was done in related experiment of N. Le Thomas et al. [116], where he investigated the dispersion of square-type lattice photonic crystal. In the present work, however, we made use of a residual two-dimensional grating which origin is attributed to the e-beam patterning process.

The actual device was fabricated in SOI substrates of 220-nm-thick silicon layer on top of 2-μm-thick buried oxide layer. The lattice parameters of $a = 380$ nm (or $a = 350$ nm) and filling factor $f = 35$ % (the same as used for the calculations) were chosen to fit the topmost region of the dielectric band within the wavelength range of 1470-1660 nm. Low e-beam dose used for the sample patterning resulted in periodic corrugations, which are clearly visible at the sidewalls of the access waveguide (detailed zoom in Fig. 5.1(b)). Similar corrugations, although not visible in the SEM, were observed in the photonic crystal region in both perpendicular directions z and y. As the grating was not designed intentionally, it is a pure coincidence that the period of the residual gratings has just the proper value to fold both the K and M point into the light cone.

The process of reconstruction of the dispersion map around the K and M points is schematically shown in Fig. 5.3(a). The residual corrugation grating has the same period $\Lambda_z = \Lambda_{y_1} = 640$ nm in both perpendicular directions, as was retrieved from the experimental data. Note that the period is exactly one half of the residual grating period section 4.1.1, which indicates that it can be equally related to the size of the e-beam subfield border, just scaled by the resolution used to write the photonic crystal pattern. However, no conclusive statement can be made as the actual subfield size used to pattern the device is unknown. In addition, in the y direction, a second residual grating was observed, although its origin and period are difficult to clarify without a further systematic study.

The grating along the z-axis scatters preferentially the light propagating along Γ-K, while the perpendicular gratings scatter the light propagating along the Γ-M direction, folding the EFSs found in the proximity of the M-point into the light cone as depicted in Fig. 5.3(a). At the M-point, the EFS image is quadrupled due to the presence of double periodicity corrugation and the symmetric dispersion folding from both the upper and bottom Brillouin zone boundary.

The experimental equifrequency surfaces along the Γ-K direction recorded for increasing excitation wavelength from 1473 nm (corresponds to the top of the dielectric band) to
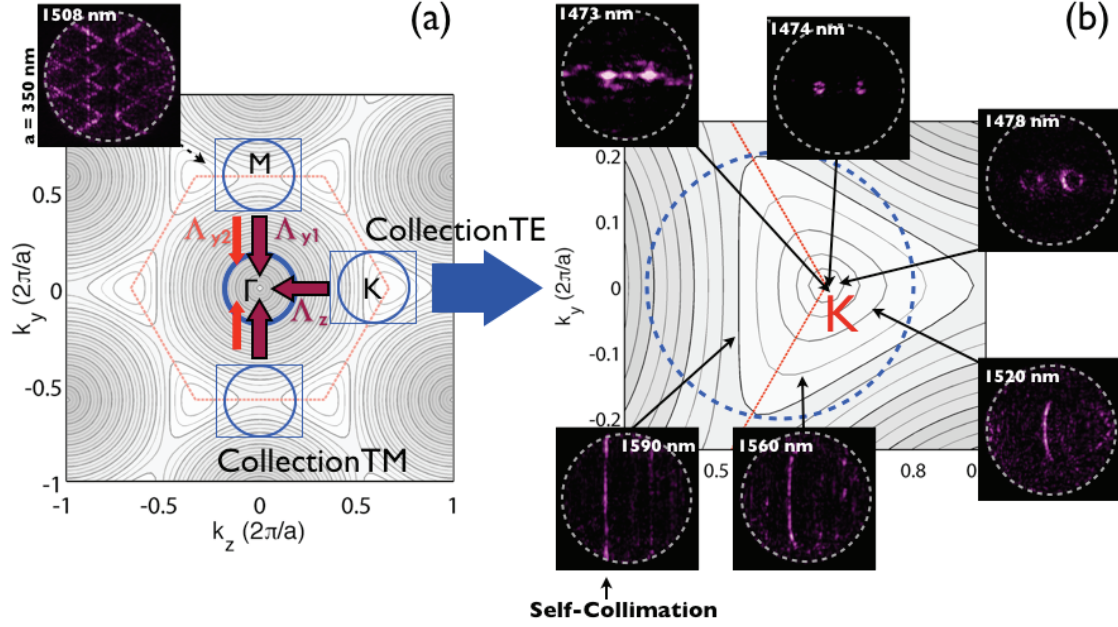
Figure 5.3: (a) Reconstruction of the dispersion map around the K and M points. (b) Evolution of the experimental dispersion map around the K-point from the top of the dielectric band down to the self-collimation regime.

1590 nm (self-collimation) are shown in Fig. 5.3(b). They clearly follow the theoretically predicted change of the EFS curvature, that manifests the transition from diffractive to self-focusing regime. The phenomenon of self-collimation is observed at the frequency of 1595 nm, in both Fourier space, where the equifrequency surface form a straight line along k_y, and the Real space, where the near-field image of light scattered at residual imperfections shows a narrow, collimated beam.

With exception of the topmost region of the dielectric band, the EFS with positive slope of the group index are mainly excited due to unidirectional excitation scheme. However, above approx. 1520 nm, weak excitation of the backward-propagating Bloch mode is observed, attributed to back-scattering at residual defects. The intensity of the backward component increases as the frequency approaches the extremum of the dielectric band, which is correlated with the decrease of the group velocity and the onset of the slow-light regime. Similar increase in the disorder-induced coherent back-scattering in the slow light regime was experimentally observed in 3D and 2D photonic crystals [116, 131] and one-dimensional waveguide structures [132, 133]. At the very top of the dielectric band, the EFSs converge to a single spot, accompanied by strong out-of-plane emission attributed to the onset of light localization. The spatially-localized modes were observed in a very similar configuration also in the real space, as was reported by N. Le Thomas in [116].

Fig. 5.4(a) plots the superimposed Fourier-space images recorded in the wavelength range 1473 - 1660 nm as compared to dispersion map calculated by plane wave expansion method. Position of the EFS recorded along the k_z axis and plotted versus the excitation frequency yields directly the dispersion relation along the Γ-K direction as shown in

Figure 5.4: (a) Experimentally measured dispersion map compared to the theoretical EFSs. (b) Dispersion curve along the Γ-K direction retrieved from (a).

Fig. 5.4(b). It can be witnessed that an excellent agreement between the experiment results and the theoretical calculations is achieved provided that the dispersion of the planar waveguide is taken into account.
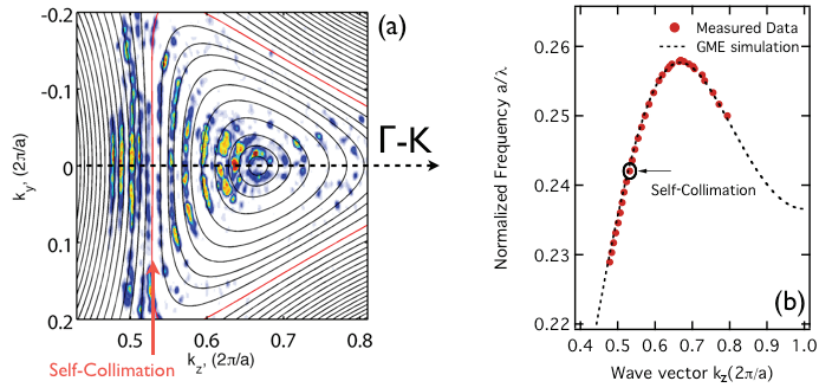
Chapter 6

Slow light in W1 waveguides in the presence of disorder

Slowing down the speed of light has been intensively studied within the past few years; it provides the possibility to control the speed of light for optical signal processing (optical buffers, delay lines) and at the same time, it enhances both linear and nonlinear light-matter interaction such as absorption, gain, thermo-optic and electro-optic interactions [57, 134, 135]. In photonic crystals, the slow light phenomenon is related to the multiple reflection and interference on periodic photonic crystal lattice, which leads to creation of *flat* photonic bands, *i.e.* bands which are characterized by group velocity considerably lower that in corresponding unstructured homogeneous medium.

As was already shown in the previous section, slow light can be observed at the band edges of a bulk photonic crystal, however, for practical applications, slow light line-defect waveguides are far more appealing:

- Optical waveguides can guide the slow optical signal without inherent propagation losses and within a large frequency bandwidth. In the case of bulk photonic crystal, reasonable transmission is achieved in the self-collimation regime, but such a regime has intrinsically a narrow bandwidth that principally does not coincide with the slow light operation.
- More degrees of freedom in the design of the waveguides. Dispersion curve of the line-defect waveguides can be engineered to create regions of flat, linear dispersion of the desired group index, within the largest possible bandwidth and lowest possible group velocity dispersion [58, 59, 136]. In contrast, the near-parabolic dispersion of bulk, perfectly periodic photonic crystals at the band edge is accompanied with large GVD, which hinders the advantage of operation in the slow light regime.

In the further text we will experimentally investigate the slow light propagation in W1 waveguides, mainly focusing on two aspects that are widely discussed in relation to the slow light propagation in photonic crystal environment: coupling into the slow light modes and limitation of the maximum achievable group index by disorder.

6.1 Coupling into slow light modes

Coupling between ridge access waveguides and photonic crystal slow-light modes is problematic firstly due to the difference of the transverse mode profiles of the fast and slow

light modes, and secondly, due to the difference in their energy density. While the first issue can be rather easily solved by adapting the access waveguide width and the exact photonic crystal termination, the latter is more fundamental. The difference in the energy density between fast and slow modes results from the fact that in the slow light regime the optical signal is spatially compressed and its intensity consequently increased proportionally to the slow-down factor S, defined as the ratio of the phase and the group velocity $S = v_\varphi / v_g$ [134]. In order to match the transverse field components at the interface, the energy flow in the slow light region must be lower than in the fast-light region, in other words, a large amount of energy must be reflected at the interface.

However, is has been shown that an efficient coupling between fast and slow modes can be achieved either by adiabatic transition, or at abrupt interfaces through significant contribution of the evanescent modes, which partially cancel the naturally large fields associated with the slow mode at the interface [137].
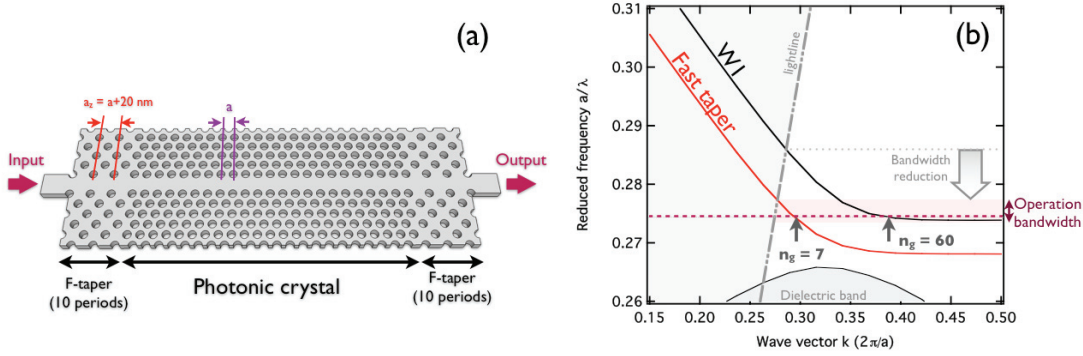
Figure 6.1: Schematic drawing of the Fast-light taper (F-taper).

Interface designs proposed to improve the coupling into the slow light line-defect waveguide modes include optimized hole termination [138], adiabatic tapering [139] and most recently, the so-called fast-light taper proposed by J. P. Hugonin *et. al.* [90] and experimentally realized by J. Li *et. al.* [58]. The latter consists of a *fast light* photonic crystal section approximately 10 periods long, inserted between the ridge waveguide and the photonic crystal waveguide. The lattice constant of the fast-light section is extended by 15-30 nm along the propagation direction, to effectively shift the dispersion curve of the PhC to lower energies and ensure the following coupling scheme: fast ridge waveguide mode → fast W1 mode → slow W1 mode, as schematically represented in Fig. 6.1(a). The fast-light taper introduces a new interface between the fast and slow mode, which favours the excitation of the relevant evanescent modes of appreciable amplitude and field profile, helping to satisfy the boundary condition [137, 140].

Dispersion curves of a standard W1 waveguide ($a = 420$ nm, $f = 36\%$) and fast-light taper section where the lattice constant a_z was increased by 20 nm are shown in Fig. 6.1(b). For the group index of the W1 equal to $n_g = 60$, the group index of the taper is $n_g = 7$, i.e., the taper still operates in the fast-light regime and efficient coupling between the access waveguides and the taper is expected. Below we provide an illustrative experimental proof that the fast-light section does indeed substantially improve the coupling into the slow modes.
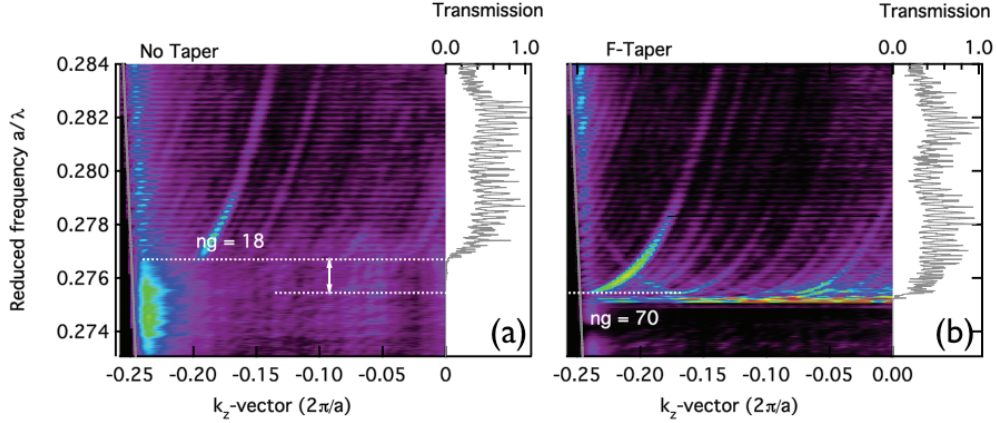
Figure 6.2: Comparison of experimental dispersion curves measured on a sample (a) without any taper, (b) containing a 10-period long F-taper section.

Fig. 6.2 shows the experimentally measured dispersion curves of two W1 waveguides, the first one with the standard interface, the second with an integrated fast-light taper as shown in the inset of the figure. Both samples were processed in a 220 nm thick Si membrane at the University of St. Andrews, with the nominal lattice constant $a = 426$ nm and filling factor $f = 36\%$. For the taper section, the lattice constant along the propagation direction z was increased to $a_z = 440$ nm.

The far-field signal shown in Fig. 6.2 originates from the scattering at the residual corrugation and surface roughness of the sample. As already mentioned in section 3.2.2, scattering of the guided mode at a given distribution of scatterers (*e.g.* one realization of disorder) results in a characteristic interference pattern, which follows the dispersion relation of the guided mode; this is exactly what we observe in Fig. 6.2. Nevertheless, two stronger lines can be distinguished, which are attributed to scattering at periodic residual corrugation of period 2.56 μm and can be used to reconstruct the full dispersion including the group index.
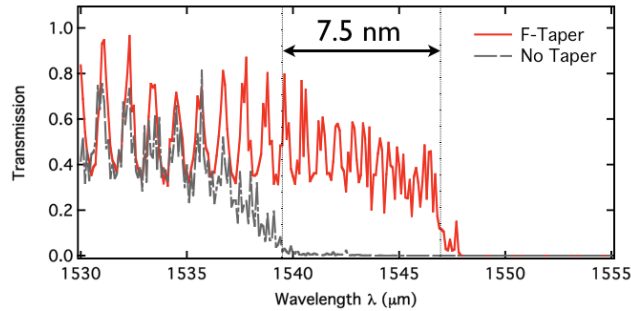
Figure 6.3: Increase in the spectral transmission bandwidth owing to the F-taper: Transmission through a sample with integrated F-taper (red) is compared to the standard access/photonic crystal waveguide interface (grey).

The striking difference between Fig. 6.2 (a) and (b) is the frequency at which the dispersion signatures including the residual grating lines disappear. For the waveguide with the standard interface, this occurs at the frequency $a/\lambda = 0.2767$ ($\lambda = 1539.5$ nm) which is well correlated with the loss of transmission plotted in the same figure. The maximum group index that can be deduced from the dispersion does not exceed the value $n_g = 18$. In contrast, when the fast light taper is used to couple into the W1 waveguide, both dispersion and transmission can be traced down to a close proximity of the theoretical W1 cutoff found at $a/\lambda = 0.2754$ ($\lambda = 1547$ nm). Hence, by adding the taper, the transmission bandwidth of the W1 waveguide is increased by 7.5 nm (Fig. 6.3), pushing the experimental group index value up to $n_g \approx 70$.

The example above shows a large improvement of the coupling performance when the fast-light taper is used, and in this context, the taper represents a guarantee of an efficient coupling down to the slow light regime until the light propagation gets hindered by the effects of disorder. However, systematic study on several W1 waveguides leads to observation that in certain cases an efficient coupling can be achieved even without the taper, which seems to largely depend on the specific realization of disorder inducing accidental resonances in the proximity of the access/photonic crystal waveguide interface.

Note further, that the use of fast-light taper reduces the operation bandwidth of the original W1 waveguide. Namely, in the frequency region just below the crossing of the W1 mode and the lightline (see Fig. 6.1(b)), the dispersion curve of the taper section is found within the light cone and, hence, the taper section suffers from out-of plane radiation loss. The larger the lattice constant difference Δa_z between the W1 and the taper, the more the operation bandwidth is reduced; in this context, optimum value of $\Delta a_z \approx 15\ nm$ should be chosen to allow for both efficient coupling into the slow-modes and at the same time only marginally affect the W1 performance in the fast-light regime.

6.2   Light transport regimes

An ideal W1 photonic crystal waveguide under TE-polarized excitation supports two guided modes, even and odd, which follow the theoretical dispersion presented in the introductory chapter in Fig. 1.14. For the even mode, such dispersion is roughly linear at higher frequencies with the group index of approximately $n_g = 5$, comparable with the index of ridge nanowire waveguides, while it becomes quasi-parabolic at the proximity of mode cutoff. In the latter region, the mode remains guided thanks to the photonic crystal band-gap effect and its dispersion is well defined until the mode cutoff where the n_g grows nominally to infinity. However, disorder that is always present in the real structures will eventually prevent the ballistic light propagation at high indices by inducing losses due to out-of-plane and back-scattering and, finally, light localization [141,142].

The modification of the ideal dispersion curve in the present of disorder has been discussed in detail the paper of N. Le Thomas et al. [141]) and is schematically illustrated in Fig. 6.4. Depending on a degree to which the light propagation is affected by disorder, we can distinguish three different regimes of light transport: dispersive, diffusive and the regime of light localization. As a criterion to assess the effect of disorder we choose the ratio of the sample length L and the so-called *mean free path l*, which gives the scale of exponential decay of the propagating wave due to disorder.
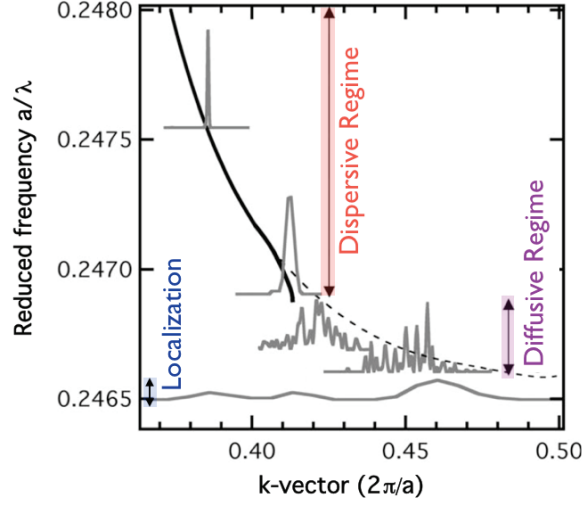
Figure 6.4: Illustration of a W1 dispersion in the presence of disorder.

Dispersive regime. In the dispersive regime the ratio $L/l << 1$, the sample length is much shorter than the attenuation length. This means that within the sample length the wave undergoes rare scattering events, its propagation is ballistic and the situation resembles the line propagation in ideal structure. In the dispersion diagram of the W1 such a regime is located far enough from the mode cutoff and is characterized by well-defined group velocity and dispersion line of vanishing linewidth, broadened only by the finite size of the guiding structure.

Diffusive regime. As the group index of the W1 mode increases, interaction of the light and matter increases accordingly, resulting in enhanced light scattering. Such disorder-induce scattering can be directed either out-of plane (scattering into radiative modes) or in the backward direction into the backward propagating mode, both leading to reduction of the attenuation length. At $L/l \approx 1$, the scattered intensity becomes comparable with the spatially coherent guided mode signal and we speak about the onset of diffusive regime. In the dispersion picture (Fig. 6.4), the dispersion curve broadens due to disorder induced scattering loss and related random spatial dephasing of the field. In such a regime neither the dispersion curve, nor the group velocity can be defined. Nevertheless, residual correlations within the partially coherent optical signal allow for the definition of energy transport velocity v_E [143], which may strongly deviate from unperturbed group velocity v_g, but can maintain rather efficient energy transport. Such regime is characterized by strong amplitude oscillations in the waveguide transmission spectrum as well as by formation of *necklace states*, *i.e.* partially-extended states that begin at the waveguide input and abruptly stop at a random position.

Regime of localized states. Finally, when the attenuation length becomes shorter than the actual length of the device $L/l > 1$, the regime of light localization takes place. It is characterized by the presence of sharp spectral signatures at and below the bottom of the theoretical mode cutoff. They originate from spatially localized states of localization

length shorter than the actual length of the sample, as evidenced by their dispersion that is largely extended along the k-axis. These states contribute to formation of the so-called Lifshitz tail [144], *i.e.* an extension of the density of states below the band edge of the regular unperturbed crystal [142], however, are not able to provide for transmission through the device.

First convincing experimental evidence of the three light transport regimes - dispersive, diffusive, and localization - is given in [141], where the light propagation in InP-based W1 waveguides was closely analyzed. Here we focus on W1 waveguides processed in a Silicon free-standing membrane. In contrast to [141], the investigated structures already include the fast-light taper, so that an efficient W1 mode excitation down to the slow light regime is guaranteed. Moreover, no additional grating probe was designed in the structure; we rely only on a residual corrugation grating present due to e-beam patterning, which provides us with sufficient optical signal to retrieve the dispersion curve. In this way, no additional leakage channel is present in the sample to smear the effect of disorder.

Let's first consider the structure introduced in the previous section, a standard W1 waveguide equipped with fast-light tapers, whose dispersion curve is shown in Fig. 6.2(b) and reproduced in a closer zoom in Fig. 6.5(a). The weak residual corrugation grating of period 2.56 μm folds the original dispersion curve into the lightcone, so that the 1st and the 2nd diffraction orders are visible as equally indicated in Fig. 6.5(a). The dispersion curve remains continuous and clearly resolvable down to the frequency of approximately $a/\lambda = 0.2754$, where the group index of 60-70 is achieved. Equally, the transmission along the full sample length (60 μm) does not decrease by more than 3dB. Within this frequency region the definition of the group velocity holds and W1 waveguide operates in the dispersive regime, although the portion of scattered, spatially incoherent light in the coherent signal increases, as evidenced by rising intensity of the background.

In the frequency region below classified as the diffusive regime, the original far-field pattern formed by two dispersion lines weakens, giving rise to new spectral features. One of them is depicted in Fig. 6.5(a) by an orange arrow. These features are correlated within a short frequency range, where they exhibit flat, nearly linear dispersion. Such a dispersion does not anymore follow the theoretical dispersion curve of the W1 waveguide, and leads to formation of the Lifshitz tail extending below the theoretical mode cutoff. However, note that the loss of spatial coherence and onset of the diffusive regime is not precisely correlated with the loss of transmission (see Fig. 6.5(a)). It confirms that light can be transported through the device even when the dispersion vanishes, and, hence, a careful distinction between group and energy transport velocity is required to determine the actual slow-down factor of a device when operating in the diffusive regime [141].

At the frequency $a/\lambda = 0.2754$, which roughly coincides with the theoretical cutoff of the W1, extended quasi-localized so-called necklace states, are formed. At discrete frequencies that are determined by the particular realization of disorder, weak coupling of such localized states is established, which leads to the apparition of narrow transmission peaks in otherwise strongly attenuated transmission spectrum as visible in Fig. 6.5(a). On the other hand, the extended states below that are depicted by blue arrows in Fig. 6.5(b) are truly localized, exhibiting no signature of transmission through the device.
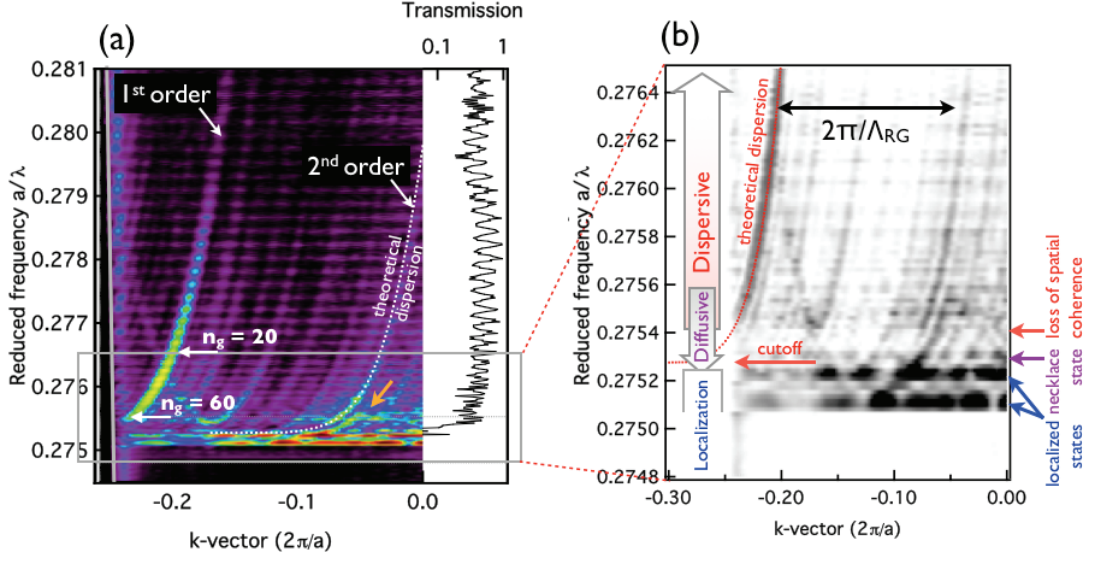
Figure 6.5: (a) Experimental dispersion and transmission of a W1 waveguide with integrated F-taper; red arrow depicts new spectral features attributed to the onset of the diffusive regime. (b) Detailed zoom of (a) in the proximity of the mode cutoff; spectral regions of dispersive, diffusive and localization regimes are assigned.

6.2.1 Scattering

The onset of the diffusive regime and localization is closely linked to enhanced out-of-plane scattering and back-scattering from disorder present in the sample [118, 142]. In photonic crystals, light may be scattered at sidewall roughness of the holes as well as at any deviation from perfectly periodic photonic crystal pattern, such as variations in the hole radius (size disorder) or in the hole position (position disorder). For instance, the position disorder in photonic crystals processed at EPFL yields standard deviation lesser than 1.3 nm, as results from a systematic study of high resolution SEM images [145]. In the fast light regime, *i.e.* for group indices around 5, such disorder does not cause important scattering and, hence, low propagation losses of 5-10 cm^{-1} can be achieved [146]. However, with increasing group index, the scattering probability and consequently the propagation loss increase dramatically, still limiting the use of slow light devices for practical applications.

Out-of-plane scattering. The fraction of the intensity scattered out of plane per unit length is expected to be proportional to the density of states, and hence, to the group index n_g [146]:

$$I^{out} \sim \gamma n_g \tag{6.1}$$

where the factor γ represents the overlap of the optical field with the scatterers, *i.e.* hole sidewalls in the photonic crystal environment, and may aslo depend on n_g.

The Fourier-space imaging technique allows us to observe such a linear dependence $I^{out} \propto n_g$ in experiment, as we show on the same dataset as presented in the previous section in Fig. 6.5. As already mentioned above, the intensity of light scattered out of plane, by both the random defects (background interference pattern) and the residual
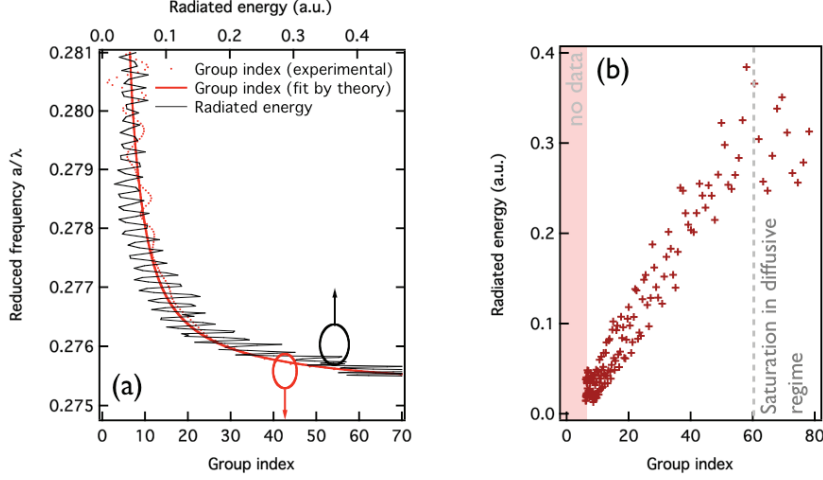
Figure 6.6: (a) Correlation of the out-of-plane scattering increase and the group index in the proximity of the mode cutoff. (b) Intensity of light scattered out of plane as a function of the group index.

gratings (dispersion lines), increases notably as the excitation frequency approaches the mode cutoff. This intensity, integrated along the k-axis and plotted versus frequency, is shown in Fig. 6.6(a), where it is compared to the measured group index. The intensity plot matches qualitatively well the increase of the group index, thus validating the linear scaling of the out-of-plane scattering with n_g.

Figure 6.6(b) plots directly the scattered intensity as a function of the theoretical group index; for this purpose, the scattered intensity in the *fast-light regime* was renormalized by transmission in order to remove spurious modulations in the collected signal, which are clearly related to variations in the coupling efficiency rather than to slow-light induced loss. The experimental points exhibit relatively large dispersion due to Fabry-Perot resonances, however, linear dependence $I^{out} \propto n_g$ is readily resolvable up to the group index of approx. 60, which is well correlated with the onset of the diffusive regime. Hence, the experimental data suggest that in a standard W1 waveguide operating in dispersive regime, the out-of-plane scattering loss scales linearly with n_g to a good approximation. For group indices larger than 60, saturation of the scattered signal is observed, which can be explained by gradual decrease of optical signal along the sample due to enhanced back-scattering.

Back-scattering In theory, the amount of back-scattered light is proportional to the density of states of both the forward and the backward propagating modes, and therefore it is scaled with n_g^2 [146–148]:

$$I^{back} \sim \gamma^2 n_g^2 \tag{6.2}$$

In reality, the n_g^2 dependence is affected by the Bloch mode shape included in the $\gamma(n_g)$ that rapidly changes and spreads into the photonic crystal in the slow light regime. Theoretical calculations performed on a standard W1 waveguide by S. Mazoyer et al. [118] show that a single exponent cannot be used to fit the dependence of the back-scattering loss on the group index; the loss exponent takes the value of 2 for large group indices ($n_g > 500$) and vanishingly small disorder (standard deviation of 0.02 nm), however, for $n_g < 40$ and disorder of 3 nm the exponent of almost 3.5 was found.
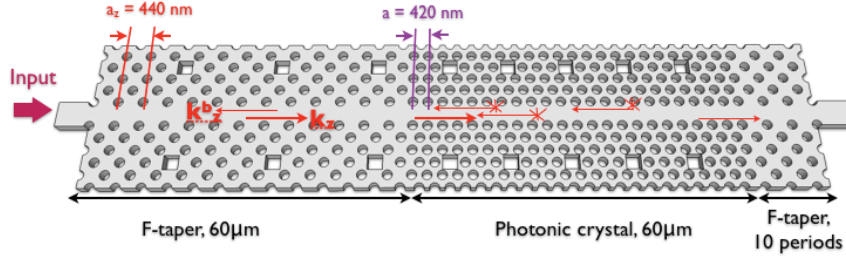
Figure 6.7: Schematic layout of sample designed for the back-scattering measurement.

The back-scattering in slow-light engineered waveguides was recently measured [132] using an interferometric technique similar to Low Optical Coherence Interferometry discussed in chapter 3, however, conclusive results with deeper physical argumentation have not (yet) been published. Here we use the Fourier-space imaging approach, taking the advantage of the fact that in Fourier space the forward and backward-propagated signal components can be spatially separated. For the purpose of backscattering measurement, we designed a sample shown in Fig. 6.7, which consist of 60 μm long fast-light taper section (F-taper, $a_z = 440$ nm), 60 μm long photonic crystal section (S-region, $a = 420$ nm, $f = 30\%$) and finally, a short output fast-light taper only 12-periods long to allow for efficient slow-fast light outcoupling. Linear probe grating is designed along the whole sample, and it consists of etched rectangular pillars of period $4a$, separated by 6 rows of holes from the W1 waveguide core. The sample was fabricated at the University of St. Andrews in a 220-nm-thick Si-air membrane.
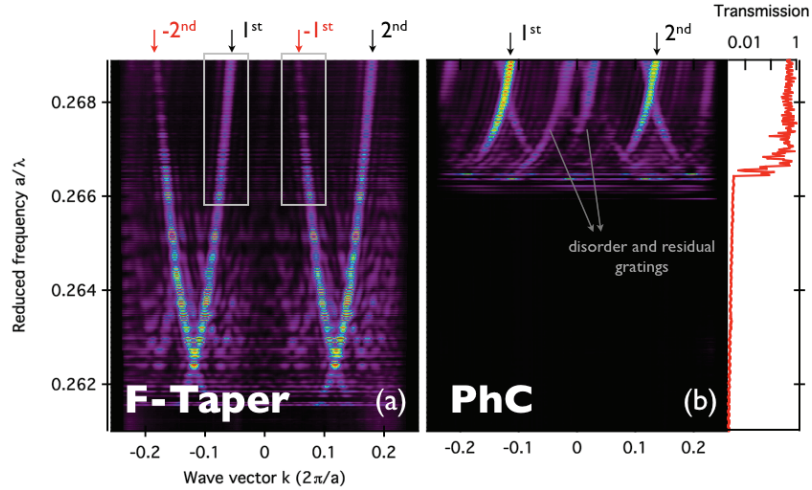
Figure 6.8: Dispersion curves of (a) F-taper section and (b) photonic crystal section measured by FSI. The back-scattering is measured by comparing the intensities of 1st and -1st diffraction orders in F-taper dispersion map, as indicated by grey rectangles.

The signal scattered at the probe grating allows us to determine the dispersion of the fast-light taper and photonic crystal itself, as shown in Fig. 6.8(a) and (b), respectively. Al-

though both sections are integrated within the same structure, separate dispersion curves can be obtained by careful spatial filtering in the real space; the possibility of characterization of different devices integrated on the same chip represents a distinct advantage of our characterization technique.

In both dispersion plots we can identify the first and the second diffraction orders of the probe grating folding the original dispersion into the light cone, as well as their back-reflections. The increase in the back-reflected signal measured as a function of frequency allows us to retrieve the spectral dependence of the back-scattering, and correlate it with the increase of the W1 group index.

However, this is possible only under the following assumptions:

The back-reflected signal is measured inside the F-taper region. Spatially incoherent back-scattered light inside the slow light S-section does not add coherently when scattered at the grating probes, and therefore it does not produce any increase in the back-reflected component. However, at the interface between the slow light and fast light region, the back-scattered signal is coupled into a dispersive eigenmode of the F-taper waveguide. The latter is spatially coherent and can be diffracted at the probe gratings, resulting in a well-defined line in the far-field.

Reflections are neglected. We assume that the reflections at all interfaces can be either neglected, or are spectrally independent, yielding back-reflection signal of a constant value. Such an assumption can be delicate as it is principally based on theoretical calculations [137] and is experimentally confirmed only up to the group index of approx. $n_g = 40$ [58].
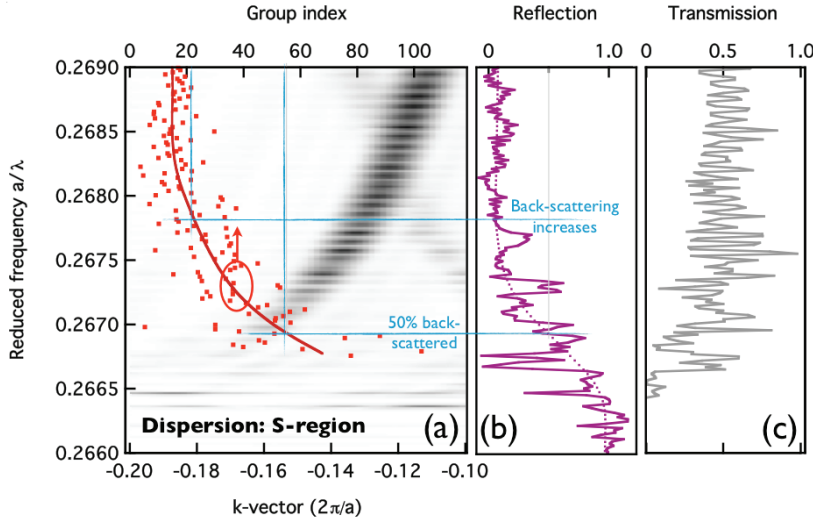
Figure 6.9: (a) Experimental dispersion curve and the group index of the photonic crystal "S" region. (b), (c) Spectral dependence of reflection due to back-scattering compared to the transmission spectrum. Correlations between the transmission increase and dips in reflection are clearly observed.

Fig. 6.9 shows the experimental dispersion curve of the photonic crystal S-region and the group index compared to the measured reflection and transmission spectra. As explained above, the reflection was measured in the F-taper region, namely by taking

the ratio of intensity diffracted at the probe gratings in the backward and the forward direction, respectively. In the fast-light regime and for reduced frequencies down to of approximately $a/\lambda = 0.2675$, the measured reflection remains constant at the mean value of approximately 23%. This value corresponds to the reflection at the output sample facet, is spectrally independent and was therefore subtracted from the measured data. Above $a/\lambda = 0.2679$ where the group index of the W1 waveguide reaches 20, a gradual increase of the reflection is observed, while at approx. $a/\lambda = 0.2675$, $n_g = 55$, one half of the intensity is back-reflected.

In such a condition, the transmission of the W1 waveguide as well as the light transport velocity is strongly influenced by the disorder, as is evidenced by strong oscillations in both reflection and transmission spectra. Note that local transmission increase is well correlated with the dips in reflection, which implies that it is indeed the back-reflection and not the out-of-plane scattering that is hindering the wave propagation, as was also demonstrated theoretically *e.g.* in [118].
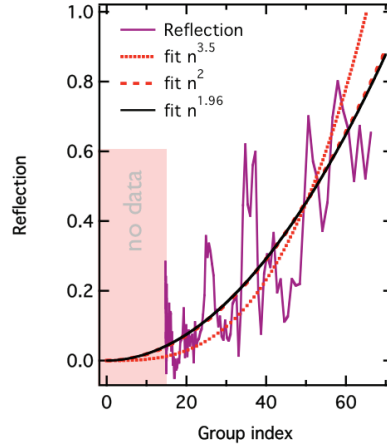
Figure 6.10: Back-reflection due to back-scattering plotted as a function of the group index.

The experimental reflection is plotted as a function of the group index in Fig. 6.10. Although the data are too noisy to make a definite conclusion about the $I^{back}(n_g)$ dependence, on can see that power dependence with the exponent between 2 and 3.5 (dotted red curves) matches reasonably well the experimental data. Direct fit of the experimental data for indices $20 < n_g < 60$ yields the value 1.96 ($\chi^2 = 1.36$, black line). The value surprisingly well matches the ideal $I^{back} \propto n_g{}^2$ dependence, but due to large spread of the experimental values the fit is not really statistically significant.

The experimental data presented in this chapter show that the Fourier space imaging in combination with residual or intentionally designed probe grating approach is a technique particularly well suited to study the light propagation in the presence of disorder. At the same time, substantial noise that is present in the data prevents us from making more general conclusions.

One part of this noise is caused by the disorder itself and is intrinsic, it cannot be eliminated, just smoothed out by averaging over several realizations of disorder. Such an averaging must be done on otherwise identical samples, processing of which is not a trivial

experimental task.

The second contribution of noise has its origin in insufficient signal to noise ratio between the signal scattered at the grating probes and the speckle-like background of far-field images. This issue can be solved by using volume probe gratings that probe the propagating modes efficiently independently on the mode profile. Finally, the Fabry-Perot resonances at the sample facets largely deteriorate the quality of the presented data. Antireflection coating deposition or utilization of more elaborate coupling schemes [16, 149] represent a straightforward solution and will be implemented in the future.

Chapter 7

Coupled-cavity waveguides

As an alternative to line-defect optical waveguides, photonic crystal coupled cavity-waveguides (CCW) [52,53] have recently generated a large interest in the field of slow-light engineering. Based on evanescently coupled optical resonators as schematically illustrated in Fig. 7.1(a), they can slow down the light propagation and at the same time, they exhibit essentially zero group velocity dispersion within a large part of their transmission bandwidth. The CCWs allow therefore for optical pulse retardation with negligible pulse distortion, which is highly desired in communication applications such as buffers or integrated optical delay lines. As an example, a pulse delay of 125 ps has been already experimentally demonstrated in a chain of 150 coupled cavities [21], proving that the CCW concept is eligible for practical use.
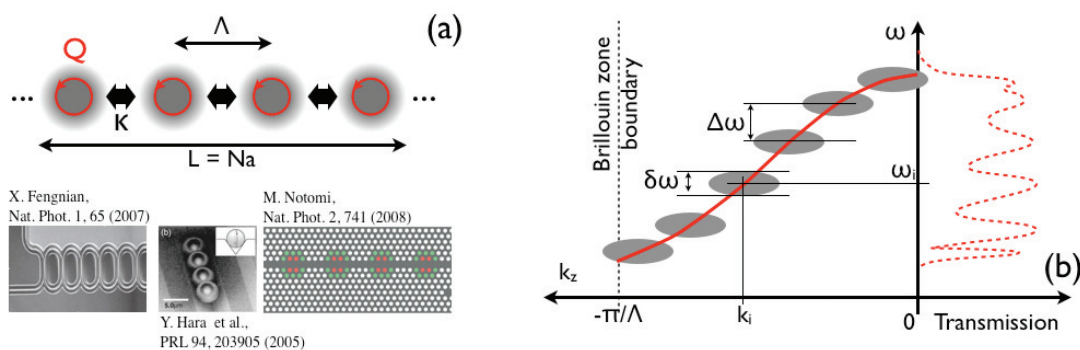
Figure 7.1: (a) Schematic drawing of a coupled resonator chain and three practical realizations using coupled ring resonators [150], microspheres [151] and high-Q photonic crystal cavities [21]. (b) Dispersion curve of an infinite (red line) and finite (grey ellipses) coupled-cavity waveguide as given by the Tight-binding model. Anticipated transmission for the finite CCW case is depicted at the right.

Coupled-cavity waveguides reported up to date include structures formed by concatenated nanowire microrings [150], microsphere resonators [151], coupled nanopillars [152], and last but not least, photonic crystal microcavities of different sizes and designs [21, 153, 154]. In this chapter, we will focus on two examples: photonic crystal L3-based coupled cavity waveguides separated by one hole in the barrier (Fig. 7.2(a)) and heterostructure cavities (Fig. 7.2(b)), which are based on W1 photonic crystal waveguide with locally reduced lattice constant. The FSI technique was used to probe the dispersion

properties of both structures, and the experimental results allow us to illustrate the formation of the CCW mode as well as to discuss the limitations of the coupled-cavity structures related to their finite size, radiation loss and residual disorder.
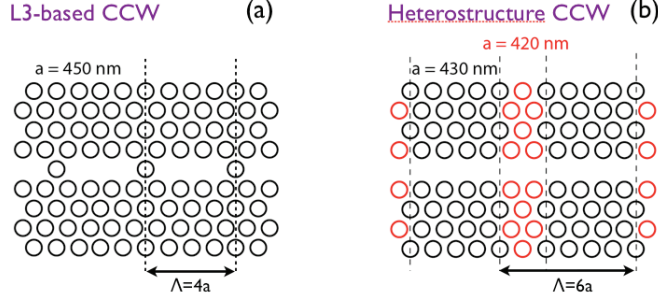
Figure 7.2: Schematic of an L3-based CCW (a) and a heterostructure photonic crystals CCW (b).

7.1 L3 Coupled-Cavity Waveguides

7.1.1 Formation of the coupled-cavity mode: Tight-binding approach

A general chain of coupled optical resonators is depicted in Fig. 7.1(a), where Λ denotes the period, Q_i the quality factor of an isolated cavity and κ the coupling constant. The dispersion of such a chain of coupled resonators can be conveniently modeled by the Tight Binding Approximation (TBA), which is well known in solid state physics to describe the formation of electronic bands [33]. In most PhC CCW structures, the cavity separation is large enough so that coupling to the first neighbor is sufficient to yield the dispersion curve, which is takes the well-known form [33, 52, 155]:

$$\omega = \omega_0 + \frac{S + 2T\cos(k\Lambda)}{1 + 2R\cos(k\Lambda)} \approx \omega_0 + \kappa\cos(k\Lambda) \tag{7.1}$$

where S, T, R are the *shift, overlap and transfer* integrals defined in [155], k is the wavenumber, ω the frequency, ω_0 the resonance frequency of the isolated cavity and κ is the coupling constant, *i.e.* the measure of mutual interactions between the cavities. As illustrated in in Fig. 7.1(b), the dispersion curve has a sinusoidal shape, with period determined by the CCW periodicity Λ and amplitude given by the coupling constant κ. The coupling constant κ can be expressed as [52, 156]:

$$\kappa = \int \left[\epsilon_0\left(\mathbf{r} - \mathbf{\Lambda}\right) - \epsilon\left(\mathbf{r} - \mathbf{\Lambda}\right)\right] \times \mathbf{E}_0(\mathbf{r})\mathbf{E}_0(\mathbf{r} - \mathbf{\Lambda})d^3\mathbf{r} \tag{7.2}$$

and, hence, it depends on the field overlap between neighboring cavities. For a given periodicity Λ, an increase in the mutual coupling leads to an increase of the bandwidth an the slope of the dispersion curve, and, consequently, a drop in the group velocity of the guided light. On the contrary, if the cavities are well separated and weakly coupled, narrow, flat CCW dispersion curve with a large group index is created. For slow light applications, the operating point of interest is the inflection point at $\omega = \omega_0$. Although the

group velocity $v_g = \kappa\Lambda$ is maximum at this point, the group velocity dispersion vanishes and dispersion can be considered linear to a good approximation.

For chains of finite length of N cavities, the dispersion curve is sampled into N states with a constant spacing in k (Fig. 7.1(b)):

$$\omega_i \approx \omega_0 + \kappa\cos(k_i\Lambda), \qquad k_i = \frac{\pi i}{(N+1)\Lambda}, \quad i \in [1..N] \qquad (7.3)$$

The scaling of k_i by factor $N+1$ results from truncation of the infinite TBA problem into a matrix equation of finite dimensions (linear boundary condition), in contrast to scaling by N for infinite or periodic structures (periodic, or Born - Von Karman boundary condition) [156]. Such a scaling can be intuitively explained by comparing the coupled cavity waveguide modes to vibrations of a one-dimensional line of atoms of separation R, where the 0th and $(N+1)^{\text{th}}$ atoms are fixed, and, hence, have zero amplitude [33]. Each vibrational mode of such a chain has the form of a standing wave:

$$u_i = u_0\exp(-i\omega_k t)\sin(ikR) \qquad (7.4)$$

with boundary conditions:

$$u_0 = 0$$
$$u_{N+1} = 0 \quad \Rightarrow \quad \sin((N+1)kR) = 0,$$

which samples the wave vector values k_i into $\frac{\pi}{(N+1)R}, \frac{2\pi}{(N+1)R}, ... \frac{\pi}{R}$. The rigorous mathematical derivation for the electromagnetic case of coupled cavities is given *e.g.* in [157].

If the linewidth of individual energy states ($\delta\omega$) is narrower than the energy spacing between the states, the dispersion curve will consist of N isolated points and the optical transmission shall exhibit N well-separated sharp peaks. This occurs when the cavity number is small in respect to the cavity quality factor, Q, like *e.g.* in the work of Notomi et al. [21], where a finite chain of high intrinsic Q cavities ($Q_i > 10^5$) was discussed. In such a regime, an input pulse of bandwidth $\Delta\omega$, is transformed into its convolution with discrete transmission spectrum of the CCW, and it is slowed down at the expense of distortion of its temporal envelope. Such distortion includes generation of residual pulse echoes and possibly the envelope broadening if the transmission peaks are not strictly equidistant or do not cover the full bandwidth of the pulse.

In the other case, *i.e.* if $\delta\omega \geq \Delta\omega$, the dispersion curve of the CCW is expected to be smooth and continuous and a transmission band is formed. Creation of such a band is essential for practical applications, as the optical signal can propagate without distortion only if all its spectral components are equally transmitted. Using elementary algebra, we can rewrite the continuity condition $\delta\omega \geq \Delta\omega$ using the Q-factor Q_i of individual waveguide modes:

$$\delta\omega = \frac{\omega}{Q_i} \quad > \quad \Delta\omega = \frac{c\Delta k}{n_g} = \frac{c\pi}{(N+1)\Lambda n_g} \qquad (7.5)$$

$$Q_i \quad < \quad 2(N+1)n_g\frac{\Lambda}{\lambda} \qquad (7.6)$$

As a first approximation we will consider the quality factor constant and equal to the isolated cavity quality factor Q. Such an approximation is exact for cavity constituents

whose quality factor is not limited by the out-of-plane radiation, like it would be for coupled micro-ring resonators, or for a cavities with uniform emission profile as discussed later in this chapter. In this case, the condition Eq. (7.6) is a restatement of the intuitive argument that the higher the Q, the more cavities need to be coupled to achieve continuous dispersion. However, the photonic crystal coupled cavities considered in this work are limited by out-of-plane losses and as a result, the Q_i changes depending on the location of the mode wavevector within the Brillouin zone as will be discussed later in this chapter. In this case, Eq. 7.6 applies with i being the index of the mode with the largest Q-factor.
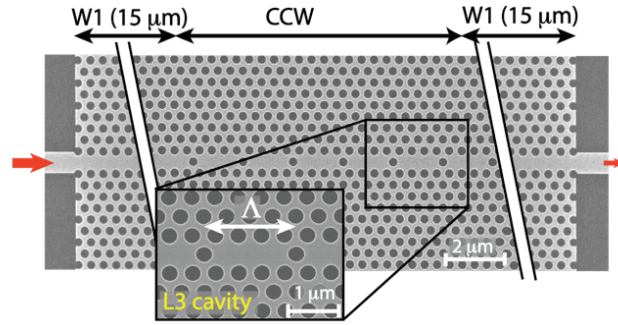
Figure 7.3: Top-view SEM image of an L3-based CCW including the coupling scheme.

Using the Fourier-space imaging, we are able to illustrate in experiment the formation of the CCW mode as well as the transition from discrete to continuous dispersion curve upon increasing the number of cavities in the chain. The structures under consideration consist of N = 1, 3, 6, 10 and 20 concatenated cavities in a triangular photonic crystal lattice. As can be seen in Fig. 7.3, each cavity is formed by removing three holes along the Γ-K direction and is separated from the neighboring ones by one adjacent hole. The presented data were measured on three different L3-CCW samples, all fabricated using the facilities at EPFL:

- Low-Q CCW (Q∼1000), 330-nm thick SOI with lattice constant $a = 420$ nm and the filling factor $f = 0.38$

- Moderate-Q CCW 1 (Q∼4800), 220-nm thick Si air-bridge membrane, $a = 450$ nm and $f = 0.36$

- Moderate-Q CCW 2 (Q∼5200), 220-nm thick Si air-bridge membrane, $a = 440$ nm and $f = 0.45$

As also shown in Fig. 7.3, the coupled-cavity chain was excited through an adiabatically tapered access waveguide and photonic crystal W1 waveguide in a so-called in-line configuration, which typically allows for high transmission through the resonator chain [21].

The theoretical dispersion diagram of such a waveguide calculated by GME is shown in Fig. 7.4(a) with the fundamental CCW mode shown in red. The latter is well separated from both the dielectric band shown in grey as well as from higher order coupled-cavity waveguide modes appearing at frequencies higher than $a/\lambda = 0.28$. Such a separation validates the assumption that the L3 cavity mode is an isolated, nondegenerate state, which

is one prerequisite for using the TBA theory to simulate the CCW dispersion. Hence, in agreement with the TBA result, the mode is characterized by flat and sinusoidal dispersion curve of bandwidth of approximately 8 nm and group index value $n_g \approx 50$ at the inflection point. The higher order CCW modes are out of interest as they are either not excited due to their odd symmetry, or they are extremely lossy due to low intrinsic quality factor of the higher order L3 cavity modes.
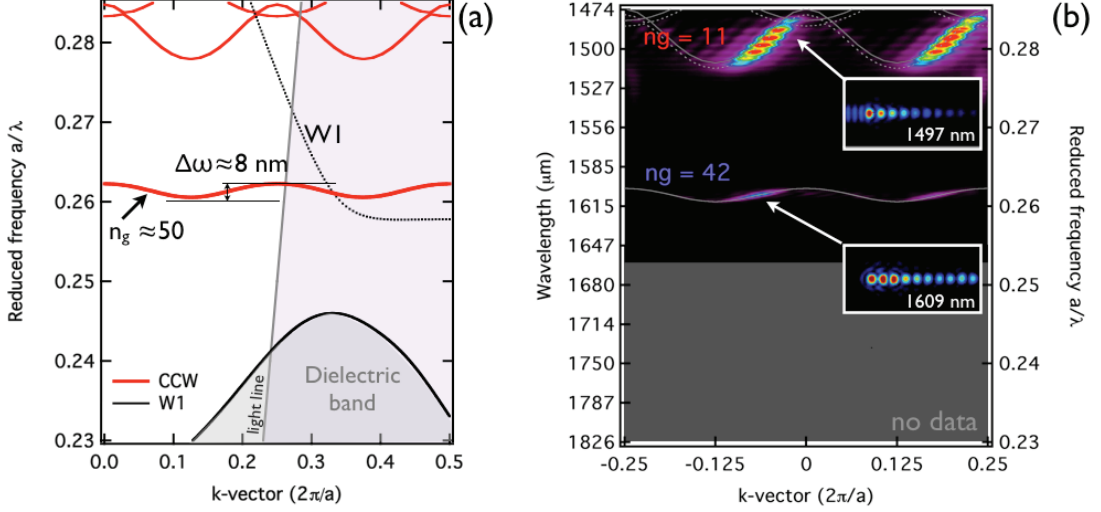
Figure 7.4: Theoretical (a) and experimental (b) dispersion of a the L3-based CCW with one hole in the barriers. The latter was measured on a Low-Q CCW sample based on SOI.

As can be seen in the figure, the first two Brillouin zones of the coupled-cavity waveguide fall into the light cone, which means that the CCW mode has leaky Bloch mode components. These two Bloch mode components constitute channels through which the mode energy can radiate out of plane. In consequence, unlike in typical low-loss optical waveguides which support truly guided modes, the coupled-cavity waveguides are inherently lossy. Although detrimental for energy performance, this permits us to study the light propagation within the structure by means of Fourier-space imaging and without the need of using additional near-field probes. Full experimental dispersion map of the Low-Q CCW sample measured in the same frequency range as the GME calculations is shown in Fig. 7.4(b), proving a good agreement between the experiment and the theoretical simulation. The insets show the comparison of the near-field pattern of the fast exponential decaying second order mode and the fundamental mode of interest.

Fig. 7.5(a)-(c) shows the experimentally measured dispersion diagrams for Moderate-Q CCW 2 samples when increasing the numbers of cavities from N = 3 to 6 and 10. The inter-cavity coupling strength defined by one hole in the barrier results in a bandwidth $\Delta\omega = \Delta(a/\lambda) = 0.0015$, which corresponds to approximately 8 nm. In agreement with the TBA for finite cavity chains, the dispersion is formed by resonances modes whose spectral position follows the underlying theoretical sinusoidal dispersion. Nevertheless, note that unlike predicted by theory, the spacing of the resonance waveguide modes is not strictly equidistant in k as demonstrated in Fig. 7.5(b) where both the experimental data and the
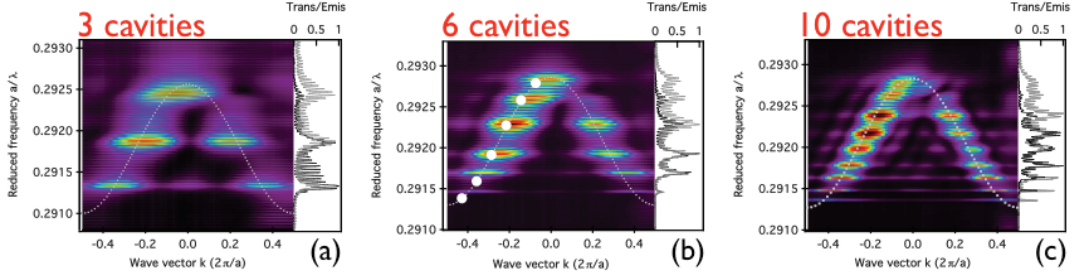
Figure 7.5: Formation of CCW dispersion when increasing the number of cavities N from 3 (a) to 6 (b) and 10 (c); transmission and out-of-plane emission measured for all structures is shown in black and grey, respectively. (b) equally shows the discrepancy between the position of experimental and ideal resonant peaks (white dots) that assume equidistant sampling in k.

theoretical position of the modes given by Eq. 7.3 are shown. Such violation of equidistant spacing is primarily due to the way how the CCW is terminated. The coupling into the CCW mode is realized through access waveguides, which modify the field distribution of the adjacent cavities and hence, the cavities in the CCW chain are not anymore strictly identical as assumed by the TBA approach. Moreover, the field distribution of the cavity chain changes along the dispersion curve, resulting in variations of the effective penetration length of the CCW resonance modes. As a result, nor linear, neither periodic boundary conditions can be applied and the k_i spacing becomes dependent on the frequency and the specific CCW termination. The larger the numbers of coupled cavities, the weaker is the effect of the CCW terminantion. For large N, the majority of the cavities can be considered equivalent and the change of the penetration length in respect to the full length of the device becomes negligible, and the linear boundary condition holds to a good approximation.

The sampling into discrete resonance modes along the CCW dispersion curve is also altered by inherent radiation loss of the CCW, which is generally not taken into account in the TBA model. Resonant modes with extremely low Q_i decay rapidly along the CCW chain, exciting only a fraction of the cavities. In consequence, the Q-broadening due to out-of plane loss becomes larger that the spacing between the CCW modes and the individual resonance modes cannot be resolved anymore. This is illustrated in Fig. 7.5(c) where only 8-9 resonances can be discriminated although the full CCW chain comprises 10 cavities.

To sum up, in short coupled-cavity waveguides, or waveguides characterized by excessive loss within (a part of) the CCW spectral bandwidth, the assumption of equidistant spacing in k between discrete resonant modes is not justified. Hence, the correct shape of dispersion curve cannot be reconstructed by simple transmission measurement, where the spectral position of the discrete transmission peaks is plotted on a regular k_i-grid. Though, such an approach is used in [21], and therefore the precision in retrieved group indices in particular for a small number of coupled cavities might be debatable.

7.1.2   Radiation losses

Taking as example the dispersion diagram shown in Fig. 7.5(c), one can notice that the Q-factors of individual CCW resonant modes change dramatically along the dispersion curve.

As illustrated in Fig. 7.6(a), the spectral profile of each individual peak allows us to directly determine the quality factors Q_i, which, plotted versus ω_i, yield the spectral dependence $Q(\omega)$ equally shown in Fig. 7.6(b). While the Q-factor at the top of the transmission band hardly exceeds the value of 1800, it gradually increases towards the bottom edge of the transmission band, reaching $Q > 28000$, which is a value approx. six times higher than the intrinsic quality factor $Q \sim 5200$ of individual cavity constituents. The latter was determined from the emission spectrum of an isolated reference L3 cavity of identical parameters as shown in the inset of Fig. 7.6(b).
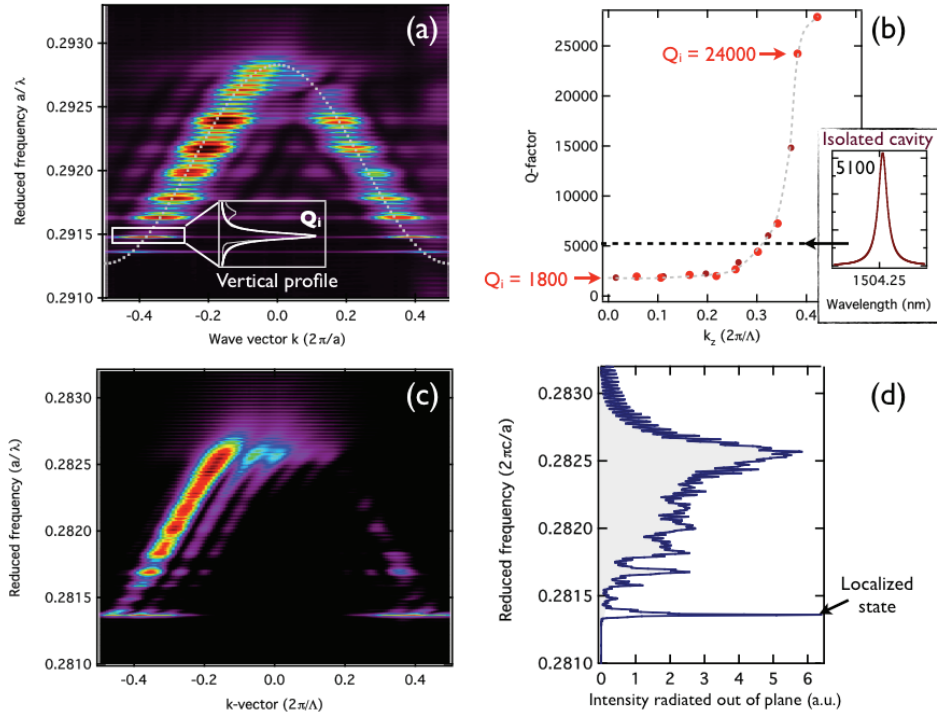
Figure 7.6: Change of radiation losses along the dispersion curve for both the discrete ($N = 10$) and continuous ($N = 20$) case of dispersion measured for moderate-Q Si-membrane structures. (a), (b) illustrate how the Q-factor of CCW resonant modes increases from the Γ point towards the Brioullin zone boundary. The resonance peak of an isolated L3 cavity that gives the quality factor of approx. 5100 is shown in the inset. (c), (d) demonstrates that in the case of continuous dispersion the out-of-plane emission yield decreases towards the Brillouin zone boundary in agreement with (b).

Similar effect of frequency-dependent radiation loss can be observed on the dispersion diagram presented in Fig. 7.6(c) and (d), which appertain to a sample consisting of 20 coupled cavities (sample Moderate-Q CCW 1). As witnessed in the figure, concatenating $N = 20$ cavities with intrinsic Q of 4800 is already enough to achieve a smooth dispersion curve with the exception of the very bottom part of the CCW bandwidth. In analogy with the previous example, even in the case of a smooth dispersion curve the radiated intensity and, hence, the propagation loss of the CCW reaches maximum close to the top of the dispersion band and diminish in the direction towards the 1$^{\text{st}}$ Brillouin zone (BZ) boundary, were the out-of plane radiation is almost completely suppressed.

Such experimental observations are in agreement with the recent theoretical work [158, 159], which has shown that the CCW radiation loss primarily depends on the quality-factor of a single cavity, but may vary substantially by several orders of magnitude along the dispersion curve. The physical origin of this variation can be partially explained by the light-line argument, *i.e.* the optical loss increases with the number of Bloch mode components lying in the light cone. However, this approach provides only an incomplete insight into the problematic and fails to explain the fine $Q(k)$ variations predicted by more rigorous theoretical calculations [158]. Here we demonstrate that along with the number of Bloch modes lying inside the light cone, it is mainly the radiation pattern of an isolated constituent cavity that determines the magnitude and the frequency dependence of the CCW radiation loss. As we show below, such pattern defines an envelope function that modulates the entire emission spectrum of the coupled-cavity waveguide.

The origin of the radiation loss of coupled-cavity waveguides can be understood in terms of finite lifetime of the confined electromagnetic mode of the constituent cavities. Indeed, optical cavities fabricated in two-dimensional photonic crystal slabs are inherently lossy; Although they can well confine the electromagnetic field in-plane by virtue of the photonic band-gap effect, vertical confinement by total internal reflection is incomplete and the energy can leak out of the cavity, resulting in out-of-plane radiation losses. It has been shown [160, 161], that the total radiated power from an isolated cavity is related to the Fourier Transform (FT) of the electromagnetic field at the slab interface, and can be expressed as an integral over all spatial components of this field that are found within the light cone:

$$P^{SC}(k_y, k_z) \propto \int_{k<w/c} \left| E^{SC}(k_y, k_z) \right|^2 d\mathbf{k} = \int_{k<w/c} \left| \text{FT}\left(E^{SC}(r_y, r_z) \right) \right|^2 d\mathbf{k} \qquad (7.7)$$

Here ω stands for the resonant frequency of the cavity, $E^{SC}(r_y, r_z)$ is the cavity near-field profile and c the speed of light. A similar approach can be used to calculate the radiation loss of the coupled-cavity waveguides. We assume a finite CCW that consists of N cavities concatenated along the r_z axis, separated by a distance Λ. Within the tight binding approximation, we can express the near-field pattern of the CCW as a linear combination of the eigenmodes $E^{SC}(r_y, r_z)$ of individual cavities [52]:

$$E_\omega(r_y, r_z) = \sum_{n=-N/2}^{N/2} E^{SC}(r_y, r_z - n\Lambda) \mathrm{e}^{-ik(\omega)\Lambda n} \qquad (7.8)$$

Such near-field distribution is an explicit function of the mode propagation constant $k(\omega)$, and it varies significantly with frequency owing to the strong dispersion of the CCW slow mode. By performing the Fourier transform of eq. 7.8, we obtain the far-field pattern of the CCW:

$$E_\omega(k_y, k_z) = E^{SC}(k_y, k_z) \times N \sum_{n=-\infty}^{\infty} \text{sinc}\left[\frac{N\Lambda}{2\pi} \left(k_z - k(\omega) - \frac{2\pi n}{\Lambda} \right) \right] \qquad (7.9)$$

Radiation loss of the CCW can be evaluated in the same way as in Eq. 7.7, *i.e.* by integrating $E_{\omega_i}(k_y, k_z)$ over all spatial components of the CCW far-field pattern that lie below the light line.
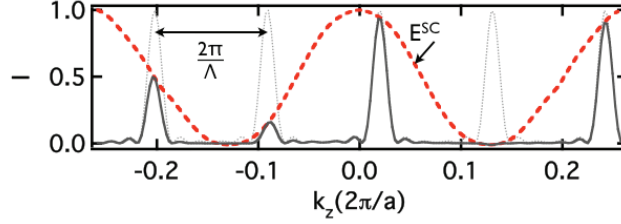
Figure 7.7: Theoretical one-dimensional far-field spectrum (blue) of CCW with $\Lambda = 9a$, $N = 20$ and $k_0 = 0.02(2\pi/a)$. Single cavity far-field pattern (red) that forms the envelope function of the CCW spectrum is also shown.

Let's focus on the theoretical far-field pattern given by eq. 7.9. An example of such pattern for a CCW formed by $N = 20$ cavities with a periodicity $\Lambda = 9$ a is shown in Fig. 7.7. It is formed by an infinite series of peaks, which are equidistantly spaced along the k_z axis and separated by the reciprocal vector of the coupled cavity chain $\mathbf{G} = 2\pi/\Lambda$. The discrete nature of the far-field pattern is a consequence of far-field interference between individual cavities, and it has the same physical origin as diffraction beams of an optical grating or highly directional emission of periodic antenna arrays [162]. Since the coupled-cavity chain is limited in length, each of the peaks is further broadened by a sinc-profile with line-width inversely proportional to the total length of the structure $L = N\Lambda$. In the limit of $N \to \infty$, *i.e.* for an infinitely long structure, the far-field pattern converges to a comb of delta-functions $\sum_{n=-\infty}^{\infty} \delta(k_z - k(\omega - 2\pi n/\Lambda))$. Finally, the amplitude of individual peaks is multiplied by the emission pattern of an isolated cavity $E^{Sc}(k_z)$, which plays the role of envelope function modulating the whole CCW emission spectrum. Note that according to eq. 7.9, the CCW mode can freely radiate only at those k-vectors at which the constituent cavities radiate; if an isolated cavity does not emit at a given wave-vector k_z, no radiation occurs in this direction neither for the periodic arrangement of cavities. In consequence, any structure of the single-cavity far-field pattern result in a variation in the emission yield, and, hence, the CCW loss along the dispersion curve.

Fig. 7.8 (a) and (c) show the measured experimental far-field pattern of an isolated L3 cavity and a CCW as well as their k_z profiles (b) compared to the experimentally measured quasi-continuous dispersion curve (d). In agreement with the theoretical model presented above, the far-field spectrum of the coupled-cavity waveguide is discrete, formed by two narrow peaks separated by a distance $2\pi/\Lambda$. The absolute position of the spectral lines is determined by the propagation constant of the CCW mode k, which depends on the frequency of excitation ω. When the excitation frequency is tuned, the spectral lines move along the k_z axis following the dispersion relation and at the same time a gradual change of their intensity is observed. The radiated intensity decreases with decreasing frequency (*i.e.* in the direction towards the 1$^{\text{st}}$ Brillouin zone (BZ) boundary) were it is almost completely suppressed. This is a direct consequence of modulation of the CCW far-field spectrum by the emission profile of an isolated cavity: referring back to Fig. 7.8(a), the isolated cavity pattern also exhibits a clear maximum at the Γ point and decreases along the k_z axis towards distinct minima at approximately $k_z/(2\pi/a) = \pm 0.125$, which coincide with the BZ boundary of the coupled-cavity chain.
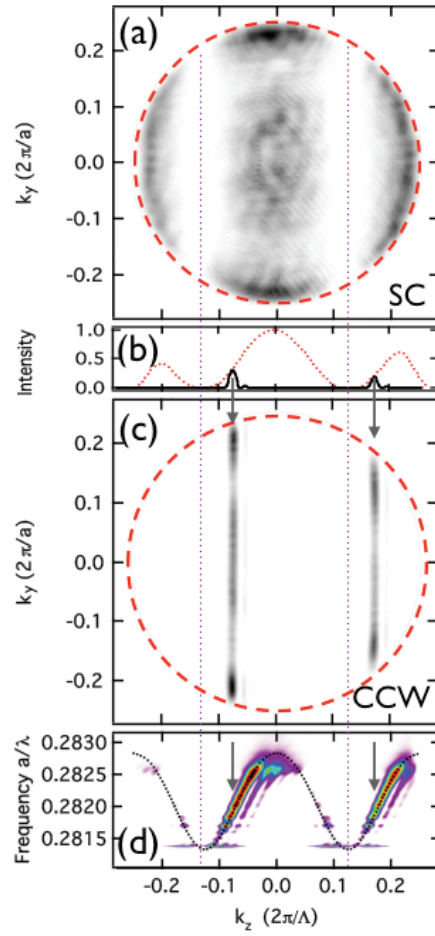
Figure 7.8: (a) and (c): Experimentally measured far-field spectrum of an isolated L3 cavity and a CCW formed by 20 cavities, respectively. (b) one-dimensional intensity profiles of (a) and (c) at $k_y = 0$. (d) Dispersion curve of the CCW mode.

7.1.3   CCW dispersion in the presence of radiation loss and disorder

Strong variation of the optical loss along the dispersion curve has several consequences on the coupled-cavity device operation. Primarily, it dramatically reduces the transmission bandwidth of the CCW. Figure 7.9 shows the previous example of the dispersion curve measured for 20 coupled cavities (sample Moderate-Q CCW 1) plotted together with the transmission spectrum and the real-space decay of light propagating along the coupled-cavity chain. The latter was obtained by integrating the measured real-space profile along r_y direction and plotting it as a function of wavelength. As illustrated in the figure, we can distinguish several transmission regimes:
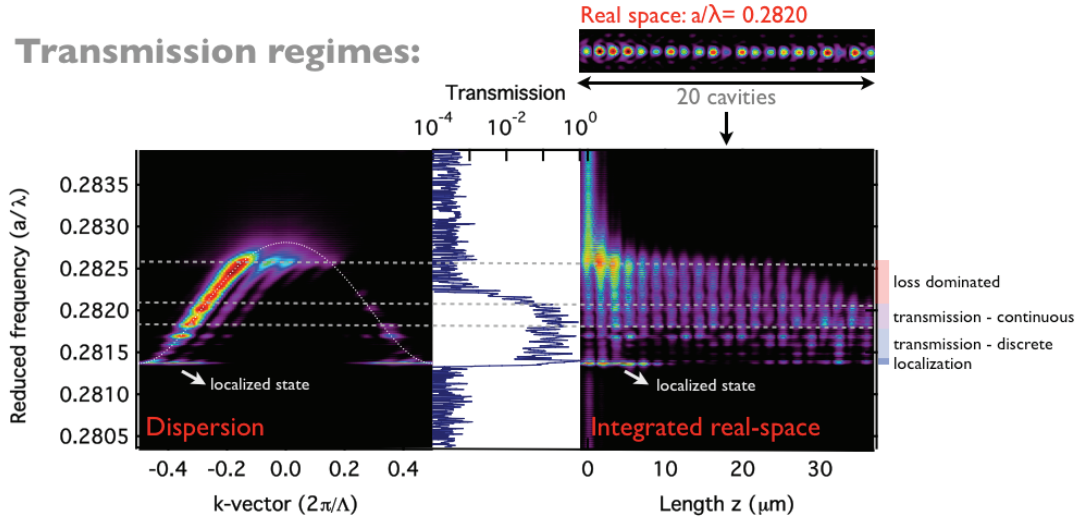
Figure 7.9: Dispersion curve, transmission and integrated real-space top-view images of a CCW plotted vs the frequency. The regime dominated by radiation loss, continuous and discrete transmission regimes and the regime of localization can be distinguished.

- Regime dominated by radiation loss. The mode decays rapidly along the propagation direction and practically all optical signal is radiated out of plane before reaching the output access waveguide. The transmission through the sample is completely hindered by excessive radiation loss. Referring to Fig. 7.6(b), the corresponding waveguide quality factors Q_i are of the order of 2000 and lower.

- Regime of continuous transmission. A narrow spectral regime where high transmission through the CCW sample is achieved and at the same time the condition of continuous transmission Eq. (7.6) is fulfilled. According to this condition, the waveguide quality factor Q_i is of the order of 2500, which is roughly one half of the intrinsic Q of an isolated L3 cavity.

- Regime of discrete transmission. Increase of Q_i associated with the diminution of the radiation loss at the proximity of the Brillouin zone boundary results in the fact that the condition Eq. (7.6) is no longer fulfilled and a gradual transition from continuous to discrete transmission regime is observed.

- Regime of localized states. Similarly as for W1 line-defect waveguides discussed in the previous chapter, increased group index at the band edge in the presence of residual disorder finally prevents the ballistic signal propagation, leading to an onset of the diffusive regime and localization. This is manifested by overall decrease of transmission as well as localized or necklace states that start at the waveguide input and stop at a random position along the sample length. Such a localized state can be observed in Fig. 7.9, both in real space as well as in Fourier-space as a line distinctively broadened along the k_z direction.

In summary, due to spectral variation of the optical loss in L3 CCWs, only the bottom half of the full CCW bandwidth can be transmitted along the coupled-cavity chain, while only 20% of the full bandwidth exhibits flat, continuous transmission. We stress that this conclusion is valid only for the L3 cavity design and low periodicity of the coupled cavity chain, *i.e.* $\Lambda = 4a$. For practical applications, the radiation profile of the constituent cavities and the periodicity of the CCW must be optimized so that within a specified frequency range the wave vectors of the CCW modes take values at which the single cavity does not radiate. Ideally, if the full bandwidth of the CCW mode is to be used, the emission profile of a single cavity has to be homogenized in order to suppress the variations of the waveguide quality factor and reduce the integral propagation loss below a desired level.

Another detrimental effect of the out-of-plane radiation loss is the renormalization, *i.e.* change of the shape of dispersion curve in the regime of slow light propagation, and consequent limitation of the maximum achievable group index. This is illustrated in Fig. 7.10, where the experimental dispersion is compared to the theoretical dispersion curve obtained from the tight-binding model. At the top of the dispersion band where the radiation loss dominates, the theoretical group index $n_g = \mathrm{d}k/\mathrm{d}\omega$ diverges to infinity while the experimental group index is limited to a finite value $n_g = 80$, yielding a clear discrepancy between the theory and experiment. At the bottom of the dispersion band of the moderate-Q sample where the losses become negligible, group index can achieve much higher values up to 180 before the light transport gets hindered by structural disorder and related light localization. Renormalization of the dispersion curve due to disorder is more closely discussed in *e.g.* [113, 142, 143]. Since the main application of the CCW structures is expected in slow-light engineering, it is important to understand that suppressing the CCW radiation loss simultaneously pushes the limit of possible light speed reduction.

7.2   Heterostructure CCW

7.2.1   Mode formation: perturbative approach

The coupled-cavity structure considered in this section is shown in Fig. 7.11. It is based on a standard photonic crystal single-line-defect waveguide (W1), the lattice constant of which is periodically decreased in the propagation direction by 10 nm to create a double heterostructure as originally proposed by B-S. Song *et. al.* [163]. More specifically, the optical cavities are formed by four successive periods of lattice constant $a = 430$ nm and they are separated by potential barriers consisting of two periods of $a_b = 420$ nm (highlighted by red in Fig. 7.11). Hole diameter of $d = 286$ nm is constant in the whole photonic crystal, corresponding to the filling factor of $f = 40\%$ in the cavities. The total length of the investigated CCW is 25.8 μm and it comprises 8 cavities, which are
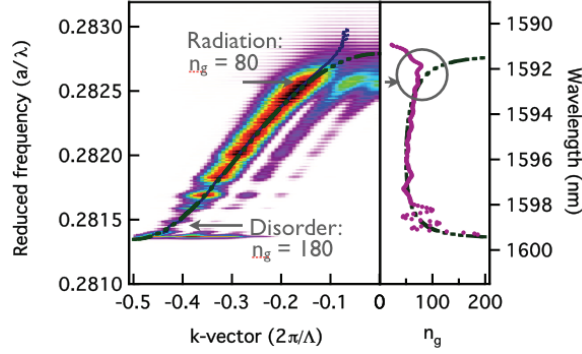
Figure 7.10: Experimental dispersion curve of a CCW compared to theoretical dispersion calculated by tight-binding approximation (dashed line). Maxima of the measured data are depicted by markers to better visualize the discrepancy between the theoretical and the experimental dispersion near the top extremum of the dispersion band. Right: Spectral dependence of the group index.

coupled to the access waveguides by an intermediate photonic crystal waveguide region of $a = 430$ nm. The actual device was processed in 220-nm thick SOI wafer using deep-UV lithography within the collaboration with Ghent University and IMEC.
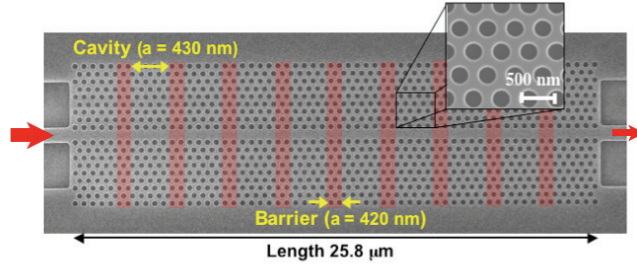
Figure 7.11: Top-view SEM image of a heterostructure coupled-cavity waveguide consisting of 8 cavities. Barrier regions are highlighted by red.

Creation of barriers and cavities in such a system can be understood from comparison of dispersion curves of a W1 waveguide with lattice parameter $a = 430$ and a W1 with reduced lattice constant in the z-direction (*i.e.* $a_z = 420$ nm), as shown in Fig. 7.12(a). In the frequency range from $a/\lambda = 0.2764$ to 0.2800 delimited by mode cutoffs of the respective waveguides, the standard W1 still suports an optical mode, while for the modified W1 no extended optical states exists, it acts as a barrier. This is exactly the spectral region, where the CCW mode can be formed.

Dispersion diagram of the full CCW structure calculated by guided-mode expansion (GME) method [76] is presented in Fig. 7.12(b) (dotted line). At higher frequencies the mode dispersion is similar to the dispersion of a standard W1 waveguide, folded by the periodicity of the super-cell defined by $\Lambda = 4\,a + 2a_z$. In this frequency range the barrier regions still support a propagating mode and the upper band represents a dispersion curve
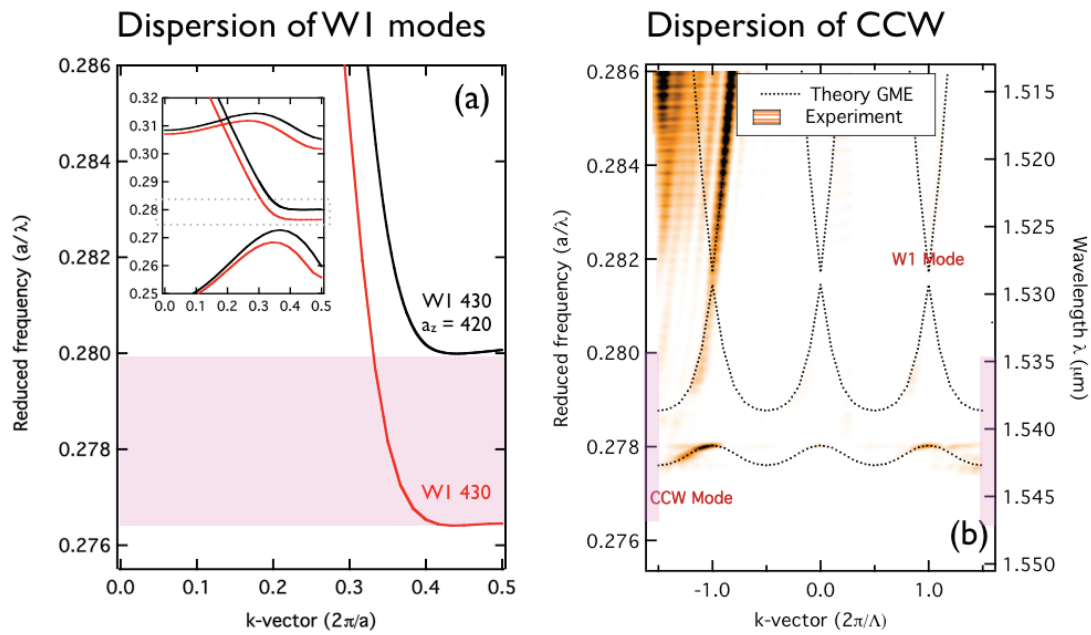
Figure 7.12: (a) Theoretical dispersion curves of a W1 waveguide with lattice parameter $a = 430$ (red) and the barrier region W1 with reduced lattice constant in the z-direction to 420 nm (black) calculated by GME. (b) Comparison of the experimentally measured dispersion (image plot) and the CCW dispersion simulated by GME, depicting both the "W1 mode" and the CCW mode.

of a weakly corrugated W1 waveguide. The coupled cavity mode appears approximately 4 nm below the cut-off of the "W1 mode" and is characterized by cosine-shape dispersion of a bandwidth spanning 2.6 nm (0.33 THz). The close proximity of the "W1 mode" and the CCW mode implies that an important interaction between the two modes is expected. The coupled cavity chain cannot be considered anymore as an impurity found deep enough in the photonic bandgap, for which the Tight-Binding model in its simplest form (Eq. (7.2)) holds.
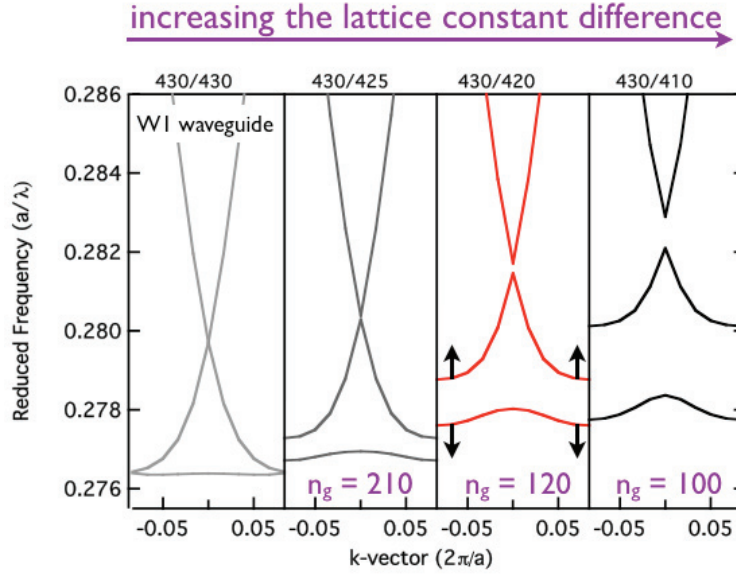
Figure 7.13: CCW mode formation upon gradually decreasing the barrier lattice constant a_z from 430 nm (folded W1 waveguide) to 410 nm simulated by GME.

Alternatively, the heterostructure CCW mode can be understood in terms of a perturbed W1 waveguide; it is a result of the anticrossing of the folded W1 modes, which are coupled due to the perturbation introduced by the barriers. This is illustrated in Fig. 7.13, which shows how the W1 mode splits and the band diagram is formed once the coupling interaction is introduced. The perturbation modifies the band diagram primarily at the Brillouin zone boundary, where the anticrossing point is located. Increasing the lattice constant difference between the barriers and cavities pushes the low-frequency cutoff of the CCW mode away from the anticrossing point, until a nearly sinusoidal coupled-cavity band is formed. Note, that the CCW bandwidth increases with the perturbation, *i.e.* the lattice constante difference between the barriers and the cavities, which is an opposite effect as would be expected from the TBA: stronger lattice constant mismatch would imply a reduction in the coupling strength and consequent flattening of the dispersion curve.

7.2.2   Experimental CCW dispersion

The experimental dispersion diagram showing both the CCW and the corrugated W1 waveguide mode is plotted in Fig. 7.12(b), together with the result of the guided-mode expansion simulation. The direct comparison demonstrates a good agreement between the

theory and the measurement in respect of both the position and the slope of the investigated modes. It should be stressed that the full three-dimensional nature of the structure must be taken into account (expansion into the guided modes of the slab - GME or full 3D plane wave expansion) in order to simulate the proper position, curvature and bandwidth of the CCW. The 2D PWE combined with effective index approach, which is still widely used in the photonic crystal community, completely fails to reproduce the dispersion of the present coupled-cavity waveguide design.

As aforementioned, the periodicity of the CCW allows to probe the dispersion of such a waveguide by far-field optics, without the need of additional near-field probes. The numerical aperture NA = 0.9 of our imaging system allows us to probe the first three Brillouin zones nearest to the center of the dispersion plane. Hence, in the dispersion map (Fig. 7.12(b)) we observe three dispersion curves, which are identical in shape, but offset along the k-vector coordinate by the reciprocal vector of the coupled-cavity chain $2\pi/\Lambda = 2.45\,\mu m^{-1}$. Their peak intensities reflect the energy distribution in individual Brillouin zones, *i.e.* the relative intensities of the spectral components of the Bloch mode.

A closer zoom on the CCW mode dispersion is given in Fig. 7.14(a), which presents the experimental dispersion curve in the 2nd Brillouin zone normalized in intensity, together with the theoretical band diagram calculated by the guided-mode expansion method. Red markers that depict the maxima of the experimental data help to visualize the measured dispersion curve. The experimental dispersion $\omega(k)$ is smooth enough to be numerically differentiated to obtain the group index and its frequency dependence, as is shown at the right.

The group index does not drop below 105 ± 20 within the entire linear bandwidth of the CCW, which extends over approx. 2 nm. The experimental dispersion relation agrees well with the theoretical calculations until a maximum group index of approximately $n_g = 300$, which is one of the largest experimental group index values reported for an optical waveguide. The relevance of this value, however, is moderated by the short length of the structure which was as little as 25 μm. Above $n_g = 300$, the CCW mode deflects from the ideal cosine-shape dispersion and gets smoothly coupled into a slow-decaying evanescent modes that emerge from the top/bottom of the dispersion band. The existence of such evanescent modes is confirmed theoretically by modified 2D PWE[1] frequency-based simulation as shown in Fig. 7.14(b) (see section 1.3.7, paragraph *Numerical calculation methods*). Here the CCW dispersion curve characterized by purely real k-vector components is plotted together with four evanescent modes appearing at the top and at the bottom of the CCW band. Of all evanescent modes existing in the given spectral range, the depicted ones exhibit the lowest imaginary wave-vector components. Their decay length at the proximity of the CCW band exceeds several lattice constants, making it possible to observe them experimentally using the Fourier-space imaging.

7.2.3   Slow-light PhC waveguides: Figures of Merit

To evaluate the energy performance and the buffering capacity of photonic devices, in particular for slow-light telecom oriented applications, two figures of merit are currently used:

---

[1]Although the 2D PWE can't reproduce correctly the dispersion of the CCW band as mentioned above, we still can use it to gain deeper qualitative understanding of phenomena occurring in the CCW structure, such as existence of evanescent modes. Nevertheless, GME or 3D PWE tool that can simulate the imaginary k-vector components, if available, should be of primary choice.
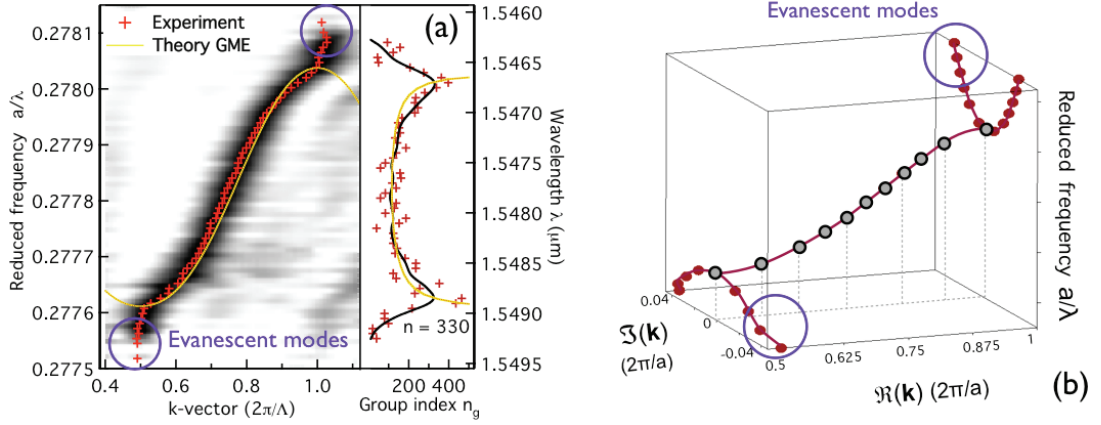
Figure 7.14: (a) Normalized dispersion curve of the heterostructure CCW mode (left) and its group index ng (right). The experimental group index was obtained by both numerical differentiation of the raw data (crosses) and data interpolated by a spline function (black curve). (b) Frequency-based 2D PWE calculation of the CCW dispersion band (gray) and the slowly decaying evanescent modes that appear at the in the proximity of the CCW band extrema (red).

The delay-bandwidth product (DBP)

$$DBP = \Delta t \Delta f = n_g \frac{\Delta \omega}{\omega} \frac{L}{\lambda} \tag{7.10}$$

where Δt is the delay, Δf the frequency bandwidth. The expression for DBR depends on the group index n_g, relative bandwidth $\Delta \omega / \omega$, wavelength and the length of the device L. The latter dependence is excluded in the following definition of the **length-normalized delay-bandwidth product** [164], also referred as group index-bandwidth product [146]:

$$DBP_N = n_g \frac{\Delta \omega}{\omega} \tag{7.11}$$

which is more practical for optical slow light applications, as it expresses the delay achievable with a current waveguide *design*, independently of its length and technology used. Also, it is important to set a general criterion how to define the operation bandwidth. It turns out that for most practical applications, such operation bandwidth can be defined as a range of frequencies, within which the group index remains constant within 10%, which sets the practical limits of acceptable group velocity and higher order dispersion.

In photonic crystals, the periodicity of the PhC lattice imposes a strict relation between the group index and the bandwidth, and hence, an upper limit of the maximal achievable DBP_N. Because of the periodicity of the dispersion curve in the reciprocal space, the wave vector span is limited to one half of the Brillouin zone (see Fig. 7.1(b)):

$$k = \frac{\Delta \omega n_g}{c} < \frac{\pi}{\Lambda} \Rightarrow \Delta \omega < \frac{\pi c}{n_g \Lambda} \tag{7.12}$$

where n_g is assumed constant over the bandwidth $\Delta \omega$ and Λ is equal to the lattice constant for W1 waveguide or the supercell length for the CCW. In consequence, the DBP_N is

limited by:

$$DBP_N < \frac{\lambda}{2\Lambda} \tag{7.13}$$

In this context, the CCW systems have a clear disadvantage as the k-span, and hence, the bandwidth is reduced Λ/a-times compared to the W1. In Table 7.1, where DBP_N and maximum DBP_N^{max} for different slow light waveguide structures is reported, one can see that there is still margin for improvement for the W1 waveguides, however, principally all CCW systems regardless of the cavity design are very close to the theoretical limit.

On the other hand, the coupled-cavity waveguides can exhibit better slow-light performance in the presence of disorder. In the CCWs, the disorder is averaged over large supercell and therefore group indices Λ/a-times larger can be achieved than in the case of a simple W1, before the detrimental back-scattering and localization take place. The Λ/a-times lower sensitivity to disorder in CCW systems was confirmed theoretically by V. Savona [142], and witnessed by experimental results treated in this work: while W1 waveguides can reach maximum group index of 50-60, the L3-based CCWs ($\Lambda = 4\,a$) show onset of localization only at $n_g = 180 \sim 4 \times 50$ and the heterostructure CCWs ($\Lambda = 6a$) are able to achieve the index as high as $n_g = 300 \sim 6 \times 50$.[2]

Loss per length   is the most standardly used figure of merit to evaluate the propagation loss of a waveguide due to out-of-plane radiation, absorption or scattering. Its definition is based on the Lambert-Beer's law:

$$T \sim \exp^{-\alpha_L z} = \exp^{-z/L} \tag{7.14}$$

where T is the transmission through device, α_L is the loss per length, most commonly given in dB/cm or dB/mm units. The loss can be also expressed in terms of an attenuation length $L = 1/\alpha_L$.

For slow-light devices, a more appropriate measure of loss was proposed [146], which is the **Loss per unit time**:

$$\alpha_t = \frac{\alpha_L c}{n_g} \tag{7.15}$$

Such a definition refers the optical loss directly to the achievable delay, which better expresses the primary purpose of slow-light devices, *i.e.* to achieve a delay while maintaining satisfactory transmission. In this context, the loss per device length is not of primary importance and shorter devices providing the same delay are often preferred.

Loss per relative time.   If one figure of merit should be used to comprehensively characterize the performance of a slow-light device including its buffering capacity, signal retardation and optical loss, a good candidate could be the Loss per relative time, *i.e.* loss per time normalized by the temporal duration of pulse spectrally limited by the structure $\Delta t = 1/\Delta \nu$.

$$\alpha_{tN} = \frac{\alpha_L c}{n_g} \frac{1}{\Delta \nu} \tag{7.16}$$

---

[2]To make the comparison strictly rigorous, devices of the same length should be considered: Significant line broadening in k-space masks the effect of disorder, which appears in consequence less detrimental for short structures than for long devices of the same slow-light performance.

Here $\Delta\nu$ is the frequency bandwidth given in THz and α_{tN} the dimensionless loss per relative time. The smaller the α_{tN} parameter, the more suitable is the device for slow light applications.

Practical examples

In the following, we will discuss the previously mentioned figures of merit for four different device designs (see Tab. 7.1): Heterostructure coupled-cavity waveguides and Coupled-cavity waveguides based on moderate-Q L3 cavities reported in this work, coupled cavity waveguides based on ultrahigh-Q cavities presented by Notomi et. al [21] and W1 slow light engineered waveguides studied by the group of T. F. Krauss [58].

Structure	n_g	$\Delta\lambda$ (nm)	DBP_N	DBP_N^{max}	Loss/length α_L (dB/mm)	Loss/time α_t (dB/ns)	Loss/time$_N$ α_{bN}(dB)
Hetero. CCW	105	2	0.14	0.30	300*	860	3.43
L3 CCW	50	3	0.10	0.43	50	300	0.81
CCW Notomi [21]	100	1.5	0.10	0.24	14	42	0.22
Engineered W1 [58]	25	15	0.24	1.80	5	60	**0.032**

*Loss with bottom oxide cladding

Table 7.1: Figures of merit of slow light structures: comparison.

Table 7.1 shows that the slow-light engineered W1 waveguides exhibit the best properties concerning both the losses and the optical delay. Although they don't exhibit record-breaking group indices, due to inherently low loss they can be made longer and thus provide for large enough optical delays. Their most important asset is their large operation bandwidth of one order of magnitude higher than for the CCW devices, that allows for bit rates as large as 100 Gbit/s.

After the engineered W1 waveguides, the second best choice would be the ultrahigh-Q CCW waveguide design. However, the figures of merit listed in Tab. 7.1 neglect the fact that the transmission through this device is not continuous, but does exhibit large variations (>20 dB), which necessarily leads to pulse distortion and residual echoes. On the other hand, L3-based devices can achieve flat-top frequency response, however, the price to pay is largely increased propagation loss.

Finally, the heterostructure CCW exhibits very high group index, but also excessive propagation loss, which makes it unsuitable for practical applications. In the future, the propagation loss could be largely reduced by the bottom oxide cladding removal.

To summarize, if CCW devices are to be used in practical applications, there are two principal aspects that must be solved: the design of a single cavity constituent has to be engineered to provide for homogeneous emission profile to avoid strong variations in transmission within the CCW bandwidth. Moreover, for a given sample length (defined by

the desired optical delay), the Q-factor of constituent cavities has to be chosen according to condition Eq. (7.6), in order to guarantee a trade-off between the flat-top transmission response and the lowest possible propagation loss

Chapter 8

Hollow-core photonic crystal structures

Line-defect waveguides and optical cavities realized in photonic crystals allow for strong optical field confinement, which leads to dramatic enhancement of both the optical intensity and the light matter interaction. In photonic crystal waveguides, such a strong optical confinement is possible both due to the bandgap effect and the temporal compression of optical pulses in the slow light regime. In the case of cavities, photonic crystal environment offers a lot of degrees of freedom to engineer the cavity design and achieve high quality factors of the order of Q $\sim 10^6$ within an extremely small volume [44, 45]. Therefore, they find a vast number of applications in nonlinear physics, quantum electrodynamics, and based on experimental demonstrations achieved to date, they also constitute a promising building block for optical (bio)sensors [22, 49]. However, in typical PhC devices, the strong light-matter interaction occurs in the high index material where the majority of optical field is located, making it difficult to efficiently probe the physical properties of the surrounding low index medium. Enhancement of the field overlap between the optical mode and the cladding medium would be beneficial *e.g.* for optical sensing applications, as it would increase the device sensitivity and/or lead to the reduction of the necessary amount of analyte.

One solution to increase the interaction between the optical mode and the surrounding environment is to introduce a narrow, nanometer-wide air-slot within the core region of the waveguide (or cavity), and thus create a device similar to nanophotonic slot waveguides discussed in Chapter 4. In such a hollow-core photonic crystal structure, the TE polarized modes are confined in the slot allowing for a large interaction of the optical field with the low index medium, and at the same time, the structure maintains the versatile dispersion properties of photonic crystals [165]. In other words, the speed of light propagation in the photonic crystal slot waveguides as well as optical confinement in the cavities can still be controlled by the means of dispersion engineering.

The main focus of this chapter is to experimentally investigate the light propagation in hollow-core photonic crystal devices in order to visualize their dispersion and to quantify their sensitivity to changes of the external environment. In particular, a new type of a PhC air-slot cavity is proposed and tested as a high precision gas index sensor.

8.1   Slotted W1 waveguides

The schematic drawing of the air-slot waveguide under consideration is shown in Fig. 8.1. The photonic crystal cladding is characterized by a lattice constant $a = 510$ nm and filling factor of $f = 0.4$, and the slot width was set to 120 nm. The theoretical dispersion of the waveguide calculated by GME method is presented in Fig. 8.2(a).
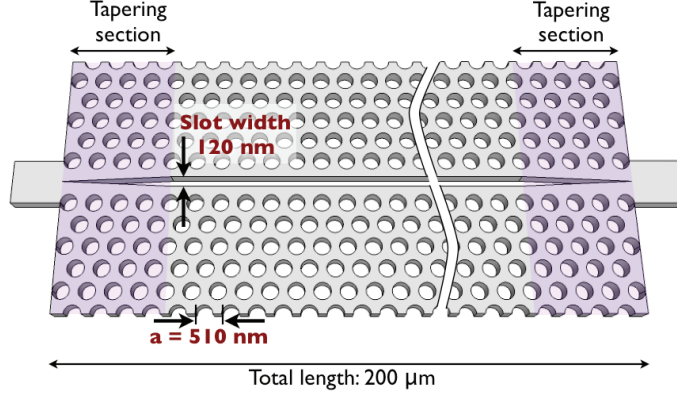
Figure 8.1: Illustration of a photonic crystal slot waveguide.

When opening an air-slot inside the W1 defect region, the original line defect modes (labelled as W1-odd and W1-even in Fig. 8.2(a)) are shifted to higher optical frequencies as a result of increasing overlap of their field with the air. The even W1 mode which is strongly confined within the line-defect region is shifted rapidly towards the air band, while the odd W1 mode is only marginally affected due to a rather weak mode profile overlap with the air-slit. In addition, a new waveguide mode denoted as slot-waveguide mode (SW1) is lifted up from the dielectric band, shifting its cut-off to higher frequencies as the width of the slit increases. It is characterized by even symmetry, positive slope of the dispersion curve and strong spatial overlap of the optical field with the air Γ:

$$\Gamma = \frac{\int_a |\mathbf{E}(\mathbf{r})|^2 d^3 r}{\int_{a+d} |\mathbf{E}(\mathbf{r})|^2 d^3 r} \tag{8.1}$$

where a stands for the air and d for the dielectric. For the 120 nm wide slit the spatial overlap of the SW1 mode with the air is as high as 92%. As discussed in J. Gao et al. [166], its origin can be traced back to the second-order quasi-guided mode that is found below the projected bulk modes in the dispersion diagram of a standard W1 waveguide.

To study the dependence of the dispersion curve on the slot dimensions, we tune the slit width from 60 to 200 nm and plot the simulation result in Fig. 8.2(b). If the slit is too narrow, *i.e.* below approx. 60 nm, the SW1 mode is found within the dielectric band and is not fully guided within the plane. However, further increase of the slot width induces a rapid shift of the mode cutoff towards the air band, which is correlated to the increase of dispersion curve slope in its linear part. It should be noted that the increase of the slit width from 100 to 120 nm, *i.e.* by only 20 nm, leads to the shift of the mode cutoff by as much as 50 nm. Such a high sensitivity of the dispersion to the slit width results in high sensitivity of the device to disorder and an accentuated need for high

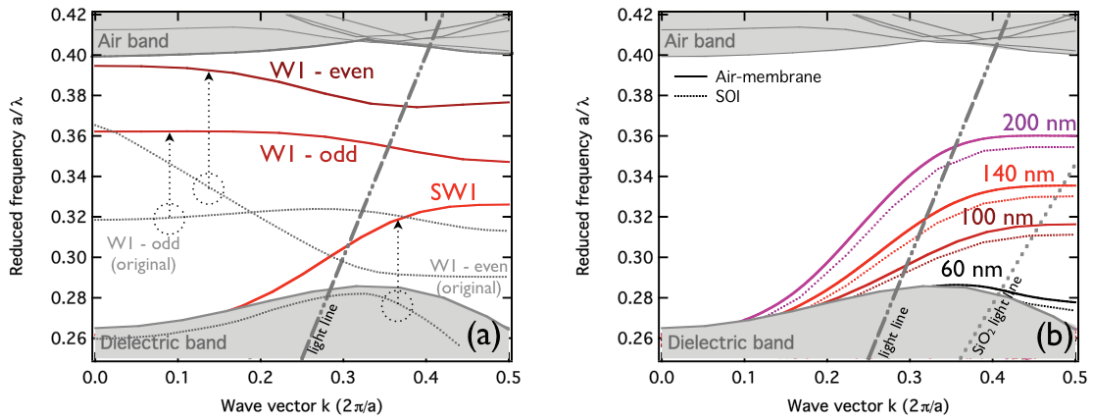**Figure 8.2:** (a) Dispersion diagram of a W1-based slot waveguide with $a = 510$ nm and slot width of 120 nm, showing the slot waveguide mode (SW1), the original W1-odd and W1-even mode, as well as their position within the photonic crystal bandgap. (b) Change in the slot waveguide mode dispersion upon increasing the slit width from 60 to 200 nm.

precision fabrication. On the other hand, it brings along the possibility to detect with a high precision and sensitivity the presents of particles in the slit, which is particularly appealing for (bio)sensing applications.

For practical applications, it is also important to regard the position of the SW1 mode in respect to the lightline and the silica-light line for SOI-based devices, since the useful bandwidth of the waveguide is limited to the frequency range where its dispersion lies below the two respective lightlines. It turns out that for slot W1-based waveguides with silica bottom cladding and technologically feasible slot widths, such a useful bandwidth is limited to only a couple of nanometers as illustrated in Fig. 8.2(b). In addition, within this spectral range, the waveguide is already in the slow light regime and the transmission through the structure is hindered by disorder and localization as we could witness in experiment. It is therefore imperative to fabricate the devices in an air-bridge membrane, which may, on the other hand, impose limitations on the total length of the device; the photonic crystal membrane separated in the middle by an air slit is susceptible to bend down, inducing a slight variation of the slit with along its length and thus negatively affecting the mode propagation. The membrane deformation is a possible reason why no experimental transmission was observed for devices longer than 200 μm.

Taking the above consideration into account, slot W1-based waveguides were fabricated at EPFL in 220-nm thick Si membrane. The lattice constant and the filling factor were the same as used in the simulations and the slot width was varied between 80 to 120 nm in the step of 10 nm. Good transmission was obtained through samples with the slot of 90 nm and wider; in the 80 nm wide slot the light propagation was strongly affected by the slot sidewall irregularities, as witnessed by strong out-of plane scattering observed in the near field along the waveguide core region, showing that the 80 nm line is indeed at a limit of our fabrication technology.

The experimentally measured dispersion curve for a 120-nm wide waveguide is plotted together with the measured transmission in Fig. 8.3. As the waveguide operates below the
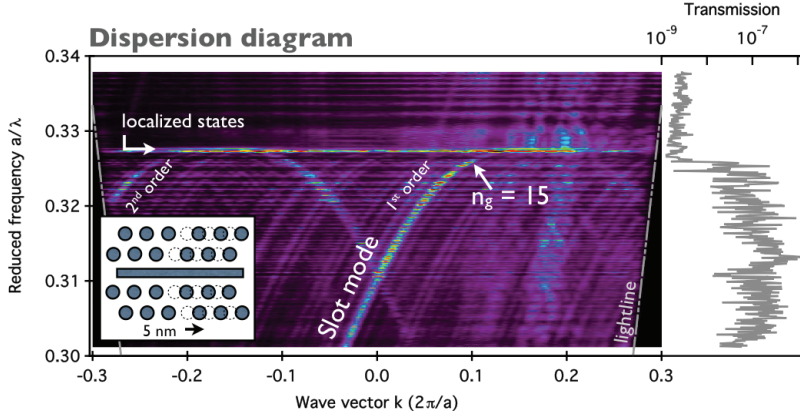
Figure 8.3: Experimental dispersion and transmission for a slot waveguide with 120-nm wide air-slit. The inset shows a schematic drawing of the grating probe design.

light cone, one-dimensional volume grating probe has to be included in the design in order to fold the dispersion curve into the light cone and allow for FSI measurement. In this particular case, the grating was realized by increasing the lattice constant of the photonic crystal every third period along the propagation direction by 5 nm. The measured dispersion curve has nearly parabolic shape and its group index increases from $n_g = 4$ measured in the fast-light region to the maximum value of $n_g \approx 15$ before the light propagation gets limited by disorder. Compared to the group index of ~ 50 measured for standard W1 waveguides, we can conclude that the slow light propagation in slot waveguides is more importantly affected by disorder. This can be explained by a large amplitude of the optical field at the slot side-walls and hence, intense interaction of the light and side wall roughness and defects. Moreover, large sensitivity of the mode dispersion to the fluctuations of the slot width may also contribute to the loss of optical signal in the slow light regime.

Besides the group index, the waveguide termination has also an important effect on the signal transmission. In the present work we adopted the approach of adiabatic tapering of the slot width as shown in Fig. 8.4(a), however, the transmission still exhibits oscillations of 10dB (despite antireflection coating on the sample facets), confirming that large impedance mismatch still occurs at the sample-access waveguide boundary. In the future, the inverse taper approach shown in Fig. 8.4(b) [167] is envisaged, the design of which might be delicate as it has to be adapted to a free-standing membrane structure. Fast-light taper section similar as for W1 waveguides as discussed in Chapter 6.1 will be equally added to account for better fast-slow light matching at the interface.

8.2 Air-slot cavity

Photonic crystal air-slot cavity was firstly proposed in a 1-D photonic crystal by Robinson et al. [168], followed by several different designs in PhC slabs [169,170]. To create a cavity, one can either modify the properties of the PhC mirror, or the dimensions of the slot itself. The first approach was adopted by A. Di Falco and coworkers [169], who locally reduced the lattice constant of the photonic crystal to create a heterostructure cavity, as well as by Yamamoto et al. [170] and Gao et al. [166], where the holes adjacent to the
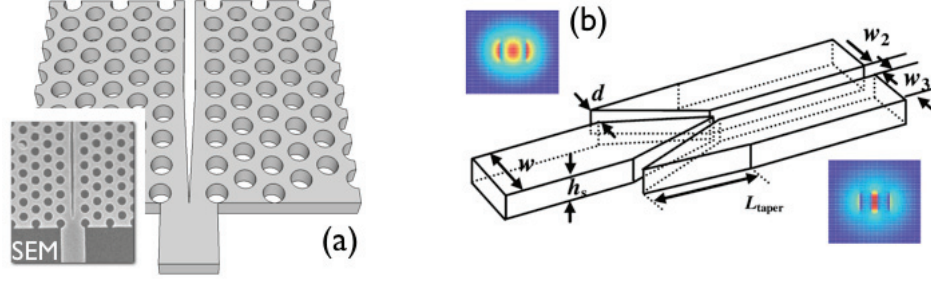
Figure 8.4: (a) Adiabatic taper between access/W1/slot waveguide used in this work. (b) Inverse taper design that allows for over 90% percent coupling efficiency for slot nanowire waveguides, and will be tested in the future for photonic crystal slot waveguides. The figure was taken from [167]

slot were transversally shifted to form a width-modulated line-defect cavity. In the present design, the PhC lattice is kept unchanged, but the width of the air slot is locally reduced by 20 nm to delimit the volume of the cavity as shown in Fig. 8.5. Reduced slit width results in formation of reflective barriers for the cavity mode, as it can be inferred from the dispersion diagram of slot PhC waveguides shown previously in Fig. 8.2(b). The 120 nm slot waveguide mode lies at slightly higher frequencies than the 100 nm one, and hence, it can create a defect state when sandwiched between two 100 nm slot waveguide sections.
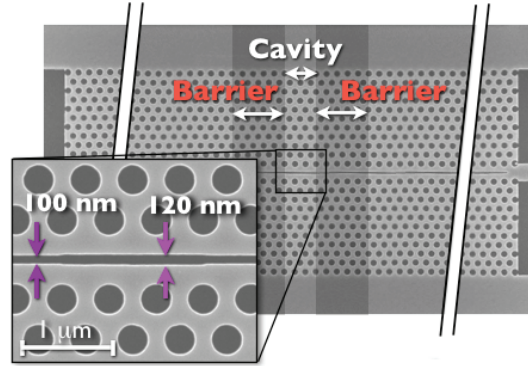
Figure 8.5: Top-view SEM image of the air-slot cavity structure with barriers highlighted in dark grey. Inset shows a detail of the cavity region.

We focus on a cavity with the length equal to three lattice constants $L = 3a$, the resonant state of which is found between the cutoffs of the 120 and 100 nm wide slot waveguides as calculated by GME and shown in Fig. 8.6. The corresponding electric field distribution plotted in the inset of the same figure confirms that the cavity mode is strongly confined within the slot region, having an effective mode volume:

$$V_{\text{eff}} = \frac{\int \varepsilon(\mathbf{r})|\mathbf{E}(\mathbf{r})|^2 d^3 r}{\max[\varepsilon(\mathbf{r})|\mathbf{E}(\mathbf{r})|^2]} = 0.053 \, \mu\text{m}^3 \qquad (8.2)$$

where $\varepsilon(\mathbf{r})$ is the permittivity distribution. However, note that despite the definition Eq. (8.2) is often cited in literature [45, 171] and used by broad scientific community, it is not ideally suited to quantify the mode volume of hollow-core structures. The discontinuity of the electric field at the slot boundaries may introduce a large error, especially if the denominator is to be evaluated numerically. Therefore, the mode volume value calculated by Eq. (8.2) is largely sensitive to the structure meshing and the used calculation method. Mode volume defined by the following relation:

$$V'_{\mathrm{eff}} = \frac{\left[\int \varepsilon(\mathbf{r})|\mathbf{E}(\mathbf{r})|^2 \mathrm{d}^3 r\right]^2}{\int \left[\varepsilon(\mathbf{r})|\mathbf{E}(\mathbf{r})|^2\right]^2 \mathrm{d}^3 r} = 0.51\,\mu\mathrm{m}^3 \tag{8.3}$$

would give a more meaningful and reliable argument. Such a definition of the mode volume is inspired by the theory of localization, namely the definition of the Inverse Participation Ratio, which characterises the spatial extent of a localised state: $IPR = \int |\varphi(x)|^4 \mathrm{d}x$, where $\varphi(x)$ is a wavefunction normalized to unity [172]. Nevertheless, in order to allow for quantitative comparison with similar devices reported in literature, the first value of $V_{\mathrm{eff}} = 0.053\,\mu\mathrm{m}^3$ will be quoted in the following text.

The spatial overlap Γ with the gas is as high as 0.83 and the theoretical quality factor reaches $Q = 28000$. The mode volume, spatial overlap and the Q-Factor were obtained from FEM simulation performed by Ulagalandha Perumal Dharanipathy using the COMSOL software package. The computational domain used for the calculation enclosed 24 columns by 17 rows at the center of the structure and the Scattering Boundary Conditions were imposed on the boundary surfaces of the device. Custom fine meshing was done in the slot, otherwise the meshing was optimized according to the availability of computational resources.

Knowing the mode field overlap Γ, the first order perturbation theory [173] can be used to estimate the sensitivity of the cavity resonance frequency to the refractive index change Δn inside the slot. Taking into account only the first order perturbation [174], the
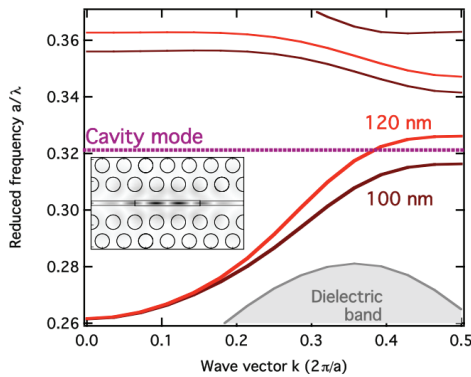

Figure 8.6: Theoretical dispersion curves of the 100 and 120 nm wide slot waveguides (solid line) shown together with the air-slot cavity resonance (dashed line). Inset shows the electric field distribution $|\mathbf{E}_{xy}|$ of the cavity mode.

frequency change can be expressed as:

$$\frac{\Delta\omega}{\omega} = -\frac{1}{2}\frac{\int \mathbf{E}(\mathbf{r})\Delta\varepsilon(\mathbf{r})\mathbf{E}(\mathbf{r})d^3r}{\int \mathbf{E}(\mathbf{r})\varepsilon(\mathbf{r})\mathbf{E}(\mathbf{r})d^3r} \tag{8.4}$$

where ω is the resonance frequency of the cavity, ε the unperturbed dielectric permittivity and $\Delta\varepsilon$ the change of the dielectric permittivity inside the slot. Denoting the volume of the low index material as a (air) and the volume of the high index medium as d (dielectric), one can rewrite the expression above as follows:

$$\begin{aligned}\frac{\Delta\omega}{\omega} &= -\frac{\Delta\varepsilon}{2}\frac{\int_a |\mathbf{E}(\mathbf{r})|^2 d^3r}{\varepsilon_a \int_a |\mathbf{E}(\mathbf{r})|^2 d^3r + \varepsilon_d \int_d |\mathbf{E}(\mathbf{r})|^2 d^3r}\\ &= -\frac{\Delta\varepsilon}{2}\frac{1}{\varepsilon_a + \varepsilon_d\left[\frac{1}{\Gamma}-1\right]}\\ &= -\frac{\Delta\varepsilon}{2}\frac{\Gamma}{\varepsilon_{\text{eff}}}\end{aligned} \tag{8.5}$$

where $\varepsilon_{\text{eff}} = \Gamma\varepsilon_a + (1-\Gamma)\varepsilon_d$ and Γ is the spatial mode overlap defined by Eq. (8.1). Expressed in terms of the wavelength and the refractive index:

$$\frac{\Delta\lambda}{\lambda} = \frac{\Delta n\,\Gamma}{n_{\text{eff}}} \tag{8.6}$$

where $n_{\text{eff}} = \sqrt{\Gamma\varepsilon_a + (1-\Gamma)\varepsilon_d}$ stands for the effective refractive index of the cavity. The sensitivity of the cavity resonance to the change of the refractive index of the surrounding environment can be expressed as:

$$S = \frac{\Delta\lambda}{\Delta n} = \Gamma\frac{\lambda}{n_{\text{eff}}} \tag{8.7}$$

For the resonance wavelength $\lambda = 1570$ nm, $n_{\text{air}} = 1$ and $n_{\text{Si}} = 3.47$ we get a sensitivity of $S = 770$ nm per refractive index unit (RIU), which is quite remarkable for a device with an active sensing volume as low as $V_{\text{eff}}\Gamma = 0.04$ $\mu m^3 = 40$ attoliters (al).

Sensitivity of the air-slot cavity was also calculated by the FEM-based COMSOL solver, where the change in the resonance frequency of the cavity was simulated as a function of varying index of the surrounding medium. The simulation yield the sensitivity of 460 nm/RIU, which is surprisingly lower than the sensitivity obtained from the perturbation theory and, as shown below, even lower that the experimentally measured value (590 nm/RIU). It it yet to be clarified if such a discrepancy is related to the computational issues (meshing, precision of the definition of the group index, etc...) or to small variation of structural parameters between the ideal and the fabricated device.

The air-slot cavity of above specified parameters was fabricated at EPFL and was characterized using our combined End-fire–Fourier space imaging setup. The air-slot cavity is excited in inline configuration through $5a$-long barrier region into the cavity, as shown in Fig. 8.5. The length of the barriers was carefully chosen to achieve a high loaded Q-factor while keeping the transmission at a detectable level. In parallel with the standard end-fire transmission measurement, the light emitted from the sample surface is collected by a high numerical aperture microscope objective and detected with an infrared CCD

camera. The long working distance Olympus LMPlanFI objective of NA = 0.8 was used in this particular measurement in order to leave large enough distance between the sample surface and the objective, as required later in the gas-sensing experiment.

The experimental transmission spectrum of the air-slot cavity is shown in Fig. 8.7(a). The cavity barriers are transparent down to 1590 nm, where the mode cutoff of the 100-nm wide slot waveguide is found. Approximately 20 nm below this cutoff we can observe a narrow transmission peak that corresponds to the resonant mode of the cavity. A broad resonance also observed at 1580 nm between the cavity mode and the barrier cut-off was attributed to an evanescent mode, which can penetrate through the barriers due to evanescent coupling and thus contribute to undesired background in transmission. Such residual background resonances could be eliminated in the future by employing lateral (*i.e.* outline) coupling scheme for the cavity excitation.
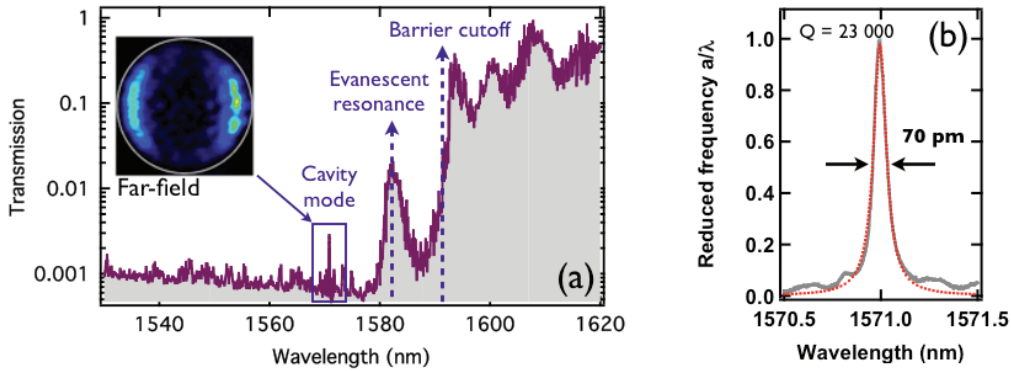
Figure 8.7: (a) Tranmsission spectrum of the air-slot cavity. Inset: far-field emission profile of the cavity at the resonance cavity wavelength. (b) Emission spectrum (grey) plotted together with the Lorentzian fit (red dotted line).

Although the transmission peak attributed to the cavity mode is weak, its spectral position is unambiguously confirmed by the far-field imaging, which allows to identify the cavity resonance although the transmitted signal is weak or accompanied with spurious resonances. In the far-field, the cavity mode exhibits a stable, highly symmetric pattern as shown in the inset of Fig. 8.7(a), which differs distinctly from the speckle-like emission of the residual resonance peaks. The light radiated from the sample surface and recorded as a function of the wavelength yields the emission spectrum of the cavity, which is shown in the inset of Fig 8.7(b). Unlike the transmission, it exhibits an excellent signal to noise ratio with Lorentzian line-shape, and was therefore used to analyze the spectral properties of the cavity. The Lorentzian fit of the emission peak gives the linewidth of 70 ± 1 pm, yielding a loaded quality-factor Q = 23'000.

8.2.1   Refractive index sensing

In order to assess the sensing potential of the cavity, we expose the sample to gases of different optical refractive index such as nitrogen N_2 ($n = 1.000270$) [175], helium He ($n = 1.000032$) [176], carbon dioxide CO_2 ($n = 1.000407$) [175], propane C_3H_8 ($n = 1.000999$) [175] and acetylene C_2H_2. The refractive index values are given at atmospheric pressure

and were recalculated for $\lambda = 1570$ nm and room temperature $T = 20°$C using the ideal gas model [177]. This was possible for all gasses but acetylene, which exhibits a series of strong absorption lines in the 1.5 μm spectral window.
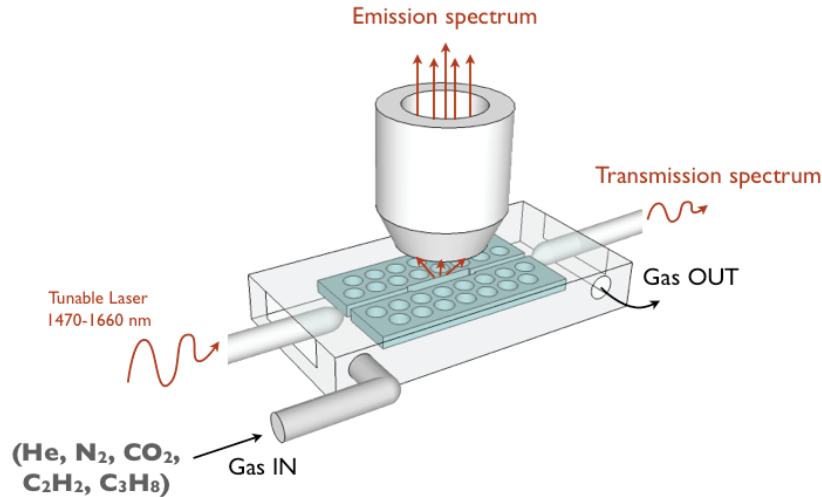
Figure 8.8: Illustration of the experimental transmission/far-field imaging setup and the assembly for the gas infiltration.

During the measurement, the sample is placed in a gas cell as schematically illustrated in Fig. 8.8 that is equipped with a gas inlet, two micrometer-size openings for the optical fibers and an outlet for gas evacuation. Moreover, the cell has a thin transparent window positioned $\sim$100 μm above the sample surface to facilitate for the far-field imaging of the cavity emission. The gas is injected into the cell at a constant rate, fills the volume of the cell and escapes by the outlet opening, thus avoiding the overpressure inside the cell. The flux rate is set to a value just sufficient to entirely fill the cell volume in order to avoid residual effects of the gas flow such as input/output fiber vibrations and the sample cooling due to gas flow. The desired flux of the test gas was set by observing the shift of the cavity resonance upon accruing concentration of gas; when a new increase of the gas flux does not induce further shift in the resonance wavelength, the cell is considered to be completely filled with the analyte.

The shift of the air-slot cavity resonance in response to the change of the gas refractive index is shown in Fig. 8.9. Considering nitrogen as the reference medium, we can observe both blue shift of the resonance peak for He and red shift for the other gases; CO_2, acetylene and propane. Only a weak variation of the peak profile and its quality factor was observed upon exposure; experimental Q-factor varied between 20 000 to 26 000, primarily due to spurious Fabry-Perot resonances slightly affecting the peak profile. As plotted in Fig. 8.10, the dependence of the wavelength shift on the refractive index change ($n - 1$, for the gases with known refractive index) is strictly linear and yields the experimental sensitivity $\Delta\lambda/\Delta n = 590$ nm/RIU, which is slightly lower than predicted by the perturbation analysis and at the same time slightly higher that obtained from direct FEM simulation.

From the knowledge of the experimental sensitivity and the reference resonance peak

Figure 8.9: Spectral position of the cavity resonance upon exposure to helium, nitrogen, carbon dioxide, acetylene and propane.

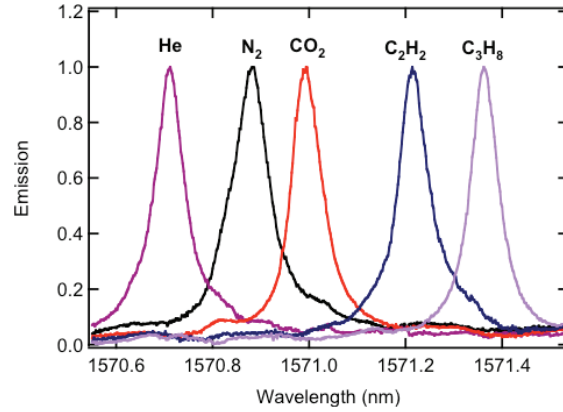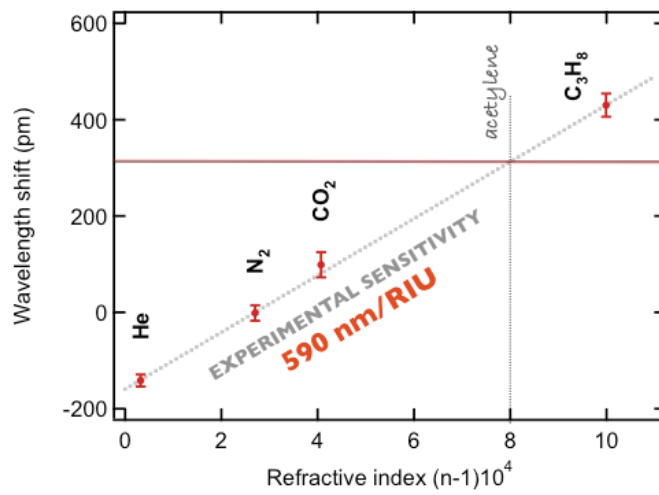**Figure 8.10:** Wavelength shift of the cavity resonance as a function of the refractive index $n-1$ of the respective gas, yielding the sensitivity of 590 nm/RIU. The refractive index of acetylene at 1570 nm of 1.0008 can be retrieved from the linear dependence $\Delta\lambda(n-1)$.

position (*e.g.* for the air), we can retrieve the refractive index of acetylene at the wavelength of 1570 nm: the peak shift of 313 nm measured for acetylene corresponds to the refractive index of $n = 1.0008$ as illustrated in Fig. 8.10.

Repetitive measurements on a longer time scale show that the peak position can be retrieved with a precision of ± 3 pm, which implies the detection limit (defined as the ratio between the resolution and the sensitivity) of 1×10^{-5} RIU, which is comparable with state of the art devices [22]. Nevertheless, it should be mentioned that along with the refractive index of the surrounding medium, there are other parameters that can induce a shift of the resonance frequency of the air-slot cavity mode, *e.g.* temperature, humidity adsorbed at the structure sidewalls, or progressive oxidation/nitridation of the sample surface.

The resonance frequency shift due to temperature can be estimated from the perturbation theory and the known values of the thermo-optic coefficient for silicon substrate and the respective gasses as:

$$\text{Si:} \quad \Delta\lambda = \frac{[1 - \Gamma]\Delta n_{\text{Si}}\lambda}{n_{\text{eff}}}, \qquad \Delta n_{\text{Si}} = \left(\frac{\partial n}{\partial T}\right)_{Si} \Delta T \tag{8.8}$$

$$\text{Gas:} \quad \Delta\lambda = \frac{\Gamma\Delta n_{\text{Gas}}\lambda}{n_{\text{eff}}}, \qquad \Delta n_{\text{Gas}} = \left(\frac{\partial n}{\partial T}\right)_{Gas} \Delta T \tag{8.9}$$

The thermo-optic coefficient of silicon $(\partial n/\partial T)_{Si}$ is approximately $1.84 \cdot 10^{-4}$ K^{-1}, resulting in the resonance wavelength shift of 39 pm/K. Since such a shift corresponds to as much as half of the FWHM bandwidth of the cavity resonance, the air-slot cavity temperature must be well stabilized to account for precise measurements with the detection limit of 1×10^{-5} RIU given above. As the thermo-optic coefficient of the used gasses is of more than an order of magnitude lower than for silicon (*e.g.* $(\partial n/\partial T)_{He} = -1 \cdot 10^{-7}$ K^{-1}, $(\partial n/\partial T)_{N_2} = -1 \cdot 10^{-6}$ K^{-1}, $(\partial n/\partial T)_{C_3H_8} = -3 \cdot 10^{-6}$ K^{-1} as calculated from the ideal gas model [177]), they have only a marginal effect on position of the cavity peak resonance. For helium, nitrogen and propane, the wavelength shift calculated using Eq. (8.9) equals to -0.06, -0.6 and -1.7 pm/K, respectively.

The progressive oxidation of the sample surface turns out to be equally detrimental as it can induce a shift of the resonance peak by as much as 45 pm per hour. This effect can be eliminated when working with N_2 and O_2-free gases, or compensated using an identical reference structure.

To summarize, we presented a highly sensitive refractive index detection scheme with a photonic crystal air-slot cavity, which was tested as an optical gas sensor. The main characteristics of the device are listed in Table 8.1. Besides the spectacular sensitivity of 590 nm/RIU, the major advantage of the sensor is an extremely small active sensing volume of 40 attoliters that is feasible due to strong confinement of the optical field in PhC environment. Such small volume not only allows to drastically decrease the necessary amount of analyte, but it also makes the sensor suitable for high density integration oriented towards parallel or multiplex detection.

The 40 attoliters sensing volume holds as little as $N \pm \sqrt{(N)} = 1 \cdot 10^6 \pm 1 \cdot 10^3$ molecules. With such a small number of molecules, the line broadening due to statistical fluctuations is only about one order of magnitude lower than the present detection limit. Hence, if we manage to further enhance the detection limit by one order of magnitude *e.g.* by increasing the Q-factor of the cavity, we expect to be able to sense such statistical fluctuations. On

Property	Theory	Experiment
Quality factor	28'000	20'000 - 26'000
Mode volume (al)	53	-
Air overlap (%)	83	-
Sensing volume (al)	43	-
Sensitivity (nm/RIU)	460*/720**	590
Detection limit	-	$1 \cdot 10^{-5}$

Table 8.1: Characteristics of the air-slot cavity sensor. * value from FEM and ** perturbation theory.

one hand, this offers an interesting pathway to the mesoscopic physics, but on the other hand, the noise from the fluctuations will finally set the physical limit of the sensor.

Conclusions and outlook

The main objective of the thesis was to both theoretically and experimentally investigate the light propagation in complex nanophotonic structures, which are intended to realize optical interconnects or functional building blocks of future optical integrated circuits. In this context, the principal characteristics to study was the dispersion relation $\omega = f(k)$, which relates the optical frequency ω of the wave vector k of the excited modes. The dispersion relation provides us complete information about the light propagating inside the structure, including the number of supported modes, their phase and group velocity and the higher order dispersion.

To pursue these objectives, we developed and tested an original experimental technique based on Fourier-Space imaging. Compared to standard far-field imaging that can probe only radiative modes, we went beyond by designing weak perturbation gratings that can fold the dispersion of truly guided modes into the light cone, while only negligibly affecting the device performance. Such an approach allowed us to probe the dispersion accurately, locally and without the need for ultra-fast setups or cumbersome data post-processing, as is the case for *e.g.* scanning near-field optical microscopy, SNOM.

In combination with real-space imaging that visualizes the propagating optical signal, the FSI represents an ideal tool to study and conceive the underlying physics of light propagation in optical nanostructures. As a good example, we could witness that current advanced e-beam patterning process results in sub-nanometer periodic perturbations of the dielectric map of fabricated optical devices. Such perturbations, even though they are not resolvable using standard SEM imaging, induce coherent scattering detectable using the FSI and contributing to the propagation loss.

Furthermore, the FSI technique proved to be particularly suitable for characterization of slow-light structures. It allowed us to accurately measure the group index of slow light modes and recognize the main factors limiting its maximum achievable value. Using FSI, could unequivocally distinguish between propagating modes and localized states, and thus make realistic conclusions *e.g.* about minimum speed of light propagation in W1 waveguides. The experimental observation of dispersion curve renormalization, diffusive light transport and light localization due to residual disorder were reported. We also managed to correlate the measured group index with the optical loss due to localization, evanescent mode mixing and back- and out-of-plane scattering. Equally, we addressed the problem of light incoupling into the slow-light modes by testing specially designed fast-slow mode photonic crystal tapers.

Within the framework of this thesis, the FSI technique was applied to experimentally study the optical properties of a large number of nanophotonic devices ranging from simple nanowire waveguides to complex photonic crystal hollow-core structures. Besides dispersion properties, we investigate the effects of radiation losses, disorder and localization on

the optical signal propagation and their dependence on the group index. A short summary of different projects is given below:

SOI wire waveguides and slot waveguides intended for nonlinear experiments. Dispersion as well as group velocity dispersion was measured in order to identify the phase-matching condition between interacting pump and probe beams.

Ridge waveguides in coupled geometry. Our approach allowed us to observe the mode splitting inherent to coupled systems and locally probe the coupling lengths with an accuracy of ±50 nm.

Waveguide phased arrays for optical beam-steering. We have achieved continuous beam steering in two perpendicular directions by using both thermo-optical and wavelength tuning mechanism.

Bulk photonic crystal devices designed for operation in the self-collimation regime. Two-dimensional dispersion map near the top of the dielectric band was reconstructed, allowing us to observe both the regime of self-collimation and self-focusing, as well as the effect of enhanced back-scattering in the proximity of the band edge.

Photonic crystal coupled cavity waveguides (CCWs), based on heterostructure or L3 cavities. We studied the physics of CCW dispersion band formation as well as the inherent radiation loss of the coupled-cavity chains.

Photonic crystal line defect waveguides. Light propagation in Si air-bridge membrane W1 waveguides and specially tailored line defect waveguides was studied in the slow light regime. In particular, coupling efficiency into slow-light modes and modification of the signal propagation due to disorder were addressed.

Slotted photonic crystal waveguides and cavities. An ongoing project which aims to realize structures highly sensitive to variations in surrounding low-index environment. Up to date, a miniature high precision sensor based on an air-slot cavity was realized and successfully tested for optical gas sensing.

All seven projects listed above have led to original results and a majority of them resulted in a publication. Nevertheless, there are still several intriguing tasks to be pursued in the future:

In the first place, the deep physical understanding acquired about light propagation in coupled cavity waveguides would allow us to design a structure with both flat transmission and good slow light performance. Utilizing a more suitable high-Q cavity design together with careful optimization of the CCW coupling scheme should do the job. Time-delay measurements of short optical pulses would follow, in order to confirm the measured group velocity and assess the sample performance in real applications.

Besides standard coupled cavity chains, it would be of a large interest to realize coupled-cavity waveguides based on air-slot cavities treated in the last chapter of this thesis. Filling the hollow core with a nonlinear or gain material would allow for light-matter enhancement due to slow light effect, which would be intensified by strong overlap of the field and matter that is present in such devices.

For the same reason why the hollow-core photonic crystal structures are advantageous for optical sensing and nonlinear applications, namely for having the majority of the optical field within low-index contrast slit, they should be well suited as an efficient trap for

nanoparticles. The designed and successfully characterized hollow-core photonic crystal cavities are yet to prove their potential for optical trapping experiments and, after functionalization of their side-walls, for specific bio/nano object detection. The latter project is already under development within our working group.

Last but not least, there is still a lot of space to pursue the study of disorder-induced power dissipation in slow light structures. More specifically, we need to increase the accuracy of detection of the back-scattered signal: remove the parasitic Fabry-Perot resonances at the sample facets by deposition of antireflection coating; and design adequate volume grating probes that would provide optical signal proportional to the amount of light in the structure, independently of the profile of the optical mode. Equally, averaging over several realizations of disorder should be done to account for more quantitative experimental results. Beyond, precise knowledge of physics of energy dissipation in the slow-light regime may help to identify the photonic designs truly suitable for practical slow light applications.

To conclude, experimental results reported in this thesis represent a fraction of recent achievement in the field of integrated photonics, suggesting that optical nanostructures including photonic crystals are slowly, but surely becoming a mature technology. Direct comparison of the state-of-the art devices with structures available only five years ago show an enormous progress that has been made in this field. Although there are still many questions to be answered, improvements to be made and new ideas to be pursued, it is equally the right time to intensify the technology transfer from basic research towards practical applications.

Bibliography

[1] B. Analui, D. Guckenberger, D. Kucharski, and A. Narasimha, "A fully integrated 20-Gb/s optoelectronic transceiver implemented in a standard $0.13-\mu$m CMOS SOI technology," *Solid-State Circuits, IEEE Journal of*, vol. 41, pp. 2945 –2955, 2006.

[2] http://www.intel.com/pressroom/archive/releases/2010/20100727comp_sm.htm.

[3] Y. Vlasov, "Silicon photonics for next generation computing systems," in *European Conference on Optical Communications (ECOC)*, (Brussels, Belgium), 2008.

[4] D. Liang and J. E. Bowers, "Recent progress in lasers on silicon," *Nat. Photon.*, vol. 4, pp. 511–517, 2010.

[5] H. Rong, S. Xu, Y.-H. Kuo, V. Sih, O. Cohen, O. Raday, and M. Paniccia, "Low-threshold continuous-wave Raman silicon laser," *Nat. Photon.*, vol. 1, pp. 232–237, 2007.

[6] B. E. A. Saleh and M. C. Teich, *Fundamentals of Photonics*. A John Wiley & Sons, Inc., 2 ed., 2007.

[7] W. Bogaerts, R. Baets, P. Dumon, V. Wiaux, S. Beckx, D. Taillaert, B. Luyssaert, J. V. Campenhout, P. Bienstman, and D. V. Thourhout, "Nanophotonic waveguides in silicon-on-insulator fabricated with CMOS technology," *J. Lightwave Technol.*, vol. 23, p. 401, 2005.

[8] P. Dumon, G. Priem, L. R. Nunes, W. Bogaerts, D. V. Thourhout, P. Bienstman, T. K. Liang, M. Tsuchiya, P. Jaenen, S. Beckx, J. Wouters, and R. Baets, "Linear and nonlinear nanophotonic devices based on silicon-on-insulator wire waveguides," *Jpn. J. Appl. Phys.*, vol. 45, pp. 6589–6602, 2006.

[9] H. Yamada, T. Chu, S. Ishida, and Y. Arakawa, "Optical directional coupler based on Si-wire waveguides," *IEEE Photonics Technol. Lett.*, vol. 17, pp. 585 –587, 2005.

[10] D. M. Beggs, T. P. White, L. O'Faolain, and T. F. Krauss, "Ultracompact and low-power optical switch based on silicon photonic crystals," *Opt. Lett.*, vol. 33, pp. 147–149, 2008.

[11] J. Jágerská, N. L. Thomas, R. Houdré, D. M. Beggs, D. O'Brien, and T. F. Krauss, "Coupling length of silicon-on-insulator directional couplers probed by Fourier-space imaging," *Appl. Phys. Lett.*, vol. 92, p. 151106, 2008.

[12] Y. Vlasov, W. M. J. Green, and F. Xia, "High-throughput silicon nanophotonic wavelength-insensitive switch for on-chip optical networks," *Nat Photon*, vol. 2, pp. 242–246, 2008.

[13] V. R. Almeida, Q. Xu, C. A. Barrios, and M. Lipson, "Guiding and confining light in void nanostructure," *Opt. Lett.*, vol. 29, pp. 1209–1211, 2004.

[14] Q. Xu, V. R. Almeida, R. R. Panepucci, and M. Lipson, "Experimental demonstration of guiding and confining light in nanometer-size low-refractive-index material," *Opt. Lett.*, vol. 29, pp. 1626–1628, 2004.

[15] P. Cheben, P. J. Bock, J. H. Schmid, J. Lapointe, S. Janz, D.-X. Xu, A. Densmore, A. Delâge, B. Lamontagne, and T. J. Hall, "Refractive index engineering with subwavelength gratings for efficient microphotonic couplers and planar waveguide multiplexers," *Opt. Lett.*, vol. 35, pp. 2526–2528, 2010.

[16] P. Cheben, D.-X. Xu, S. Janz, and A. Densmore, "Subwavelength waveguide grating for mode conversion and light coupling in integrated optics," *Opt. Express*, vol. 14, pp. 4695–4702, 2006.

[17] P. J. Bock, P. Cheben, J. H. Schmid, J. Lapointe, A. Delâge, D.-X. Xu, S. Janz, A. Densmore, and T. J. Hall, "Subwavelength grating crossings for silicon wire waveguides," *Opt. Express*, vol. 18, no. 15, pp. 16146–16155, 2010.

[18] S. Hughes, L. Ramunno, E. Kuramochi, T. Watanabe, A. Shinya, and M. Notomi, "Disorder-induced optical scattering loss in planar photonic crystal waveguides: Theory and experiment," in *Conference on Lasers and Electro-Optics/Quantum Electronics and Laser Science and Photonic Applications Systems Technologies*, p. QWD4, Optical Society of America, 2005.

[19] H. Kosaka, T. Kawashima, A. Tomita, M. Notomi, T. Tamamura, T. Sato, and S. Kawakami, "Self-collimating phenomena in photonic crystals," *Appl. Phys. Lett.*, vol. 74, pp. 1212–1214, 1999.

[20] J. P. Dowling, M. Scalora, M. J. Bloemer, and C. M. Bowden, "The photonic band edge laser: A new approach to gain enhancement," *Journal of Applied Physics*, vol. 75, pp. 1896–1899, 1994.

[21] M. Notomi, E. Kuramochi, and T. Tanabe, "Large-scale arrays of ultrahigh-Q coupled nanocavities," *Nat. Photon.*, vol. 2, pp. 741–747, 2008.

[22] X. Fan, I. M. White, S. I. Shopova, H. Zhu, J. D. Suter, and Y. Sun, "Sensitive optical biosensors for unlabeled targets: A review," *Analytica Chimica Acta*, vol. 620, pp. 8 – 26, 2008.

[23] E. Ozbay, "Plasmonics: Merging Photonics and Electronics at Nanoscale Dimensions," *Science*, vol. 311, pp. 189–193, 2006.

[24] `http://www.physics.ucsd.edu/~tmurphy/apollo/basics.html`.

[25] E. Hecht, *Optics*. Addison-Wesley, 4 ed., 2002.

[26] W. Bogaerts, D. Taillaert, P. Dumon, D. V. Thourhout, R. Baets, and E. Pluk, "A polarization-diversity wavelength duplexer circuit in silicon-on-insulator photonic wires," *Opt. Express*, vol. 15, pp. 1567–1578, 2007.

[27] V. R. Almeida, R. R. Panepucci, and M. Lipson, "Nanotaper for compact mode conversion," *Opt. Lett.*, vol. 28, pp. 1302–1304, 2003.

[28] Q. V. Tran, S. Combrié, P. Colman, and A. D. Rossi, "Photonic crystal membrane waveguides with low insertion losses," *Applied Physics Letters*, vol. 95, p. 061105, 2009.

[29] F. Grillot, L. Vivien, S. Laval, and E. Cassan, "Propagation loss in single-mode ultra-small square silicon-on-insulator optical waveguides," *J. Lightwave Technol.*, vol. 24, p. 891, 2006.

[30] C. G. Poulton, C. Koos, M. Fujii, A. Pfrang, T. Schimmel, J. Leuthold, and W. Freude, "Radiation modes and roughness loss in high index-contrast waveguides," *Selected Topics in Quantum Electronics, IEEE Journal of*, vol. 12, pp. 1306 –1321, 2006.

[31] Y. Vlasov and S. McNab, "Losses in single-mode silicon-on-insulator strip waveguides and bends," *Opt. Express*, vol. 12, pp. 1622–1631, 2004.

[32] G. Roelkens, D. V. Thourhout, and R. Baets, "High efficiency silicon-on-insulator grating coupler based on a poly-silicon overlay," *Opt. Express*, vol. 14, pp. 11622–11630, 2006.

[33] C. Kittel, *Introduction to Solid State Physics.* John Wiley & Sons, Inc., 7 ed., 1996.

[34] J. D. Joannopoulos, S. G. Johnson, J. N. Winn, and R. D. Meade, *Photonic Crystals: Molding the Flow of Light.* Princeton University Press, 2 ed., 2008.

[35] D. Leuenberger, *Experimental and numerical investigation of two-dimensional photonic crysals dor applications in integrated optics.* PhD thesis, Ecole Polytechnique Fédérale de Lausanne (EPFL), 2004.

[36] D. Prather, S. Shi, J. Murakowski, G. Schneider, A. Sharkawy, C. Chen, and B. Miao, "Photonic crystal structures and applications: Perspective, overview, and development," *IEEE J. Sel. Top. Quant. Electron.*, vol. 12, pp. 1416 –1437, 2006.

[37] V. P. Bykov, "Spontaneous emission in a periodic structure," *Soviet Journal of Experimental and Theoretical Physics*, vol. 35, pp. 269–273, 1972.

[38] H. Matsubara, S. Yoshimoto, H. Saito, J. Yue, Y. Tanaka, and S. Noda, "GaN photonic-crystal surface-emitting laser at blue-violet wavelengths," *Science*, vol. 319, pp. 445–447, 2008.

[39] O. Painter, R. K. Lee, A. Scherer, A. Yariv, J. D. O'Brien, P. D. Dapkus, and I. Kim, "Two-Dimensional Photonic Band-Gap Defect Mode Laser," *Science*, vol. 284, pp. 1819–1821, 1999.

[40] H. Zhang, L. A. Dunbar, G. Scalari, R. Houdré, and J. Faist, "Terahertz photonic crystal quantum cascade lasers," *Opt. Express*, vol. 15, pp. 16818–16827, 2007.

[41] H. Kosaka, T. Kawashima, A. Tomita, M. Notomi, T. Tamamura, T. Sato, and S. Kawakami, "Photonic crystals for micro lightwave circuits using wavelength-dependent angular beam steering," *Appl. Phys. Lett.*, vol. 74, pp. 1370–1372, 1999.

[42] M. Notomi, "Theory of light propagation in strongly modulated photonic crystals: Refractionlike behavior in the vicinity of the photonic band gap," *Phys. Rev. B*, vol. 62, pp. 10696–10705, 2000.

[43] J. Canning, N. Skivesen, M. Kristensen, L. H. Frandsen, A. Lavrinenko, C. Martelli, and A. Tetu, "Mapping the broadband polarization properties of linear 2D SOI photonic crystal waveguides," *Opt. Express*, vol. 15, pp. 15603–15614, 2007.

[44] E. Kuramochi, M. Notomi, S. Mitsugi, A. Shinya, T. Tanabe, and T. Watanabe, "Ultrahigh-Q photonic crystal nanocavities realized by the local width modulation of a line defect," *Appl. Phys. Lett.*, vol. 88, p. 041112, 2006.

[45] T. Asano, B.-S. Song, Y. Akahane, and S. Noda, "Ultrahigh-Q nanocavities in two-dimensional photonic crystal slabs," *IEEE J. Sel. Top. Quant. Electron.*, vol. 12, no. 6, pp. 1123 –1134, 2006.

[46] K. Nozaki, T. Tanabe, A. Shinya, S. Matsuo, T. Sato, H. Taniyama, and M. Notomi, "Sub-femtojoule all-optical switching using a photonic-crystal nanocavity," *Nat. Photon.*, vol. 4, pp. 477–483, 2010.

[47] S. Noda, M. Fujita, and T. Asano, "Spontaneous-emission control by photonic crystals and nanocavities," *Nat. Photon.*, vol. 1, pp. 449–458, 2007.

[48] J. Bravo-Abad, A. Rodriguez, P. Bermel, S. G. Johnson, J. D. Joannopoulos, and M. Soljacic, "Enhanced nonlinear optics in photonic-crystal microcavities," *Opt. Express*, vol. 15, pp. 16161–16176, 2007.

[49] M. Lončar, A. Scherer, and Y. Qiu, "Photonic crystal laser sources for chemical detection," *Appl. Phys. Lett.*, vol. 82, pp. 4648–4650, 2003.

[50] J. Jágerská, H. Zhang, Z. Diao, N. L. Thomas, and R. Houdré, "Refractive index sensing with an air-slot photonic crystal nanocavity," *Opt. Lett.*, vol. 35, pp. 2523–2525, 2010.

[51] M. R. Lee and P. M. Fauchet, "Nanoscale microcavity sensor for single particle detection," *Opt. Lett.*, vol. 32, pp. 3284–3286, 2007.

[52] A. Yariv, Y. Xu, R. K. Lee, and A. Scherer, "Coupled-resonator optical waveguide: a proposal and analysis," *Opt. Lett.*, vol. 24, pp. 711–713, 1999.

[53] N. Stefanou and A. Modinos, "Impurity bands in photonic insulators," *Phys. Rev. B*, vol. 57, pp. 12127–12133, 1998.

[54] L. O'Faolain, X. Yuan, D. McIntyre, S. Thoms, H. Chong, R. De La Rue, and T. Krauss, "Low-loss propagation in photonic crystal waveguides," *Electronics Letters*, vol. 42, pp. 1454 –1455, 2006.

[55] H. Benisty, S. Olivier, C. Weisbuch, M. Agio, M. Kafesaki, C. Soukoulis, M. Qiu, M. Swillo, A. Karlsson, B. Jaskorzynska, A. Talneau, R. Moosburger, M. Kamp, A. Forchel, R. Ferrini, R. Houdré, and U. Oesterle, "Models and measurements for the transmission of submicron-width waveguide bends defined in two-dimensional photonic crystals," *Quantum Electronics, IEEE Journal of*, vol. 38, pp. 770 –785, 2002.

[56] S. H. Tao, M. B. Yu, J. F. Song, Q. Fang, R. Yang, G. Q. Lo, and D. L. Kwong, "Design and fabrication of a line-defect bend sandwiched with air trenches in a photonic crystal platform," *Appl. Phys. Lett.*, vol. 92, p. 031113, 2008.

[57] T. Baba, "Slow light in photonic crystals," *Nat. Photon.*, vol. 2, pp. 465–473, 2008.

[58] J. Li, T. P. White, L. O'Faolain, A. Gomez-Iglesias, and T. F. Krauss, "Systematic design of flat band slow light in photonic crystal waveguides," *Opt. Express*, vol. 16, pp. 6227–6232, 2008.

[59] L. H. Frandsen, A. V. Lavrinenko, J. Fage-Pedersen, and P. I. Borel, "Photonic crystal waveguides with semi-slow light and tailored dispersion properties," *Opt. Express*, vol. 14, pp. 9444–9450, 2006.

[60] D. Mori and T. Baba, "Wideband and low dispersion slow light by chirped photonic crystal coupled waveguide," *Opt. Express*, vol. 13, pp. 9398–9408, 2005.

[61] T. Kawasaki, D. Mori, and T. Baba, "Experimental observation of slow light in photonic crystal coupled waveguides," *Opt. Express*, vol. 15, pp. 10274–10281, 2007.

[62] E. Yablonovitch and T. J. Gmitter, "Photonic band structure: the face-centered-cubic case," *J. Opt. Soc. Am. A*, vol. 7, pp. 1792–1800, 1990.

[63] K. M. Leung and Y. F. Liu, "Full vector wave calculation of photonic band structures in face-centered-cubic dielectric media," *Phys. Rev. Lett.*, vol. 65, pp. 2646–2649, 1990.

[64] E. Yablonovitch and K. M. Leung, "Hope for photonic bandgaps," *Nature*, vol. 351, pp. 278–278, 1991.

[65] C. C. Cheng, V. Arbet-Engels, A. Scherer, and E. Yablonovitch, "Nanofabricated three dimensional photonic crystals operating at optical wavelengths," *Physica Scripta*, vol. 1996, p. 17, 1996.

[66] M. Maldovan and E. L. Thomas, "Diamond-structured photonic crystals," *Nat. Mater.*, vol. 3, pp. 593–600, 2004.

[67] S. Y. Lin, J. G. Fleming, D. L. Hetherington, B. K. Smith, R. Biswas, K. M. Ho, M. M. Sigalas, W. Zubrzycki, S. R. Kurtz, and J. Bur, "A three-dimensional photonic crystal operating at infrared wavelengths," *Nature*, vol. 394, pp. 251–253, 1998.

[68] S. Noda, K. Tomoda, N. Yamamoto, and A. Chutinan, "Full Three-Dimensional Photonic Bandgap Crystals at Near-Infrared Wavelengths," *Science*, vol. 289, pp. 604–606, 2000.

[69] Y. A. Vlasov, X.-Z. Bo, J. C. Sturm, and D. J. Norris, "On-chip natural assembly of silicon photonic bandgap crystals," *Nature*, vol. 414, pp. 289–293, 2001.

[70] K. Ho, C. Chan, C. Soukoulis, R. Biswas, and M. Sigalas, "Photonic band gaps in three dimensions: New layer-by-layer periodic structures," *Solid State Communications*, vol. 89, pp. 413 – 416, 1994.

[71] S. A. Rinne, F. Garcia-Santamaria, and P. V. Braun, "Embedded cavities and waveguides in three-dimensional silicon photonic crystals," *Nat. Photon.*, vol. 2, pp. 52–56, 2008.

[72] K. Aoki, D. Guimard, M. Nishioka, M. Nomura, S. Iwamoto, and Y. Arakawa, "Coupling of quantum-dot light emission with a three-dimensional photonic-crystal nanocavity," *Nat. Photon.*, vol. 2, pp. 688–692, 2008.

[73] M. Plihal and A. A. Maradudin, "Photonic band structure of two-dimensional systems: The triangular lattice," *Phys. Rev. B*, vol. 44, pp. 8565–8571, 1991.

[74] K. M. Ho, C. T. Chan, and C. M. Soukoulis, "Existence of a photonic gap in periodic dielectric structures," *Phys. Rev. Lett.*, vol. 65, pp. 3152–3155, 1990.

[75] S. Shi, C. Chen, and D. W. Prather, "Revised plane wave method for dispersive material and its application to band structure calculations of photonic crystal slabs," *Appl. Phys. Lett.*, vol. 86, p. 043104, 2005.

[76] L. C. Andreani and D. Gerace, "Photonic-crystal slabs with a triangular lattice of triangular holes investigated using a guided-mode expansion method," *Phys. Rev. B*, vol. 73, p. 235114, 2006.

[77] V. Zabelin, *Numerical investigation of two-dimensional photonic crystal optical properties, design and analysis of photonic crystal based structures.* PhD thesis, Ecole Polytechnique Fédérale de Lausanne (EPFL), 2009.

[78] A. S. Sudbo, "Improved formulation of the film mode matching method for mode field calculations in dielectric waveguides," *Pure and Applied Optics: Journal of the European Optical Society Part A*, vol. 3, p. 381, 1994.

[79] J. Cardenas, C. B. Poitras, J. T. Robinson, K. Preston, L. Chen, and M. Lipson, "Low loss etchless silicon photonic waveguides," *Opt. Express*, vol. 17, pp. 4752–4757, 2009.

[80] J. Tian, W. Yan, Y. Liu, J. Luo, D. Zhang, Z. Li, and M. Qiu, "Optical quality improvement of si photonic devices fabricated by focused-ion-beam milling," *J. Lightwave Technol.*, vol. 27, pp. 4306–4310, 2009.

[81] W. Hopman, F. Ay, W. Hu, V. Gadgil, L. Kuipers, M. Pollnau, and R. de Ridder, "Focused ion beam milling strategies of photonic crystal structures in silicon," in *Proceedings European Conference on Integrated Optics (ECIO 2007)*, (Copenhagen), pp. FA1–FA1/1, 2007.

[82] J. Schrauwen, F. Van Laere, D. Van Thourhout, and R. Baets, "Focused-ion-beam fabrication of slanted grating couplers in silicon-on-insulator waveguides," *Photonics Technology Letters, IEEE*, vol. 19, pp. 816 –818, 2007.

[83] http://www.epixfab.eu/technology/imec_std/.

[84] J. Jágerská, N. L. Thomas, R. Houdré, J. Bolten, C. Moormann, T. Wahlbrink, J. Čtyroký, M. Waldow, and M. Först, "Dispersion properties of silicon nanophotonic waveguides investigated with Fourier optics," *Opt. Lett.*, vol. 32, pp. 2723–2725, 2007.

[85] http://cmi.epfl.ch/ebeam/Electrons,_resists_and_substrates.php.

[86] http://en.wikipedia.org/wiki/Deep_reactive-ion_etching.

[87] A. Talneau, K. H. Lee, S. Guilet, and I. Sagnes, "Efficient coupling to W1 photonic crystal waveguide on InP membrane through suspended access guides," *Applied Physics Letters*, vol. 92, p. 061105, 2008.

[88] A. Talneau, K. Lee, and I. Sagnes, "Spectral behavior and dispersionless propagation in indium phosphide suspended photonic wires," *Photonics Technology Letters, IEEE*, vol. 21, pp. 775 –777, 2009.

[89] H. Zhang, *Development of terahertz photonic crystal quantum cascade lasers and investigation on IIIV & SOI photonic structures at near-infrared wavelength*. PhD thesis, Ecole Polytechnique Fédérale de Lausanne (EPFL), 2010.

[90] J. P. Hugonin, P. Lalanne, T. P. White, and T. F. Krauss, "Coupling into slow-mode photonic crystal waveguides," *Opt. Lett.*, vol. 32, pp. 2638–2640, 2007.

[91] W. Hellmich and P. Deimel, "Optimal ar-coating for optical waveguide devices," *Lightwave Technology, Journal of*, vol. 10, no. 4, pp. 469 –476, 1992.

[92] M. Notomi, K. Yamada, A. Shinya, J. Takahashi, C. Takahashi, and I. Yokohama, "Extremely large group-velocity dispersion of line-defect waveguides in photonic crystal slabs," *Phys. Rev. Lett.*, vol. 87, p. 253902, 2001.

[93] Y. A. Vlasov, M. O'Boyle, H. F. Hamann, and S. J. McNab, "Active control of slow light on a chip with photonic crystal waveguides," *Nature*, vol. 438, pp. 65–69, 2005.

[94] A. Gomez-Iglesias, D. O'Brien, L. O'Faolain, A. Miller, and T. F. Krauss, "Direct measurement of the group index of photonic crystal waveguides via Fourier transform spectral interferometry," *Applied Physics Letters*, vol. 90, p. 261107, 2007.

[95] A. Parini, P. Hamel, A. D. Rossi, S. Combrié, N.-V.-Q. Tran, Y. Gottesman, R. Gabet, A. Talneau, Y. Jaouën, and G. Vadalà, "Time-wavelength reflectance maps of photonic crystal waveguides: A new view on disorder-induced scattering," *J. Lightwave Technol.*, vol. 26, pp. 3794–3802, 2008.

[96] S. Combrié, N.-V.-Q. Tran, E. Weidner, A. De Rossi, S. Cassette, P. Hamel, Y. Jaouen, R. Gabet, and A. Talneau, "Investigation of group delay, loss, and disorder in a photonic crystal waveguide by low-coherence reflectometry," *Applied Physics Letters*, vol. 90, pp. 231104 –231104–3, 2007.

[97] R. Jacobsen, A. Lavrinenko, L. Frandsen, C. Peucheret, B. Zsigri, G. Moulin, J. Fage-Pedersen, and P. Borel, "Direct experimental and numerical determination of extremely high group indices in photonic crystal waveguides," *Opt. Express*, vol. 13, pp. 7861–7871, 2005.

[98] S. Combrié, A. De Rossi, L. Morvan, S. Tonda, S. Cassette, D. Dolfi, and A. Talneau, "Time-delay measurement in singlemode, low-loss photonic crystal waveguides," *Electronics Letters*, vol. 42, pp. 86 – 88, 2006.

[99] Y. Nazirizadeh, J. Müller, U. Geyer, D. Schelle, E.-B. Kley, A. Tünnermann, U. Lemmer, and M. Gerken, "Optical characterization of photonic crystal slabs using orthogonally oriented polarization filters," *Opt. Express*, vol. 16, pp. 7153–7160, 2008.

[100] M. Galli, D. Bajoni, M. Belotti, F. Paleari, M. Patrini, G. Guizzetti, D. Gerace, M. Agio, L. Andreani, D. Peyrade, and Y. Chen, "Measurement of photonic mode dispersion and linewidths in silicon-on-insulator photonic crystal slabs," *Selected Areas in Communications, IEEE Journal on*, vol. 23, pp. 1402 – 1410, 2005.

[101] M. W. Lee, C. Grillet, C. G. Poulton, C. Monat, C. L. Smith, E. Mägi, D. Freeman, S. Madden, B. Luther-Davies, and B. J. Eggleton, "Characterizing photonic crystal waveguides withan expanded k-space evanescent coupling technique," *Opt. Express*, vol. 16, pp. 13800–13808, 2008.

[102] R. J. P. Engelen, T. Karle, H. Gersen, J. Korterik, T. Krauss, L. Kuipers, and N. van Hulst, "Local probing of Bloch mode dispersion in a photonic crystal waveguide," *Opt. Express*, vol. 13, pp. 4457–4464, 2005.

[103] H. Gersen, T. J. Karle, R. J. P. Engelen, W. Bogaerts, J. P. Korterik, N. F. van Hulst, T. F. Krauss, and L. Kuipers, "Direct observation of Bloch harmonics and negative phase velocity in photonic crystal waveguides," *Phys. Rev. Lett.*, vol. 94, p. 123901, 2005.

[104] K. Okamoto, M. Lončar, T. Yoshie, A. Scherer, Y. Qiu, and P. Gogna, "Near-field scanning optical microscopy of photonic crystal nanocavities," *Applied Physics Letters*, vol. 82, pp. 1676 –1678, 2003.

[105] J. T. Robinson, S. F. Preble, and M. Lipson, "Imaging highly confined modes in submicron scale silicon waveguides using transmission-based near-field scanning optical microscopy," *Opt. Express*, vol. 14, pp. 10588–10595, 2006.

[106] M. Burresi, R. J. P. Engelen, A. Opheij, D. van Oosten, D. Mori, T. Baba, and L. Kuipers, "Observation of polarization singularities at the nanoscale," *Phys. Rev. Lett.*, vol. 102, p. 033902, 2009.

[107] E. Flück, M. Hammer, A. M. Otter, J. P. Korterik, L. Kuipers, and N. F. van Hulst, "Amplitude and phase evolution of optical fields inside periodic photonic structures," *J. Lightwave Technol.*, vol. 21, p. 1384, 2003.

[108] M. D. Settle, R. J. P. Engelen, M. Salib, A. Michaeli, L. Kuipers, and T. F. Krauss, "Flatband slow light in photonic crystals featuring spatial pulse compression and terahertz bandwidth," *Opt. Express*, vol. 15, pp. 219–226, 2007.

[109] M. L. M. Balistreri, H. Gersen, J. P. Korterik, L. Kuipers, and N. F. van Hulst, "Tracking Femtosecond Laser Pulses in Space and Time," *Science*, vol. 294, pp. 1080–1082, 2001.

[110] J. W. Goodman, *Introduction to Fourier Optics*. Roberts & Company Publishers, 3 ed., 2005.

[111] P. Fiala and I. Richter, *Furierovská optika a optické zpracování signálů*. Praha: Vydavatelství ČVUT, 1 ed., 2004.

[112] N. L. Thomas, H. Zhang, Z. Diao, and R. Houdré, "Experimental control of the far-field and Q factor of silicon photonic crystals cavities with a top mirror," in *Ninth International Conference on Photonic and Electromagnetic Structures PECS-IX*, (Granada, Spain), 2010.

[113] N. Le Thomas, V. Zabelin, R. Houdré, M. V. Kotlyar, and T. F. Krauss, "Influence of residual disorder on the anticrossing of Bloch modes probed in k space," *Phys. Rev. B*, vol. 78, p. 125301, 2008.

[114] Y. Akahane, T. Asano, B.-S. Song, and S. Noda, "High-Q photonic nanocavity in a two-dimensional photonic crystal," *Nature*, vol. 425, pp. 944–947, 2003.

[115] S. L. Portalupi, M. Galli, C. Reardon, T. Krauss, L. O'Faolain, L. C. Andreani, and D. Gerace, "Planar photonic crystal cavities with far-field optimization for high coupling efficiency and quality factor," *Opt. Express*, vol. 18, pp. 16064–16073, 2010.

[116] N. Le Thomas, R. Houdré, D. M. Beggs, and T. F. Krauss, "Fourier space imaging of light localization at a photonic band-edge located below the light cone," *Phys. Rev. B*, vol. 79, p. 033305, 2009.

[117] D. G. Lucio Claudio Andreani, "Light–matter interaction in photonic crystal slabs," *Phys. Stat. Sol. (b)*, vol. 244, pp. 3528–3539, 2007.

[118] S. Mazoyer, J. P. Hugonin, and P. Lalanne, "Disorder-induced multiple scattering in photonic-crystal waveguides," *Phys. Rev. Lett.*, vol. 103, p. 063903, 2009.

[119] N. L. Thomas, R. Houdré, M. V. Kotlyar, D. O'Brien, and T. F. Krauss, "Exploring light propagating in photonic crystals with Fourier optics," *J. Opt. Soc. Am. B*, vol. 24, pp. 2964–2971, 2007.

[120] R. Dekker, A. Driessen, T. Wahlbrink, C. Moormann, J. Niehusmann, and M. Först, "Ultrafast kerr-induced all-optical wavelength conversion in silicon waveguides using 1.55 μm femtosecond pulses," *Opt. Express*, vol. 14, pp. 8336–8346, 2006.

[121] M. A. Foster, A. C. Turner, J. E. Sharping, B. S. Schmidt, M. Lipson, and A. L. Gaeta, "Broad-band optical parametric gain on a silicon photonic chip," *Nature*, vol. 441, pp. 960–963, 2006.

[122] C. Koos, P. Vorreau, T. Vallaitis, P. Dumon, W. Bogaerts, R. Baets, B. Esembeson, I. Biaggio, T. Michinobu, F. Diederich, W. Freude, and J. Leuthold, "All-optical high-speed signal processing with silicon-organic hybrid slot waveguides," *Nat. Photon.*, vol. 3, pp. 216–219, 2009.

[123] E. Dulkeith, F. Xia, L. Schares, W. M. J. Green, and Y. A. Vlasov, "Group index and group velocity dispersion in silicon-on-insulator photonic wires," *Opt. Express*, vol. 14, pp. 3853–3863, 2006.

[124] A. C. Turner, M. A. Foster, R. Salem, A. L. Gaeta, and M. Lipson, "Frequency conversion over two-thirds of an octave in silicon nanowaveguides," *Opt. Express*, vol. 18, pp. 1904–1908, 2010.

[125] D. Marcuse, "Directional couplers made of nonidentical asymmetric slabs. part i: Synchronous couplers," *Lightwave Technology, Journal of*, vol. 5, pp. 113 – 118, 1987.

[126] D. Marcuse, *Theory of Dielectric Optical Waveguides*. Academic Press, 2 ed., 1991.

[127] A. Yariv, "Coupled-mode theory for guided-wave optics," *Quantum Electronics, IEEE Journal of*, vol. 9, pp. 919 – 933, 1973.

[128] P. Bienstman, *Rigorous and Efficient Modeling of Wavelength Scale Photonic Components*. PhD thesis, Ghent University, 2000.

[129] F. Vasey, F. K. Reinhart, R. Houdré, and J. M. Stauffer, "Spatial optical beam steering with an AlGaAs integrated phased array," *Appl. Opt.*, vol. 32, pp. 3220–3232, 1993.

[130] Y. Kurosaka, S. Iwahashi, Y. Liang, K. Sakai, E. Miyai, W. Kunishi, D. Ohnishi, and S. Noda, "On-chip beam-steering photonic-crystal lasers," *Nat. Photon.*, vol. 4, pp. 447–450, 2010.

[131] A. F. Koenderink, M. Megens, G. van Soest, W. L. Vos, and A. Lagendijk, "Enhanced backscattering from photonic crystals," *Physics Letters A*, vol. 268, pp. 104 – 111, 2000.

[132] T. F. Krauss, L. O'Faolain, S. Schulz, D. M. Beggs, F. Morichetti, A. Canciamilla, M. Torregiani, A. Melloni, S. Mazoyer, P. Lalanne, A. Samarelli, M. Sorel, and R. D. L. Rue, "Understanding the rich physics of light propagation in slow photonic crystal waveguides," in *Advances in Slow and Fast Light III*, vol. 7612, p. 76120L, 2010.

[133] M. Patterson, S. Hughes, S. Combrié, N.-V.-Q. Tran, A. De Rossi, R. Gabet, and Y. Jaouën, "Disorder-induced coherent scattering in slow-light photonic crystal waveguides," *Phys. Rev. Lett.*, vol. 102, p. 253903, 2009.

[134] T. F. Krauss, "Slow light in photonic crystal waveguides," *Journal of Physics D: Applied Physics*, vol. 40, p. 2666, 2007.

[135] T. Baba and D. Mori, "Slow light engineering in photonic crystals," *Journal of Physics D: Applied Physics*, vol. 40, p. 2659, 2007.

[136] A. Y. Petrov and M. Eich, "Zero dispersion at small group velocities in photonic crystal waveguides," *Applied Physics Letters*, vol. 85, pp. 4866 –4868, 2004.

[137] T. P. White, L. C. Botten, C. M. de Sterke, K. B. Dossou, and R. C. McPhedran, "Efficient slow-light coupling in a photonic crystal waveguide without transition region," *Opt. Lett.*, vol. 33, pp. 2644–2646, 2008.

[138] Y. A. Vlasov and S. J. McNab, "Coupling into the slow light mode in slab-type photonic crystal waveguides," *Opt. Lett.*, vol. 31, pp. 50–52, 2006.

[139] P. Pottier, M. Gnan, and R. M. D. L. Rue, "Efficient coupling into slow-light photonic crystal channel guides using photonic crystal tapers," *Opt. Express*, vol. 15, pp. 6569–6575, 2007.

[140] C. M. de Sterke, K. B. Dossou, T. P. White, L. C. Botten, and R. C. McPhedran, "Efficient coupling into slow light photonic crystal waveguide without transition region: role of evanescent modes," *Opt. Express*, vol. 17, pp. 17338–17343, 2009.

[141] N. Le Thomas, H. Zhang, J. Jágerská, V. Zabelin, R. Houdré, I. Sagnes, and A. Talneau, "Light transport regimes in slow light photonic crystal waveguides," *Phys. Rev. B*, vol. 80, p. 125332, Sep 2009.

[142] V. Savona, "Electromagnetic modes of a disordered photonic crystal," *arXiv:1011.0109v1[physics.optics]*, 2010.

[143] N. L. Thomas and R. Houdré, "Group velocity and energy transport velocity near the band edge of a disordered coupled cavity waveguide: an analytical approach," *J. Opt. Soc. Am. B*, vol. 27, pp. 2095–2101, 2010.

[144] I. M. Lifshitz, "Energy spectrum structure and quantum states of disordered condensed systems," *Soviet Physics Uspekhi*, vol. 7, p. 549, 1965.

[145] N. L. Thomas, H. Zhang, Z. Diao, and R. Houdré, "Investigation of residual disorder in silicon planar photonic crystals structures waveguides," in *Ninth International Conference on Photonic and Electromagnetic Structures PECS-IX*, (Granada, Spain), 2010.

[146] S. A. Schulz, L. O'Faolain, D. M. Beggs, T. P. White, A. Melloni, and T. F. Krauss, "Dispersion engineered slow light in photonic crystals: a comparison," *Journal of Optics*, vol. 12, p. 104004, 2010.

[147] S. Hughes, L. Ramunno, J. F. Young, and J. E. Sipe, "Extrinsic optical scattering loss in photonic crystal waveguides: Role of fabrication disorder and photon group velocity," *Phys. Rev. Lett.*, vol. 94, p. 033903, 2005.

[148] E. Kuramochi, M. Notomi, S. Hughes, A. Shinya, T. Watanabe, and L. Ramunno, "Disorder-induced scattering loss of line-defect waveguides in photonic crystal slabs," *Phys. Rev. B*, vol. 72, no. 16, p. 161318, 2005.

[149] S. McNab, N. Moll, and Y. Vlasov, "Ultra-low loss photonic integrated circuit with membrane-type photonic crystal waveguides," *Opt. Express*, vol. 11, pp. 2927–2939, 2003.

[150] F. Xia, L. Sekaric, and Y. Vlasov, "Ultracompact optical buffers on a silicon chip," *Nat. Photon.*, vol. 1, pp. 65–71, 2007.

[151] Y. Hara, T. Mukaiyama, K. Takeda, and M. Kuwata-Gonokami, "Heavy photon states in photonic chains of resonantly coupled cavities with supermonodispersive microspheres," *Phys. Rev. Lett.*, vol. 94, p. 203905, 2005.

[152] M. Bayer, T. Gutbrod, A. Forchel, T. L. Reinecke, P. A. Knipp, R. Werner, and J. P. Reithmaier, "Optical demonstration of a crystal band structure formation," *Phys. Rev. Lett.*, vol. 83, pp. 5374–5377, 1999.

[153] S. Olivier, H. Benisty, C. Weisbuch, C. Smith, T. Krauss, and R. Houdré, "Coupled-mode theory and propagation losses in photonic crystal waveguides," *Opt. Express*, vol. 11, pp. 1490–1496, 2003.

[154] D. O'Brien, M. D. Settle, T. Karle, A. Michaeli, M. Salib, and T. F. Krauss, "Coupled photonic crystal heterostructure nanocavities," *Opt. Express*, vol. 15, pp. 1228–1233, 2007.

[155] D. Leuenberger, R. Ferrini, and R. Houdré, "Ab initio tight-binding approach to photonic-crystal based coupled cavity waveguides," *Journal of Applied Physics*, vol. 95, pp. 806–809, 2004.

[156] B. M. Möller, U. Woggon, and M. V. Artemyev, "Bloch modes and disorder phenomena in coupled resonator chains," *Phys. Rev. B*, vol. 75, p. 245327, 2007.

[157] T. Kamalakis and T. Sphicopoulos, "Analytical expressions for the resonant frequencies and modal fields of finite coupled optical cavity chains," *Quantum Electronics, IEEE Journal of*, vol. 41, pp. 1419 – 1425, 2005.

[158] M. L. Povinelli and S. Fan, "Radiation loss of coupled-resonator waveguides in photonic-crystal slabs," *Applied Physics Letters*, vol. 89, p. 191114, 2006.

[159] D. P. Fussell and M. M. Dignam, "Engineering the quality factors of coupled-cavity modes in photonic crystal slabs," *Applied Physics Letters*, vol. 90, p. 183121, 2007.

[160] J. Vučkoviè, M. Lončar, H. Mabuchi, and A. Scherer, "Optimization of the Q factor in photonic crystal microcavities," *Quantum Electronics, IEEE Journal of*, vol. 38, pp. 850 –856, 2002.

[161] Y. Akahane, T. Asano, B.-S. Song, and S. Noda, "Fine-tuned high-Q photonic-crystal nanocavity," *Opt. Express*, vol. 13, pp. 1202–1214, 2005.

[162] C. A. Balanis, *Anthenna Theory: Analysis and Design.* Hoboken: Wiley, 3 ed., 2005.

[163] B.-S. Song, S. Noda, T. Asano, and Y. Akahane, "Ultra-high-Q photonic double-heterostructure nanocavity," *Nat. Mater.*, vol. 4, pp. 207–210, 2005.

[164] T. Baba, T. Kawasaki, H. Sasaki, J. Adachi, and D. Mori, "Large delay-bandwidth product and tuning of slow light pulse in photonic crystal coupled waveguide," *Opt. Express*, vol. 16, pp. 9245–9253, 2008.

[165] A. D. Falco, L. O'Faolain, and T. F. Krauss, "Dispersion control and slow light in slotted photonic crystal waveguides," *Applied Physics Letters*, vol. 92, p. 083501, 2008.

[166] J. Gao, J. F. McMillan, M.-C. Wu, J. Zheng, S. Assefa, and C. W. Wong, "Demonstration of an air-slot mode-gap confined photonic crystal slab nanocavity with ultrasmall mode volumes," *Applied Physics Letters*, vol. 96, p. 051123, 2010.

[167] Z. Wang, N. Zhu, Y. Tang, L. Wosinski, D. Dai, and S. He, "Ultracompact low-loss coupler between strip and slot waveguides," *Opt. Lett.*, vol. 34, pp. 1498–1500, 2009.

[168] J. T. Robinson, C. Manolatou, L. Chen, and M. Lipson, "Ultrasmall mode volumes in dielectric optical microcavities," *Phys. Rev. Lett.*, vol. 95, no. 14, p. 143901, 2005.

[169] A. D. Falco, L. O'Faolain, and T. F. Krauss, "Chemical sensing in slotted photonic crystal heterostructure cavities," *Applied Physics Letters*, vol. 94, p. 063503, 2009.

[170] T. Yamamoto, M. Notomi, H. Taniyama, E. Kuramochi, Y. Yoshikawa, Y. Torii, and T. Kuga, "Design of a high-Q air-slot cavity based on a width-modulated line-defect in a photonic crystal slab," *Opt. Express*, vol. 16, pp. 13809–13817, 2008.

[171] R. Coccioli, M. Boroditsky, K. Kim, Y. Rahmat-Samii, and E. Yablonovitch, "Smallest possible electromagnetic mode volume in a dielectric cavity," *Optoelectronics, IEE Proceedings -*, vol. 145, pp. 391 –397, 1998.

[172] H. Aoki, "Critical behaviour of extended states in disordered systems," *Journal of Physics C: Solid State Physics*, vol. 16, p. L205, 1983.

[173] K. T. Hecht, *Quantum Mechanics.* Springer-Verlag New York, Inc., 2000.

[174] N. Mortensen, S. Xiao, and J. Pedersen, "Liquid-infiltrated photonic crystals: enhanced light-matter interactions for lab-on-a-chip applications," *Microfluidics and Nanofluidics*, vol. 4, pp. 117–127, 2008.

[175] A. C. Simmons, "The refractive index and Lorentz-Lorenz functions of propane, nitrogen and carbon-dioxide in the spectral range 15803-22002 cm^{-1} and at 944 cm^{-1}," *Optics Communications*, vol. 25, pp. 211 – 214, 1978.

[176] L'Air Liquide, Division Scientifique, *Encyclopédie des Gaz.* Elsevier, 1976.

[177] Y. Clergent, C. Durou, and M. Laurens, "Refractive index variations for argon, nitrogen, and carbon dioxide at $\lambda = 632.8$ nm (He–Ne laser light) in the range 288.15 K $\leq$ T $\leq$ 323.15 K, 0 < p < 110 kPa," *Journal of Chemical & Engineering Data*, vol. 44, pp. 197–199, 1999.

Acknowledgements

I wish to express my gratitude to those who made this thesis possible. In the first place, I thank my supervisor, Dr. Romuald Houdré, for his friendly guidance and continuous support throughout my research. Whenever I needed, he found time for discussion and didn't spare words of encouragement. I greatly appreciate his human nature and humor contributing to a relaxed atmosphere in the group, as well as his kind determination to propagate the French culture and language on his PhD students. Equally, I acknowledge him for careful proofreading of this manuscript.

In the second place, I am strongly indebted to Dr. Nicolas Le Thomas, an outstanding physicist and the true author of the Fourier-space imaging setup. I thank him for all passionate discussions and ready help throughout my thesis.

Furthermore, I would like to thank my friends and colleagues with whom a had the pleasure to work during the last four years. In particular, I thank Vasily Zabelin for introducing me into the complex theory of photonic crystals, Hua Zhang and Zhaolu Diao for providing top-quality samples and sharing their expertise in field of sample processing. Last but not least, my special thanks to Nicolas Descharmes and Ulagalandha Perumal Dharanipathy, exceptional people with an exceptional ability to create a pleasant atmosphere in the group.

I also acknowledge the team of techniciens, Damien Troillet, Nicolas Leiser and Roger Rochat for their high quality support and instantaneous help with numerous practical aspect of my experiments.

My thanks go also to William Whelan-Curtin and the whole group of prof. Thomas F. Krauss for fruitful collaboration and helpful discussions, prof. Anne Talneau for her kind support, and, in particular, to prof. Jiří Čtyroký, who stood at the beginning of my scientific career and ignited in me the light of passion for integrated optics that has finally become my field of expertise.

Finally, I thank my friends and relatives who make my life better every single day, especially Verena, Roland, Pavel and my family.

Publications

Peer-reviewed publications

. J. Jágerská, H. Zhang, Z. Diao, N. Le Thomas, and R. Houdré, "Refractive index sensing with an air-slot photonic crystal nanocavity," *Optics Letters*, vol. 35, pp. 2523-2525, 2010.

. N. Le Thomas, H. Zhang, J. Jágerská, V. Zabelin, R. Houdré, I. Sagnes, and A. Talneau, "Light transport regimes in slow light photonic crystal waveguides," *Phys. Rev. B*, vol. 80, p. 125332, 2009.

. J. Jágerská, H. Zhang, N. Le Thomas, and R. Houdré, "Radiation loss of photonic crystal coupled-cavity waveguides," *Appl. Phys. Lett.*, vol. 95, p. 111105, 2009.

. J. Jágerská, N. Le Thomas, V. Zabelin, R. Houdré, W. Bogaerts, P. Dumon, and R. Baets, "Experimental observation of slow mode dispersion in photonic crystal coupled-cavity waveguides," *Optics Letters*, vol. 34, pp. 359-361, 2009.

. K. Van Acoleyen, W. Bogaerts, J. Jágerská, N. Le Thomas, R. Houdré, and R. Baets, "Off-chip beam steering with a one-dimensional optical phased array on silicon-on-insulator," *Optics Letters*, vol. 34, pp. 1477-1479, 2009.

. J. Jágerská, N. Le Thomas, R. Houdré, D. M. Beggs, D. O'Brian, and T. F. Krauss, "Coupling length of Silicon-on-Insulator dierectional couplers probed by Fourier-space imaging," *Appl. Phys. Lett.*, vol. 92, p. 151106, 2008.

. J. Jágerská, N. Le Thomas, R. Houdré, J. Bolten, C. Moormann, T. Wahlbrink, J. Čtyroký, M. Waldow and M. Först, "Dispersion properties of silicon nanophotonic waveguides investigated with Fourier optics," *Opt. Lett.*, vol. 32, p. 2723, 2007.

Not related to the PhD thesis:

. F. Ondráček, J Jágerská, L. Salavcová, M. Míka, J. Špirková, and J. Čtyroký, "Er-Yb waveguide amplifiers in novel silicate glasses," *IEEE Journal Of Quantum Electronics*, vol. 44, pp. 536-541, 2008.

Conference presentations

. J. Jágerská, H. Zhang, Z. Diao, N. Le Thomas, U. P. Dharanipathy, and R. Houdré, "Air-Slot Photonic Crystal Cavity for High Precision Refractive Index Sensing," *Ninth International Conference on Photonic and Electromagnetic Crystal Structures (PECS-IX 2010)*, Granada, Spain, 2010.

. J. Jágerská, H. Zhang, N. Le Thomas, V. Zabelin, and R. Houdré, "Dispersion Properties of Photonic Crystal Coupled-Cavity Waveguides," *Lasers and Electro-Optics 2009 and European Quantum Electronics Conference (CLEO/Europe - EQEC 2009)*, München, Germany, 2009.

. J. Jágerská, N. Le Thomas, and R. Houdré, "Dispersion properties of photonic nanowires probed by Fourier-space imaging," *16th Polish-Slovak-Czech optical conference on wave and quantum aspects of contemporary optics*, Polanica-Zdrój, Poland, 2008.

. N. Le Thomas, J. Jágerská, H. Zhang, V. Zabelin, and R. Houdré, "Dispersion properties of photonic waveguide structures," *Photonics North*, Québec, Canada, 2009, invited communication.

. N. Le Thomas, J. Jágerská, H. Zhang, V. Zabelin, and R. Houdré, "Limits of slow light in actual photonic crystal structures," *International Laser Physics Workshop (LPHYS'09)*, Barcelona, Spain, 2009, invited communication.

. N. Le Thomas, J. Jágerská, H. Zhang, and R. Houdré, "Light transport and limits of slow light in real photonic crystal structures in the presence of residual disorder," *11th International Conference on Transparent Optical Networks (ICTON 2009)*, Azores, Portugal, 2009 (ICTON Tech. Dig.), invited communication.

. R. Houdré, N. Le Thomas, and J. Jágerská, "Characterisation of photonic crystal and nanophotonic devices with Fourier optics," *10th International Conference on Transparent Optical Networks (ICTON 2008)*, Athens, Greece, 2008; *ICTON Tech. Dig.*, 2, 5-6 (2008), invited communication.

. N. Le Thomas, J. Jágerská, H. Zhang, and R. Houdré, "Limits of slow light in real photonic crystal structures," *8th Workshop on Photonics and Electromagnetic Crystal Structures (PECS VIII)*, Sydney, Australia, 2009.

. N. Le Thomas, J. Jágerská, R. Houdré, M. Kotlyar, L. O'Faolain, D. M. Beggs, D. O'Brien, T. F. Krauss, J. Bolten, C. Moormann, T. Wahlbrink, J. Čtyroký, M. Waldow, M. Först, L.H. Frandsen, J. Fage-Pedersen, A. V. Lavrinenko, and P.I. Borel, "Probing the dispersion properties of 1D nanophotonic waveguides with far-field Fourier optics," *14th European Conference on Integrated Optics (ECIO'08)*, Eindhoven, The Netherlands, 2008.

Other presentations:

. J. Jágerská, "Photonic Crystals: Dispersion properties and slow light", Invited presentation at Palackého University, Departement of Optics, Sept 15. 2009, Olomouc, Czech Republic.

Jana Jágerská

Rue de la Blancherie 1, CH-1022 Chavannes-près-Renens, Switzerland
Tel: +41 764 08 40 87, Email: jagerska@gmail.com, Web: http://personnes.epfl.ch/jana.jagerska
Date of birth: 09.03.1982 (Bratislava, Slovakia), Slovak nationality, single

- **Expertise in nanophotonics and integrated optics, specialization: photonic crystals**
- **Well-developed ability to visualize, articulate and solve complex problems**
- **Experience in international and multilingual environment**

Education:

2007-
: **PhD degree in photonics (expected January 2011)**
Ecole Polytechnique Fédérale de Lausanne (EPFL)
Institute of Condensed Matter Physics
- Thesis: "Dispersion properties of photonic nanostructures"

2000 - 2006
: **Engineer degree (Ing.) in optoelectronics – Summa cum laude**
Czech Technical University in Prague, Prague, Czech Republic
Faculty of Nuclear Sciences and Physical Engineering
- Diploma thesis: "Optical Waveguide Amplifiers in Er-Doped Glass Substrates"

2005
: **Erasmus student exchange**
Royal Institute of Technology, Stockholm, Sweden
- Experimental work at the Department of Applied Physics, Laser Physics Group on "Green Induced Infrared Absorption in PPLiNbO."

Professional Experience:

2007-
: **Ecole Polytechnique fédérale de Lausanne (EPFL)**
Institute of Condensed Matter Physics (Research assistant)
- Simulation, design and experimental characterization of optical integrated devices. Development of the smallest optical gas sensor intended for (bio)sensing applications.

2005 – 2006
: **Institute of Photonics and Electronics (IREE), Academy of Sciences of the Czech Republic (**Research assistant)
- Numerical modeling and characterization of Er/Yb-co-doped waveguide amplifiers. The project was adopted by industrial partner SQS Vláknová optika a.s.

2002 – 2004
: **Institute of Electrical Engineering, Academy of Sciences of the Czech Republic** (Research Assistant, part-time)
- Optical diagnostics of dynamic phenomena in plasma jets.

Achievements and Awards:

Recognition award for the 2nd prize exequo for the oral presentation in the 9th International Conference on Photonic and Electronic Crystal Structures, Granada, Spain (2010)

Prize for the best diploma thesis, awarded by Czechoslovak section of IEEE, Chapter MTT/AP/ED/EMC (2006)

McKinsey&Company scolarship (2003)

The highest scholarship for excellent study results by Czech Technical University in Prague (years 2001-2004)

Publications: Regular papers: 8, Conferences and presentations: 10, H - factor: 3

Language skills:

Slovak	– native language	**English**	– fluent (C1/C2)
French	– advanced knowledge (C1)	**Czech**	– advanced knowledge (C1)
German	– intermediate level (B1/B2)		

Personal interests:

Mountaineering (Ski alpinism, Rock climbing); Music (piano); Ballroom dances